2017

Experimental Study of Plate Anchor-Soil Interaction in Sand for the Development of a Novel Anchor

Joseph Robert Giampa
University of Rhode Island, giampaj@gmail.com

EXPERIMENTAL STUDY OF PLATE ANCHOR-SOIL INTERACTION IN SAND FOR THE DEVELOPMENT OF A NOVEL ANCHOR

BY

JOSEPH ROBERT GIAMPA

A DISSERTATION SUBMITTED IN PARTIAL FULFILLMENT OF THE

REQUIREMENTS FOR THE DEGREE OF

DOCTOR OF PHILOSPHY

IN

CIVIL AND ENVIRONMENTAL ENGINEERING

UNIVERSITY OF RHODE ISLAND

2017

DOCTOR OF PHILOSPHY DISSERTATION

OF

JOSEPH ROBERT GIAMPA

APPROVED:

Dissertation Committee:

Major Professor Aaron S. Bradshaw

Christopher D.P. Baxter

David G. Taggart

Nasser H. Zawia
DEAN OF THE GRADUATE SCHOOL

UNIVERSITY OF RHODE ISLAND

2017

Abstract

Sustainable energy produced by offshore wind will likely increase as technology moves into deeper water. With increasing water depth, floating substructures may become the most economical and viable means for deploying offshore wind turbines, and thus require a greater reliance on anchoring systems. A green anchor concept called the “flying wing anchor” is currently in development to provide high vertical load capacity, and minimize the amount of energy needed to transport, install, and recover it from the seabed. Conceptually, the anchor is dynamically installed vertically through free-fall penetration, where the anchor will then rotate and dive into a position that is near normal to the anchor line in response to the service loads imposed by the offshore floating structure. To aid in the development of this novel anchor concept, an experimental program was conducted on scale-model anchors under 1g acceleration in a rigid sand-filled tank.

Chapter 1 describes a novel laboratory approach to measure the strength (i.e. friction angle) at very low confining pressures, typical of 1g physical model experiments. A simple tilt method is proposed to capture the peak friction angle at very low confining pressures, and then combined with conventional triaxial results to calibrate a modified stress-dilatancy relationship. The results of the tilt method indicate adequate and rational estimates of friction angle at very low stresses, and show to predict the critical state friction angle of the test sands within 1% to 3%. Furthermore, the modified stress-dilatancy relationship minimizes the asymptotic nature of the standard relationship at very low confining pressures by adding a second logarithmic term. Chapter 2 presents an experimental and

analytical study carried out in the same sand to investigate the effect of anchor shape on the pullout capacity of horizontal plate anchors. The experimental results indicate a difference in normalized capacity over a range of embedment depth with respect to shape. Circular anchors produced consistently larger capacities relative to square anchors, and with increasing embedment depth, circular, equilateral triangular, and kite anchors become comparable within 5%. The proposed analytical model predicted the pullout capacity within 10% for circular plates, and within, on average, 30% for the remaining shapes at shallow embedment depths.

Chapter 3 presents a physical model study to identify the anchor shapes that have the most effective dive performance, and to investigate the effects of initial embedment depth, loading line location, initial fluke orientation, and loading line angle on the dive trajectory. The results indicate that the dive performance of a simple kite plate anchor can be optimized when the loading line is attached at or near the anchor centroid at an initial fluke orientation of 10 degrees relative to the horizontal. This configuration has results in an additional 1.5 fluke lengths of embedment with no indication of pull out. Lastly, Chapter 4 presents an experimental study of the soil-anchor interaction during drag embedment. The capacity in the normal and shear (i.e. parallel to the anchor fluke) direction will control the trajectory and thus it is important to understand if the presence of one component of the mooring line force in one direction influences the resistance in the other direction. The resistance and kinematics of a simple kite-shaped plate anchor is measured under pure normal, shear, and rotational loading, and compared to force components acting on the anchor that were extracted from the previous dive trajectory experiments. The results

suggest there is minimal interaction between the normal and shear components acting on a simple fluke during dive trajectory in sand. Thus, the trajectory may be easily modeled with no adjustment to the resistance in either failure mode.

Acknowledgements

I would like to express my sincere gratitude to my major advisor, Dr. Aaron S. Bradshaw for his encouragement, guidance, trust, friendship, and motivation throughout my graduate career. You have provided me with amazing opportunities and have broaden my perspective by working on a variety of projects alongside many talented individuals. I will always be grateful for everything you have done for me and for allowing me to grow as a researcher and engineer. I would further like to extend my thanks to Dr. Christopher Baxter for always being available and providing valuable insight to my research, and for his endless efforts in teaching. I would like to thank Dr. David Taggart and Dr. James Miller for being part of my doctoral committee and defense.

I would like to thank the National Science Foundation for funding this research project, as well as, the project collaborators Dr. Kenneth Gavin, Dr. Paul Doherty, Dr. Vinayagamoothy Sivakumar, Dr. Hande Gerkus, Soroosh Jalilvand, and Joseph Fanning for their valuable contributions and collaborations. It has been a pleasure to meet and work alongside such talented individuals and I look forward to working with you in the future. Much of this research would not have been possible without the help of such an amazing research team at URI. I would like to thank Benedikt Breithaupt, Sven Sivarajah, Fabian Dietrich, and Kevin Broccolo for all of your assistant over the years in collecting such valuable and high quality data. It would not have been possible without your contributions and efforts. Furthermore, thank you to my amazing friends for keeping me sane: Bivian Reyes, Dr. Alesandra C. Morales Vélez, Wendy Laurent, and Jeffrey and Amanda Costa.

None of this of course would been manageable if it wasn't for my loving wife Kara. You constantly push me to become a better individual, and to always pursue my dreams. You have kept me grounded from not only the start of my graduate career, but since our senior year in high school. I love you with all of my heart.

I would also like to thank my brother, Jake, for lending an ear and for always trekking from college down to Rhode Island just to hang out. Lastly, thank you to my mom and dad for always providing me with your unconditional love and support throughout my entire life. I would not be the man I am today if it wasn't for everything you have done for me.

With that, I would like to say it's been a good run URI, but I am ready to move on to the next exciting chapter in my life!

Preface

This dissertation is organized in manuscript format and is comprised of four manuscripts contained in four separate chapters. It is the intention of the author that these manuscripts will be submitted for publication in appropriate peer-reviewed journals. The first chapter deals exclusively with the characterization of the strength of sands at extremely low confining stresses, whereas the remaining three manuscripts focus on the experimental behavior of a novel drag-type anchor proposed for the use in deep water offshore wind development. Chapter 1 presents a simple experimental approach to assess the peak friction angle of sand at extremely confining stresses typical of 1g physical model testing. The method is combined with conventional triaxial data to calibrate a modified stress-dilatancy relationship used to estimate friction angle over a full range of confining stresses. Chapter 2 investigates the effect of shape on the pullout capacity of horizontal plate anchors in sand through 1g physical model experiments. A theoretical framework is presented for the development of a nonassociated flow limit equilibrium solution to predict the pullout capacity of asymmetric anchor shapes. Chapter 3 presents an experimental investigation into the dive trajectory behavior of a plate anchor that is initially embedded in sand. The study was designed to identify optimal anchor shapes that have the most effective dive performance, and to investigate the effects of initial embedment depth, loading line location, initial fluke orientation, and loading line angle on the dive trajectory. Finally, Chapter 4 presents an experimental study to investigate the normal and shear force interactions that occur during drag embedment of a novel drag-type anchor in sand that is initially embedded in sand.

Table of Contents

List of Tables

List of Figures

1. Simple Approach for Assessing the Peak Friction Angle of Sand at Very Low Confining Stresses

Prepared for submission to ASTM Geotechnical Journal

Abstract

This paper presents an experimental approach that may be used to assess the peak friction angle of sand at extremely low confining stresses. Previous studies in literature have performed triaxial testing on sands at initial confining stresses as low as 2 kPa with corresponding mean effective stresses at failure ranging from 6 to 9 kPa. However, at initial confining stresses below 10 kPa, factors that normally would be negligible in triaxial tests become amplified and may contribute to the strength if not accounted for properly. There is no literature that presents a method to measure peak friction angle of sands below a mean effective stress at failure of 6 kPa. A simple tilt test method is proposed in this study to capture peak friction angle at very low confining stresses, that are typically below the range of element tests. The tilt and triaxial test results were combined to calibrate a modified stress-dilatancy relationship that can be used to estimate friction angle over a full range of confining stresses.

Introduction

It has been well established in the literature that sands exhibit increased dilatancy with decreasing confining stress. At very low confining stress, even very loose sands will show dilative behavior (e.g. Huang et al. 2015). Characterizing the strength and dilatancy of sands at low stress levels below 10 kPa may be needed in some geotechnical applications including small-scale 1g physical modeling, and the analysis of seabed anchors and buried pipelines (White et al. 2008; Bradshaw et al. 2015; Bradshaw et al. 2016; Giampa et al. 2016; Gerkus et al. 2016), as well as, micro-gravity environments, cavity expansion,

shallow foundations, surface failure slope stability, and cone penetration test modeling (Salgado et al. 1997).

It is common to use standard laboratory element tests such as the triaxial test to determine the friction and dilation angles of reconstituted sand. Triaxial tests have been performed at low initial confining pressures ranging from 1.4 kPa to 8 kPa (e.g. Ponce and Bell 1971; Chakraborty and Salgado 2010; Huang et. al. 2015). However, the results of triaxial tests can be unreliable at very low initial confining pressures ($\sigma'_3 < 10$ kPa) because of several factors that would normally be neglected become considerably large (Ponce and Bell 1971). These factors include the strength contributed by the rubber membrane, self-weight of the specimen, and piston and/or bearing friction. Other tests that have been used to measure friction angles at very low pressures include tilt table devices to measure friction along rock joints (e.g. Cawsey and Farrar 1976; Hencher 1976; Bruce et al. 1989), geosynthetic interfaces (e.g. Girard et al. 1990; Shan 1993; Lalarkotoson et al. 1999), and critical state friction angle (ϕ'_c) of sand under 1g and microgravity environments (e.g. Huang and Mao 2013; Huang et al. 2015). Methods involving the measurement of the angle of repose have also been used to assess the critical state friction angle of sand (e.g. Cornforth 1973; Santamarina and Cho 2001; Sadrekarimi and Olson 2011).

Given the difficulty of element testing at low stress levels (< 10 kPa), this study proposes a new approach to measure the strength of sand at very low confining stresses. It is presumed that this method will provide reliable results and eliminate factors from standard

element tests that may contribute to the overall strength. The remaining sections of the paper present the test sands used in this study, the proposed method, a triaxial experimental program, and analysis of test data.

Test Sands

This study uses two test sands to demonstrate the proposed method to characterize the strength at very low stress levels. The two sands are Westerly Beach (Bradshaw et al. 2015, 2016; Gerkus et al. 2016) and Golden Flint (Giampa et al. 2016; Schneider et al. 2016), which are currently being used in physical model testing facilities at the University of Rhode Island (URI) and the Naval Facilities Engineering Command (NAVFAC), respectively. The sands primarily consist of quartz and have very similar grain size (Figure 1.1) and index properties (Table 1.1). Characterization of the test sands include standard index testing, consolidated drained triaxial (TX) tests, and the proposed tilt tests. These datasets are used to expand on the behavior of sand at low confining stresses.

Proposed Tilt Test Method

The proposed tilt method is based on the theory of infinite slope failure, for which determines the conditions (i.e. soil strength) under which a layer of soil will slip along a plane parallel to the ground surface. A factor of safety (FS) is computed that is a measure of the closeness to conditions of sliding that exist in the slope **(**Cruikshank 2002**)**. Based on an infinite slope analysis the factor of safety for a cohensionless soil for total stress conditions (or effective stress conditions with zero pore pressure) can be expressed as the ratio of $\tan(\phi')/\tan(\alpha)$, where α is the angle of the slope (Duncan and Wright 2005). For a

slope impending failure (i.e. FS = 1), the angle α of the slope has to equal the soil strength ϕ'. Building off of infinite slope theory and the angle of repose for a loose deposit, the proposed tilt method estimates the peak friction angle at very low stresses as the inclination of the slope that causes failure (i.e. sand movement) for a range of relative density (D_r). However, an uncertainty that is associated with the proposed method is measuring the exact failure location, thus the mean effective confining pressure at failure (p'_f). As an approximation, the mean effective confining pressure at failure is taken as a range of γD_{50}, being the smallest possible stress, up to $25\gamma D_{50}$, where γ is the dry unit weight of the sand, based on shear band formation observed in laboratory tests, discrete element modeling, and theoretical considerations (e.g. Roscoe 1970; Vardoulakis and Graf 1985; Vardoulakis and Aifantis 1991; Yoshida 1994; Bradet and Proubet 1991; Oda et al. 1997; Finno et al. 1997; Iwashita and Oda 1998; Alshibli and Sture 1999; Sadrekarimi and Olsen 2010). For the sands used in this study, p'_f may range from approximately 0.0042 kPa to 0.12 kPa in the proposed method. Therefore, for further analysis p'_f was taken to be on the order of 0.1 kPa.

Tilt tests were performed on two quartz sands at different relative densities, and was performed using a standard metal mold provided for maximum and minimum index density tests (ASTM D4253; ASTM D4254). Dry sand was placed in the standard metal mold using a funnel maintaining nearly zero drop height to achieve an initial loose soil state. Once the mold was filled, any excess sand was carefully removed to make the sample level with the top. Samples were then vibrated, with a surcharge, on a vibratory table to achieve a range of relative densities from 0% to 80%. An inclinometer was then attached to the side

of the mold to track the angle to failure (i.e. sand movement at the surface) or the friction angle. Figure 1.2 summarizes the results of the tilt tests as peak friction angle versus relative density index (I_D), defined as e_{max}-e/e_{max}-e_{min} where e_{max}, e_{min} are the maximum and minimum void ratios, and e is the current void ratio of the sand.

Triaxial Testing

A total of 43 TX tests were conducted with the results summarized in Table 1.2. Three laboratories were used to characterize the test sands. The Westerly Beach sand has been characterized at the University of Rhode Island (URI) geotechnical laboratory. Similarly, the Golden Flint sand has been characterized over three separate laboratories which include URI, University of Tennessee, Knoxville (UTK) (Alshibli 2015), and California State University, Los Angeles (CSLA) (Tufenkjian and Yee 2006).

Both sands used in this study were tested in triaxial conditions over a range of initial confining pressure from 8 kPa to 150 kPa, with corresponding p'_f values from 16 kPa to 449 kPa. Three types of triaxial tests were performed on the test sands. All TX samples had a diameter and height of approximately 71 mm and 142 mm, respectively. The samples were prepared using dry pluviation with a funnel that allowed for a range of relative densities by varying the opening size and fall height. The first type of test consisted of conventional consolidated drained triaxial (CD TX) tests on saturated samples using an automated load frame system performed at URI and CSLA laboratories. At the URI laboratory, volume change was measured using a burette system that allowed the

calculation of peak dilation angles (ψ_p), however, CSLA only reported peak friction angle values. Triaxial samples were sheared after a B-parameter of at least 0.93 was achieved.

The second type of test was a slight modification to the standard CD TX test performed at UTK on the Golden Flint sand. Following preparation, a vacuum was applied to the pore space of the sample to prevent its collapse as the split mold was removed. The external test cell was assembled around the sample, filled with water, and pressurized to apply the desired initial confining pressure, while gradually reducing the vacuum connected to the specimen pore space. Upon reaching the target initial confining pressure, the sample pore was vented and kept at atmospheric pressure throughout the experiment; the specimen was sheared dry under quasi-static conditions. The volume change of the specimen was measured using the volume of water pumped in/purged out of the cell while maintaining a constant confining pressure during the experiment. Lastly, the third type of test was performed on dry samples under a vacuum in order to achieve very low initial confining pressures down to 8 kPa. When the desired confining stress was achieved through the vacuum at the TX base, the external test cell was assembled around the sample, where a special cell top cap was put in place to eliminate the resistance caused by the bearings against the piston. This allowed the sample to be tested at very low effective conditions while minimizing sample disturbance and piston friction. It was not possible to measure volume change in these tests or successfully complete tests below 8 kPa due to equipment limitations. Sample measurements before and after shear were taken in order to apply an area and membrane correction based on Baxter (2000).

Analysis of Test Data

Validation of Tilt Test Data

To help verify the proposed tilt method, the critical state friction angle was measured and compared to values previously obtained for the Westerly Beach and Golden Flint sands. Two published methods were used to determine the critical friction angle of the test sands: 1. Bolton (1986), 2. Santamarina and Cho (2001). Bolton (1986) extrapolates the peak friction angle to zero dilation angle (i.e. zero volumetric strain or critical state) using triaxial data (Figure 1.3). Santamarina and Cho (2001) proposed a tilt method using a graduated cylinder were sand is poured into the graduated cylinder filled with water, then tilted approximately 60^o and brought slowly back to the vertical position. The angle of repose made by the sand is taken as the critical state friction angle. A comparison of the critical state friction angles is summarized in Table 1.3. The resulting ϕ'_c values from the proposed tilt method were within 1% and 3% of the critical state friction angles determined using the Bolton (1986) and Santamarina and Cho (2001) methods.

It is well understood that critical state friction angle, for a particular sand, will not change with a change of initial relative density or initial confining pressure, but will vary with loading path (Chakraborty and Salgado 2010). Thus, the peak friction angle will also change. Literature has shown that friction angle under plane strain conditions can be 3^o to 5^o higher than for triaxial conditions (Tatsuoka et al. 1986; Pradhan et al. 1988; Yoshimine 2005). However, some researchers suggest that the critical state friction angle is unique regardless of boundary conditions and that there is no difference. Using a similar tilt

method to obtain ϕ'_c, Sanatmarina and Cho (2001) showed a 1^o difference in the value when compared to undrained triaxial tests for a range of sands. This difference was also seen for the test sands in this study and thus for further analyses the friction angles obtained from the proposed tilt test method have not been adjusted.

Modified Stress-Dilatancy Relationship

In order to analyze all test results, which cover a wide range of stresses and relative densities, Bolton (1986) stress-dilatancy relationship was adopted. The Bolton (1986) stress-dilatancy relationship has been used in literature for modeling the strength and dilatancy of sands at low confining stress (e.g. White et al. 2008; Chakraborty and Salgado 2010; Giampa et al. 2016; Bradshaw et al. 2016). The work is based on the fundamental understanding that the shear strength is attributed to the combination of inter-particle friction and dilation. The proposed relationship was developed using a large database of TX and plane strain (PS) compression test data, and describes the shear strength and dilatancy of sands based on relative density and p'_f as shown by the following Eqns.

$$\phi'_p - \phi'_c = A_f I_R \tag{1.1}$$

$$\phi'_p - \phi'_c = \beta\psi_p \tag{1.2}$$

$$I_R = I_D\left(Q - \ln\left(p'_f\right)\right) - R \tag{1.3}$$

$$\phi'_p - \phi'_c = A_f\left\{I_D\left(Q - \ln\left(p'_f\right)\right) - R\right\} \tag{1.4}$$

Where ϕ'_p = peak friction angle, ϕ'_c = critical state friction angle, ψ_p = peak dilation angle, I_R = relative dilatancy index, I_D = relative density index, p'_f = mean effective confining pressure at failure (in kPa), A_f, β, Q, R = soil-specific constants. The soil-specific constants can be determined through a simple linear regression using triaxial results shown in Figures 1.3-1.5 (e.g. Salgado et. al. 2000; Chakraborty and Salgado 2010; Giampa et al. 2016; Bradshaw et al. 2016). The constants are summarized in Table 1.1. As the mean effective confining stress at failure approaches a value close to 0 kPa, estimates of ϕ'_p from Eqn. (1.4) become large and unrealistic. Thus, the results of the tilt test are plotted in Figure 1.5 to show the difficulty in calibrating the existing relationship using ϕ'_p results at very low stresses. The correlation becomes poor with a resulting coefficient of determination (r^2) ranging from 0.6 to 0.7. This is caused by the logarithmic nature of the relationship in which it becomes asymptotic as p'_f approaches zero. It should be noted that the critical state friction angle from the tilt test (D_r = 0%) falls in line with the triaxial results, and with increasing relative density the data begins to deviate.

Chakraborty and Salgado (2010) gathered TX and PS data on Toyoura sand at p'_f from 9 kPa to 400 kPa to examine Bolton (1986) stress-dilatancy relationship at low stresses. Chakraborty and Salgado (2010) found when the constant R is set to a value of 1, Q decreases with decreasing σ'_3. As part of this study, the same form of the Q function presented by Chakraborty and Salgado (2010) is adapted herein, only p'_f is used in place of initial confining pressure to be consistent with Eqn. (1.3) (i.e. $Q = Q_1 + \Delta Q \ln(p'_f)$). By substituting the revised Q function into Eqn. (1.3) and combining with Eqn. (1.1), a modified form of the dilatancy index can be expressed as

$$I_R = I_D\left[\left(Q_1 + \Delta Q \ln\left(p'_f\right)\right) - \ln\left(p'_f\right)\right] - R \tag{1.5}$$

Where Q_1, ΔQ = soil-specific constants. Q_1 = a value of Q at a p'_f of 1 kPa, and ΔQ = the change in Q at a p'_f other than 1 kPa. The modified fitting parameters can be determined through a multi-variable linear regression in which should take on the general form of $y = a_1x_1+a_2x_2+b$. By equating Eqn. (1.5) with Eqn. (1.1) and rearranging, the regression equation can be expressed as

$$I_R + I_D \ln\left(p'_f\right) = I_D Q_1 + I_D \Delta Q \ln\left(p'_f\right) - R \tag{1.6}$$

The regression of Eqn. (1.6) can be performed using a statistic software add-on in Excel. The addition of the second logarithmic term in Eqn. (1.6) allows the modified fitting parameters to be regressed using results obtained from the tilt and triaxial tests to cover a wide range of stresses. The additional term simply minimizes the asymptotic behavior found in the standard Bolton (1986) relationship. Thus, providing a more rational estimate of the peak friction angle at a low stress range. A summary of the modified terms are found in Table 1.1. The regression of Eqn. (1.6) resulted in an r^2 value of 0.94 and 0.97 for the Westerly Beach and Golden Flint sands, respectively.

Predicting Strength of Sand

Figure 1.6 compares the estimated peak friction angles versus p'_f for two relative densities using Eqns. (1.4) and (1.6). As expected the peak friction angle increases with decreasing mean effective stress at failure and increasing D_r. The standard relationship, Eqn. (1.4), largely overestimates the peak friction angle over a range of relative density, with a significant difference being evident below p'_f = 10 kPa. Due to the logarithmic nature of Eqn. (1.4), the contours in Figure 1.6 produce unrealistic values of ϕ'_p at extremely low stresses. Additionally, the relationship is being extrapolated beyond its calibration due to the difficulty in incorporating the tilt test results. However, the additional logarithmic term in Eqn. (1.6) better allows the equation to estimate friction angle in the low stress range, as it essentially flattens the contours (Figure 1.6). Regressing Eqn. (1.6) using the tilt and triaxial test results provides a wide range of p'_f to calibrate the relationship and avoids extrapolation down to low stresses. The estimated peak friction angles at a $p'_f \approx 0.1$ kPa for both test sands produced values approximately 85% of those predicted using Eqn. (1.4).

Conclusions

The objective of this study was to present an experimental approach that may be used to assess the peak friction angle of sand at extremely low confining stresses. The results were then used to calibrate a modified stress-dilatancy relationship so that the peak friction angle may be predicted over a wide range of stresses. The simple tilt test method is meant to eliminate strength contributing factors often associated with element testing at initial confining pressures below 10 kPa. The results of the tilt test on two quartz sands indicate adequate and rational estimates of the friction angle at extremely low stresses. Comparisons

of the critical state friction show that the tilt test comes within 1% to 3% of the critical state friction angle of the test sands, determined from two published methods. Therefore, providing some validation that it may be extended to denser soil. Calibration of a modified Bolton (1986) stress-dilatancy relationship was carried out using the results obtained from triaxial and the tilt test approach. The modification of the stress-dilatancy relationship, adapted from Chakraborty and Salgado (2010), allows for a calibration to be accomplished over a wide range of stresses. The modification adds a second logarithmic term to the relationship which in turn minimize the asymptotic nature of the standard Bolton (1986) relationship at low stress levels. As shown by the results, the modified relationship predicted peak friction angles, at a mean effective stress equal to $p'_f = 25\gamma D_{50}$, that were approximately 85% of those estimated by the standard relationship.

Although further investigation is warranted using additional sand and regarding the exact value of the mean effective stress at failure used in the tilt test approach, the current method offers a means to capture reasonable estimates of peak friction angle in sand at low stresses.

Acknowledgments

This material is based upon work supported by the National Science Foundation under Grant No. 1300142 and also by the Science Foundation Ireland under the U.S.-Ireland R&D Partnership Program Grant No. SFI/2012/US/E2479.

References

Alshibli, K. A. (2015). "Stress-dilatancy response of fine golden flint sand." Rep. Prepared for Ocean Engineering Div., NAVFAC, Port Hueneme, CA.

Alshibli, K. A., and Sture, S. (1999). "Shear band thickness measured by digital image techniques." *J. Comput. Civ. Engrg.*, 13(2), 103–109.

ASTM (2000). "Standard test methods for maximum index density and unit weight of soils using a vibratory table." D4253-00. West Conshohocken, PA: ASTM International.

ASTM (2000). "Standard test methods for minimum index density and unit weight of soils and calculation of relative density." D4254-00. West Conshohocken, PA: ASTM International.

Baxter, D.Y. (2000). "Mechanical behavior of soil-bentonite cutoff walls." PhD Dissertation. Dept. of Civil Engineering, Virginia Polytechnic and State Univ., Blacksburg, Va.

Bolton, M. (1986). "The strength and dilatancy of sands." *Geotechnique*, 36(1), 65–78.

Bardet, J. P., and Proubet, J. (1991). "A numerical investigation of the structure of persistent shear bands in granular media." *Geotechnique*, 41(4), 599–613.

Bradshaw, A.S., Giampa, J., Dietrich, F., Gilbert, R.B., and Gerkus, H. (2015). "Pullout Capacity of Plate Anchors in Sand for Floating Offshore Wind Turbines." *Proc., of the 3rd Inter. Symp. on Frontiers in Offshore Geotechnics*, Oslo, Norway: NGI. 833-838.

Bradshaw, A.S., Giampa, J.R., Gerkus, H., Jalilvand, S., Fanning, J., Nanda, S., Gilbert, R., Gavin, K., and Sivakumar, V. (2016). "Scaling Considerations for 1-g Model Horizontal Plate Anchor Tests in Sand." *Geotech. Testing J.*, 39 (6), 1-9.

Bruce, I.G., Cruden, D.M., and Eaton, T.M. (1989). “Use of a tilting table to determine the basic friction angle of hard rock samples.” *Can. Geotech. J.*, 26(3), 474-479.

Cawsey, D.C. and Farrar, N.S. (1976). “A simple sliding apparatus for the measurement of rock joint friction.” *Geotechnique*, 26(2), 382-386.

Chakraborty, T., and Salgado, R., (2010), "Dilatancy and Shear Strength of Sand at Low Confining Pressures.” *J. Geotech. and Geoenv. Engrg.*, 136(3), 527-532.

Cornforth, D.H. (1973). “Prediction of drained strength of sands from relative density measurements.” *American Society for Testing and Materials*, 281-303.

Cruikshank, K.M. (2002). *Theory of slope stability,* Portland State University.

Duncan, J.M. and Wright, S.G. (2005). *Soil Strength and Slope Stability*, 1st Ed., Wiley, New York.

Finno, R., Harris, W., Mooney, M., and Viggiani, G. (1997). “Shear bands in plane strain compression of loose sand.” *Geotechnique*, 47(1), 149–165.

Gerkus, H., Giampa, J.R., Senanayake, A.I., Lai, Y., Huang, Y., Flores, J. E.I., Breithaupt, N.B., Sivarajah, S., Bradshaw, A. S., and Gilbert, R.B. (2015). “Preliminary development of a new concept to improve sustainability of offshore foundations.” *Proc. Geo-Congress Conference*, ASCE, IL.

Giampa, J.R., Bradshaw, A.S., and Schneider, J.A. (2016). “Influence of Dilation Angle on Drained Shallow Circular Anchor Uplift Capacity,” *Int. J. Geomech.*, 17(2).

Girard, H., Fischer, S., and Alonso, E. (1990). “Problems of friction posed by the use of geomembranes on dam slopes – examples and measurements.” *J. Geotextiles and Geomembranes*, 9, 129-143.

Hencher, S.R. (1976). “Discussion on: A simple sliding apparatus for the measurement of rock joint friction.” *Geotechnique,* 26(4), 641-644.

Huang, Y. and Mao, W. (2013). “First results derived from a drop-tower testing system for granular flow in a microgravity environment.” *Landslides*, 10(4), 493-501.

Huang, Y., Cheng, H.L., Osada, T., Hosoya, A., and Zhang, F. (2015). “Mechanical behavior of clean sand at low confining pressure: Verification with element and model tests.” *J. Geotech. Geoenvir. Engrg.*, 141(8).

Iwashita, K., and Oda, M. (1998). “Rolling resistance at contacts in the simulation of shear band development by DEM.” *J. Engrg. Mech.*, 124 (3), 285–292.

Lalarakotoson, S., Villard, P., and Gourc, J.P. (1999). “Shear strength characterization of geosynthic interfaces on inclined planes.” *Geotech. Testing J.*, 22(4), 284-291.

Oda, M., Iwashita, K., and Kazama, H. (1997). “Micro-structure developed in shear bands of dense granular soils and its computer simulation-mechanism of dilatancy and failure.” *Proc., IUTAM Symp. on Mechanics of Granular and Porous Materials*, N. A. Fleck and A.C. F. Cocks, eds., Kluwer, New York, 353–364.

Ponce, V.M. and Bell, J.M. (1971). “Shear strength of sand at extremely low pressures.” *J. Soil Mech. Fnds Div.*, 97(4), 625-638.

Pradhan, T.B.S., Tatsuoka, F., and Horii, N. (1988). “Strength and deformation characteristics of sand in torsional simple shear.” *Soils Found.*, 28(3), 131–148.

Roscoe, K.H. (1970). “The influence of strains in soil mechanics.” *Geotechnique,* 20(2), 129-170.

Sadrekarimi, A. and Olson, S.M. (2010). “Shear band formation observed in ring shear tests on sandy soils.” *J. Geotech. Geoenvir. Engrg.*, 136(2), 366-375.

Sadrekarimi, A. and Olson, S.M. (2011). “Critical state friction angle of sands.” *Geotechnique*, 61(9), 771-783.

Salgado, R., Mitchell, J.K., and Jamiolkowski, M. (1997). “Cavity expansion and penetration resistance in sand.” *J. Geotech. Geoenvir. Engrg.*, 123(4), 344-354.

Salgado, R., Bandini, P., and Karim, A. (2000). “Shear strength and stiffness of silty sand.” *J. Geotech. Geoenviron. Engrg.*, 5(451), 451–462.

Santamarina, J.C., and Cho, G.C. (2001). “Determination of critical state parameters in sandy soils-Simple procedure.” *Geotech. Testing J.*, 24(2), 185-192.

Schneider, J.A., Giampa, J.R., Newgard, J.T., and Bradshaw, A.S. (2016). "Calibrating CPT relative density and strength correlations for a laboratory fine sand." *Proc. 5th Inter. Conf. on Site Characterisation*, ISC 5, Brisbane, in press.

Shan, H.Y. (1993). “Stability of final covers placed on slopes containing geosynthetic clay liners.” Ph.D. Dissertation, University of Texas at Austin.

Tatsuoka, F. (1987). “Discussion on ‘The strength and dilatancy of sands’ by Bolton, 1986.” *Geotechnique*, 37(2), 219-226.

Tufenkjian, M. and Yee, E. (2006). “Soil friction angle and relative density of sand from minicone penetration tests at shallow depth.” Rep. prepared for Ocean Engineering Div., NAVFAC, Port Hueneme, CA.

Vardoulakis, I. and Graf, B. (1985). “Calibration of constitutive models for granular materials using data from biaxial experiments.” *Geotechnique*, 35(3), 299–317.

Vardoulakis, I., and Aifantis, E. (1991). “A gradient flow theory of plasticity for granular materials.” *Acta Mech.*, 87(3–4), 197–217.

White, D.J., Cheuk, C.Y., and Bolton, M. (2008). “The uplift resistance of pipes and plate anchors buried in sand.” *Geotechnique*, 58(10), 771-779.

Yoshida, T. (1994). “Strain localization and shear banding during failure of sands.” PhD thesis, Univ. of Tokyo (in Japanese).

Yoshimi, Y. and Kishida, T. (1981). “A ring torsion apparatus for evaluating friction between soil and metal surfaces.” *Geotech. Testing J.*, 4(4), 145-152.

Table 1.1. Properties of test sand.

	Westerly Beach	Golden Flint
Parameter	Value	Value
γ_{max} (kN/m^3)	18.10	17.68
γ_{min} (kN/m^3)	14.09	14.24
e_{max}	0.844	0.847
e_{min}	0.436	0.487
G_s	2.65	2.68
D_{50} (mm)	0.30	0.25
C_u	1.63	1.61
C_c	1.24	1.13
ϕ'_c (deg)	32.3	33.9
β	0.69	0.64
A_f	4.8	3.6
Q (Bolton 1986 Method)	7.03	9.61
R (Bolton 1986 Method)	-0.12	-0.69
Q_1 (This Study)	4.46	5.75
ΔQ (This Study)	0.53	0.80
R (This Study)	-0.27	-0.69

Table 1.2. Summary of TX results for Westerly Beach and Golden Flint sand.

Lab	Sand	Condition	D_r	p'_f (kPa)	σ'_3 (kPa)	ϕ'_p (deg)	ψ_p (deg)
URI	Westerly B.	Dry	38	102	50	37.4	-
URI	Westerly B.	Dry	43	64	30	38.8	-
URI	Westerly B.	Dry	42	42	20	38.5	-
URI	Westerly B.	Dry	42	43	20	39.0	-
URI	Westerly B.	Dry	44	22	10	39.8	-
URI	Westerly B.	Dry	48	23	10	40.9	-
URI	Westerly B.	Dry	19	93	50	34.5	-
URI	Westerly B.	Dry	17	58	30	35.5	-
URI	Westerly B.	Dry	15	38	20	35.3	-
URI	Westerly B.	Dry	13	20	10	36.2	-
URI	Westerly B.	Dry	13	16	8	36.7	-
URI	Westerly B.	Saturated	20	58	30	35.8	3.2
URI	Westerly B.	Saturated	21	180	100	33.1	2.8
URI	Westerly B.	Saturated	53	208	100	38.2	9.7
URI	Westerly B.	Saturated	52	69	30	41.5	12.9
UTK	Golden F.	Dry	0	54	25	39.6	-
UTK	Golden F.	Dry	0	97	50	36.0	3.7
UTK	Golden F.	Dry	0	288	150	35.4	-
UTK	Golden F.	Dry	65	73	25	47.8	22.0
UTK	Golden F.	Dry	61	139	50	46.6	20.4
UTK	Golden F.	Dry	61	402	150	45.7	19.8
UTK	Golden F.	Dry	81	75	25	48.5	24.0
UTK	Golden F.	Dry	81	151	50	48.8	22.7
UTK	Golden F.	Dry	81	449	150	48.5	22.0
URI	Golden F.	Saturated	62	81	30	45.8	17.4
URI	Golden F.	Saturated	40	76	30	44.2	15.3
URI	Golden F.	Saturated	5	57	30	34.8	1.4
URI	Golden F.	Dry	8	101	50	37.2	-
URI	Golden F.	Dry	7	102	50	37.6	-
URI	Golden F.	Dry	7	61	30	37.5	-
URI	Golden F.	Dry	8	39	20	36.1	-
URI	Golden F.	Dry	6	22	10	39.3	-
URI	Golden F.	Dry	54	136	50	46.1	-
URI	Golden F.	Dry	53	135	50	46.0	-
URI	Golden F.	Dry	54	82	30	46.3	-
URI	Golden F.	Dry	53	58	20	47.6	-
URI	Golden F.	Dry	51	30	10	48.4	-
CSLA	Golden F.	Saturated	17	76	34	39.9	-
CSLA	Golden F.	Saturated	29	79	34	41.3	-
CSLA	Golden F.	Saturated	43	85	34	43.4	-
CSLA	Golden F.	Saturated	32	87	34	44.2	-
CSLA	Golden F.	Saturated	60	105	34	49.1	-
CSLA	Golden F.	Saturated	62	99	33	48.7	-

Table 1.3. Comparison of average critical state friction angle.

Sand	Critical State Friction Angle, ϕ'_c (deg)		
	Bolton (1986)	Santamarnia and Cho (2001)	Tilt (This Study)
Westerly Beach	32.3	31.6	32.4
Golden Flint	33.9	32.8	34.0

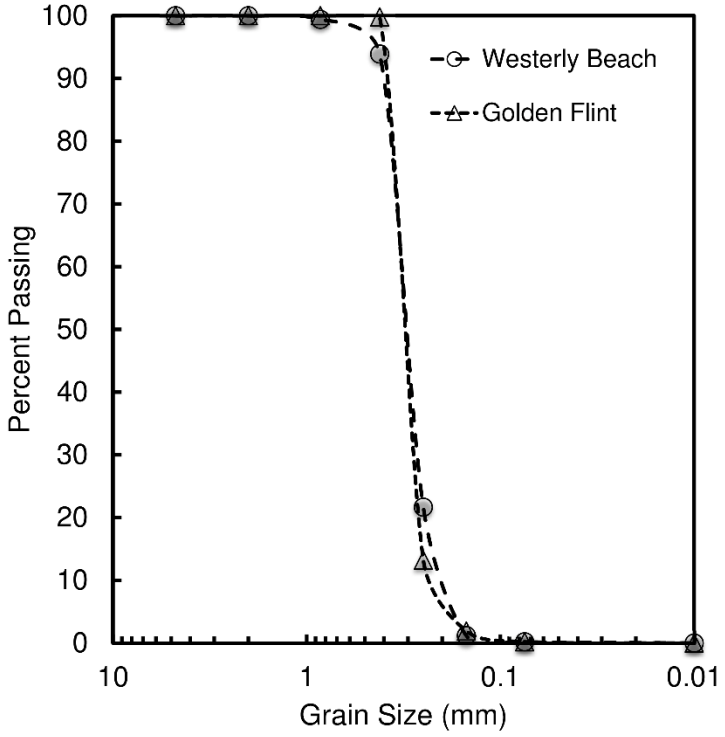

Figure 1.1. Grain size distribution of test sands.

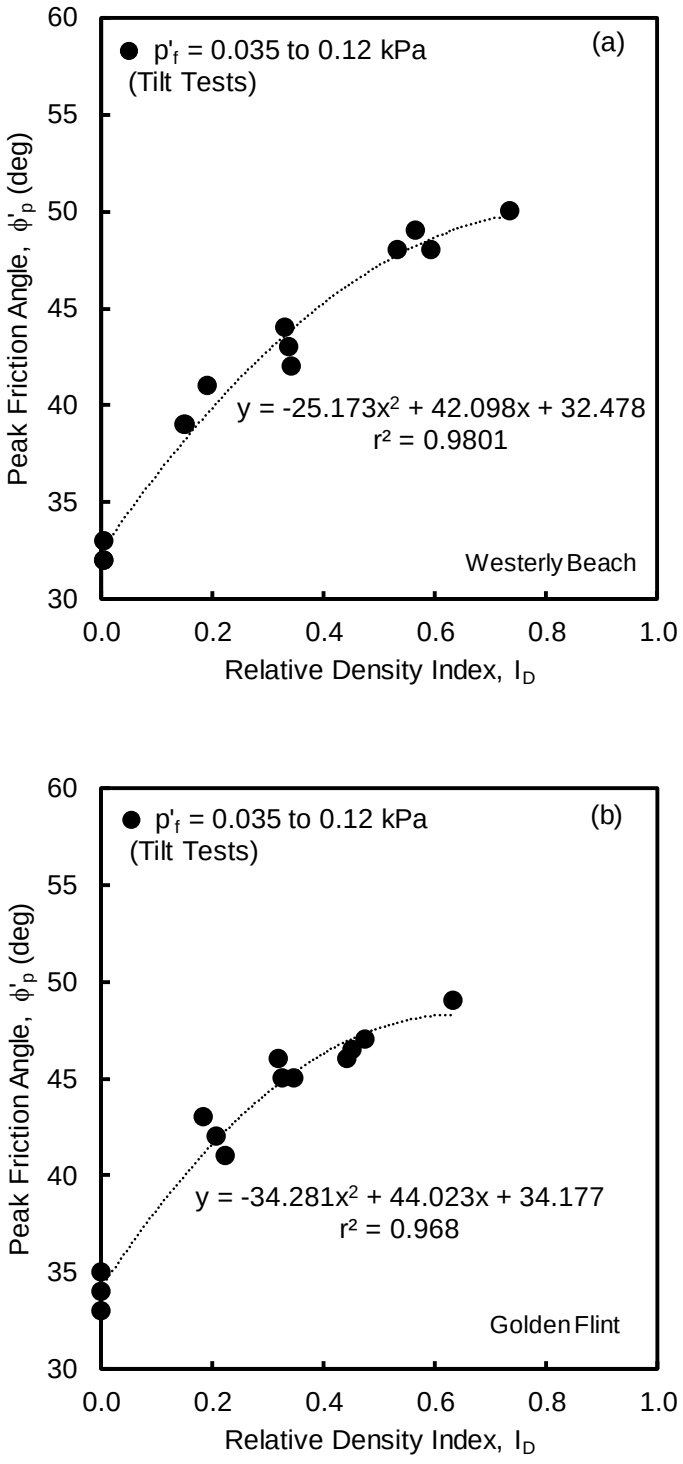

Figure 1.2. Results of tilt test method for (a) Westerly Beach sand; and (b) Golden Flint sand assuming a range of mean effective stress at failure.

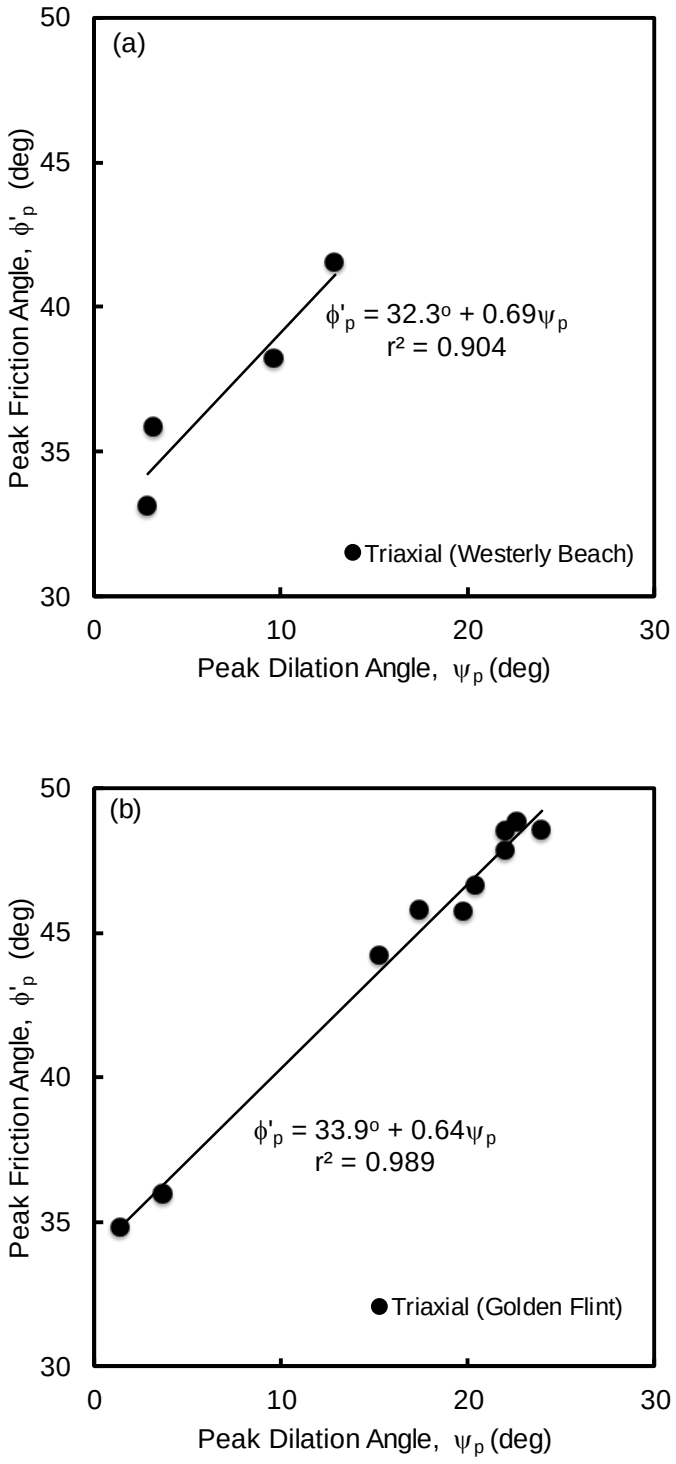

Figure 1.3. Relationship between peak friction angle and dilation angle in TX test for (a) Westerly Beach sand; and (b) Golden Flint sand.

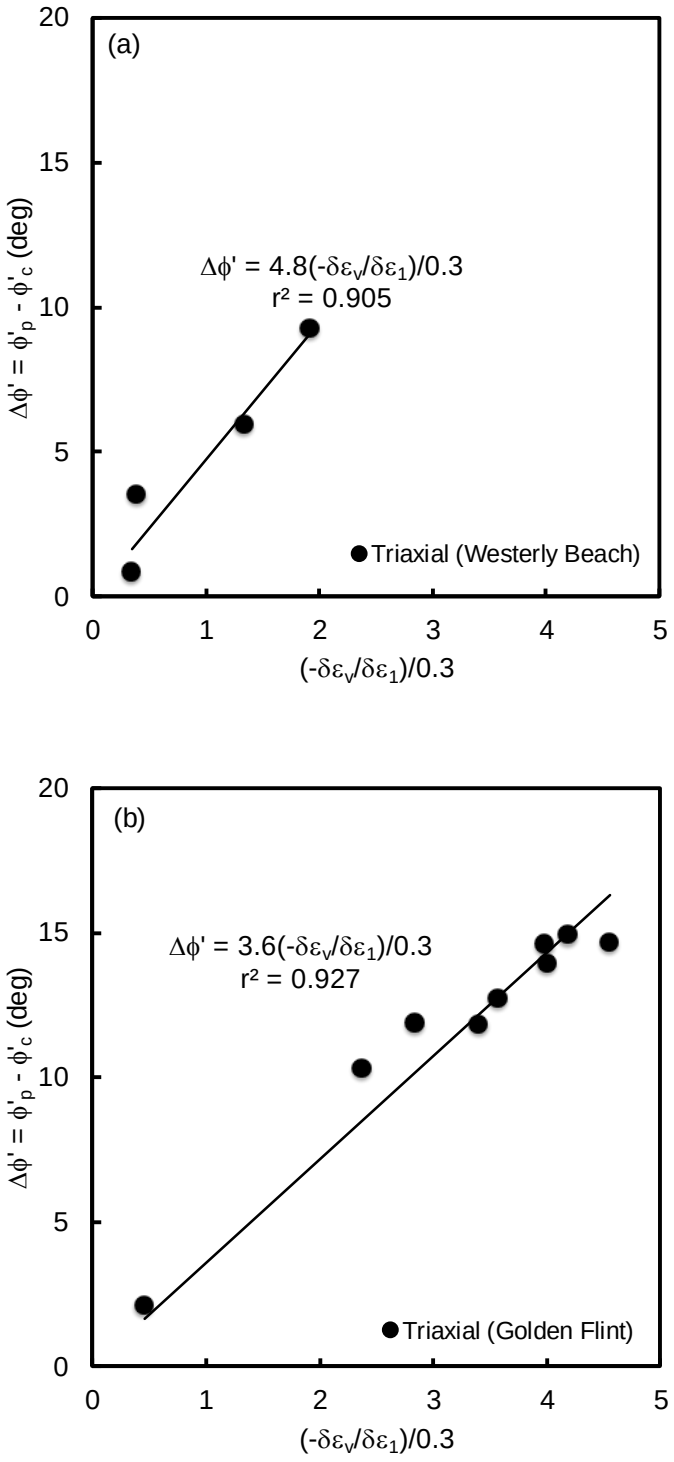

Figure 1.4. Assessment of Bolton (1986) A_f parameter from TX tests for (a) Westerly Beach sand; and (b) Golden Flint sand.

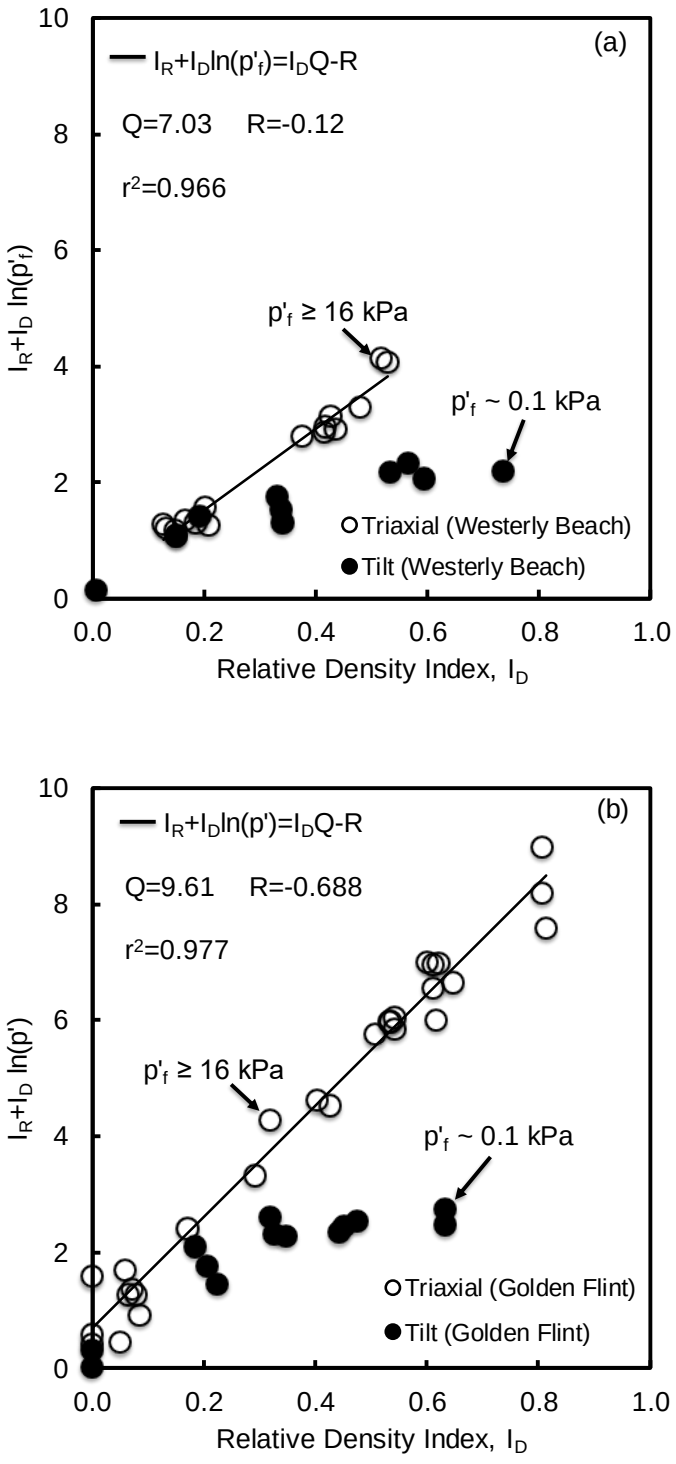

Figure 1.5. Calibration of Bolton (1986) stress-dilatancy Q and R parameters for (a) Westerly Beach sand; and (b) Golden Flint sand.

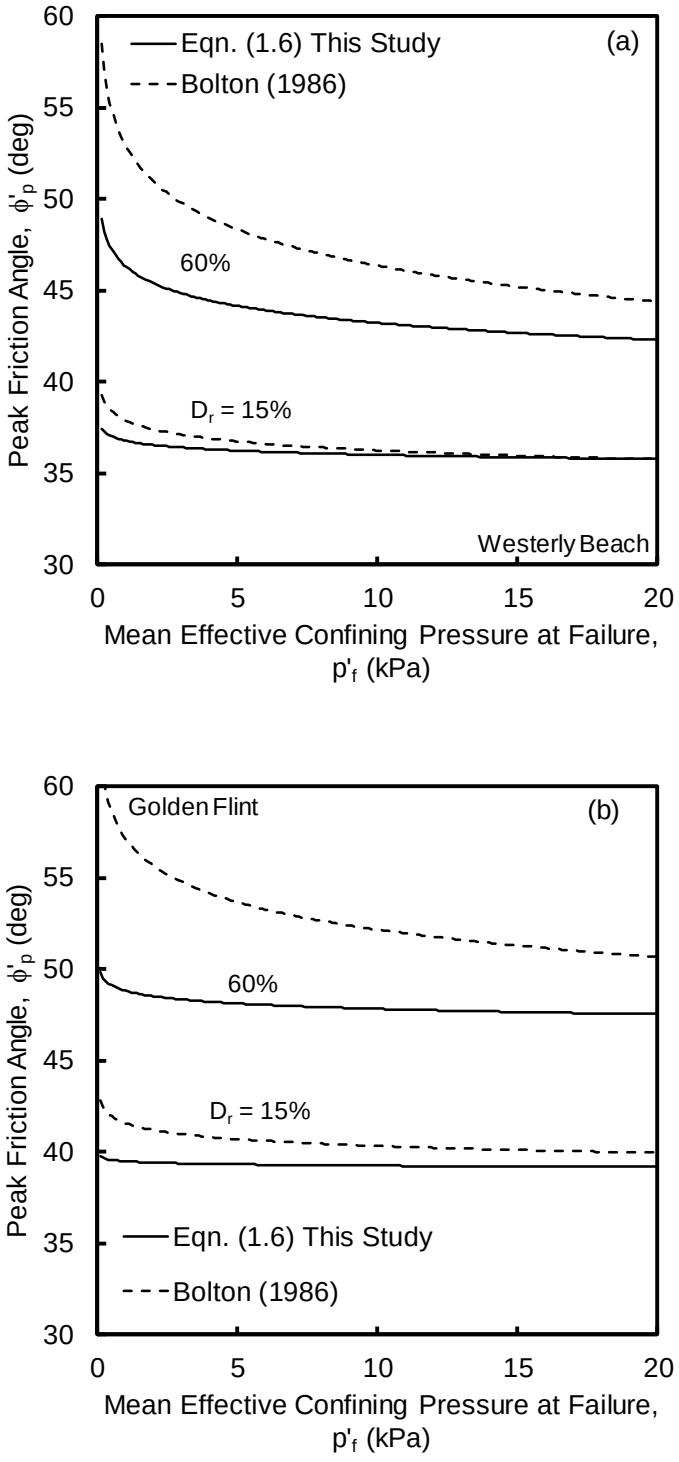

Figure 1.6. Comparison of the modified Bolton stress-dilatancy relationship regressed using tilt and triaxial test data and the standard Bolton (1986) stress-dilatancy relationship regressed using triaxial test data for: (a) Westerly Beach sand; and (b) Golden Flint sand.

2. The Effect of Shape on the Pullout Capacity of Plate Anchors in Sand

Prepared for submission to Geotechnique

Abstract

This paper presents an experimental study to investigate the effect of shape on the pullout capacity of horizontal plate anchors in sand. In addition, a nonassociated flow limit equilibrium solution for plane strain and axisymmetric conditions is proposed for asymmetric anchor shapes. Experimental results indicate a difference in the breakout factor (i.e. normalized capacity) over a range of embedment depths with respect to shape. Circular anchors produced consistently larger breakout factors relative to square anchors. With increasing embedment, the circle, equilateral triangular, and kite anchors become comparable within 5%. The proposed analytical model predicted breakout factors within 10% for circular plates and within, on average, 30% for the remaining shapes for a normalized embedment less than 5. Although additional study is warranted, the experimental results indicate a difference in capacity when altering the shape, and the solution procedure predicts pullout capacity within reason which in turn gives confidence in the further application of the analytical procedure.

Introduction

The offshore wind industry will likely move further offshore into deeper water to capture greater wind resources and to extend out of visual range of coastal communities (Musial et al. 2004). This will allow for the production of a significant amount of renewable energy without harmful emissions (Musial and Ram 2010). The major challenges with moving into deeper water is that conventional offshore foundations will become impractical and uneconomical due to the size and energy required for resisting environmental forces and installation. Thus, the most economical option will be floating substructures anchored to

the seafloor, which must provide enough buoyancy to support the weight of the turbine, and restrain from pitch, roll, and heave motions within acceptable limits (Musial and Butterfield 2006).

Floating platforms have been successfully used for oil and gas development in deep water; these platforms are secured by anchors attached to the structure via mooring systems. The mooring systems typically can be a taut, semi-taut, or catenary system attached to a variety of different anchors which include, but are not limited to, anchor piles, suction caissons, drag anchors, suction embedded plate anchors, and dynamically penetrating anchors (Randolph and Gourvenec 2011). However, plate type anchors have shown to provide an efficient means to resist vertical and inclined loading due to the resistance being mobilized over the bearing surface of the anchor, rather than in side shear that might be the case, for example, in a pile anchor.

The Author is currently researching a new anchor concept where a wing-like plate anchor is installed into the seabed using free-fall penetration, similar to a torpedo pile. The anchor will then rotate and move into position that is near normal to the anchor line under the applied mooring load (Gerkus et al. 2016). The shape of the anchor will likely take on non-axisymmetric and non-planar shapes so that it will remain hydrodynamically stable as it free-falls through the water column. It will be necessary to be able to predict the pullout capacity of the wing anchor after it achieves its final embedment.

A review of the literature, summarized in Table 2.1, indicates that most of the studies on the pullout capacity of horizontal plate anchors have focused primarily on either circular or rectangular anchors. Researchers (e.g. Murray and Geddes 1987; Merifield et al. 2006) have found that circular anchors have approximately 30% higher capacity than square anchors. Other studies (e.g. Rowe and Davis 1982; Sing and Ramaswamy 2008) have shown that circular and square anchors have higher capacities than rectangular anchors due to three-dimensional effects. It is unclear how shape might affect the capacity of other non-axisymmetric and/or non-planar shapes. As a starting point, the objective of this study is to investigate the pullout capacity of shallow embedded triangular and kite shaped anchors. Circular and square anchors are also included, however, to provide a baseline for comparison.

Experimental Program

As part of this study, 20 small-scale 1g physical model experiments were performed on various shaped anchors in dry sand. The anchor embedment ratio (H/B), where H is the depth from the ground surface to lowest point of the anchor and B is the diameter or plate width, varied from 1 to 5 in order to focus on shallow embedded anchors. As part of a preliminary development study on the wing-anchor concept after Gerkus et al. (2016), experimental penetration results following free-fall of a simple plate anchor indicated maximum normalized embedment's of 1 and 3 for saturated and dry sand, respectively. Furthermore, simple dive trajectory experiments in sand have shown the anchor to achieve one to two additional anchor width or diameter of embedment, therefore gearing the focus to shallow embedded anchors. Scale effects are important to consider so that the results can

be reliably interpreted. Bradshaw et al. (2016) showed that scale effects can be minimized in 1g plate anchor tests by presenting the pullout capacity in a dimensionless form, commonly referred to as a breakout factor ($N\gamma = q/\gamma H$), and by scaling the constitutive behavior of the soil. Soils will generally have a higher strength in small-scale 1g models due to higher dilation at low confining pressures. Therefore, the scaling of the constitutive behavior involves preparing the soil looser in the model than at full-scale to get a similar dilation response. Consistent with current centrifuge scaling laws presented in Garnier and Gaudin (2007), experiments were also designed such that the width of the anchors were at least 48 times the median diameter (D_{50}) of the sand to ensure there was a sufficient number of particles over the width of the plate.

A schematic of the anchor load test setup is shown in Figure 2.1. The sand used in this study was obtained from a natural deposit in Westerly, RI (Bradshaw et al. 2015; 2016) and consisted of uniform quartz grains with index properties provided in Table 2.2. To investigate the effect of shape on pullout capacity, circular, square, equilateral triangular, and kite shaped plate anchors were tested as shown in Figure 2.2. The anchors were fabricated from 12.7 mm thick structural steel with dimensions given in Table 2.3 and had either a plate area of 75 cm^2, 232 cm^2, or 929 cm^2. The anchors were "wished" into place and tested in a rigid test container having dimensions of 2.4 m length x 1.2 m width x 0.9 m height. Sand was dry pluviated using a portable pluviator adapted from Gade et al. (2013). The device consisted of a bucket attached to a flexible hose leading to a pipe containing a plate with holes and a stack of sieves. By varying the opening size, fall height of the sand, and amount of sieves, the density was easily controlled (Bradshaw et al. 2016).

The unit weight of the deposited soil was determined by dispensing sand into small cups of a known volume (413 cm^3), that were placed on the soil surface at various depths during pluviation. A typical profile of unit weight and corresponding relative density index (I_D), defined as $(e_{max}-e)/(e_{max}-e_{min})$ where e_{max}, e_{min} equal the maximum and minimum void ratios, and e equals the void ratio of the prepared sample, is shown in Figure 2.3. The relative density index was fairly uniform throughout the test container with a coefficient of variation less than 0.20.

The plate anchors were spaced at least 3B from the walls of the test container and the adjacent anchors to minimize interaction. The anchors were pulled out at a constant rate of 50 mm/s using an electric hoist, and a block and tackle system as shown in Figure 2.1. Loads were measured with a load cell with a capacity of 0.89, 2.2, or 11.1 kN (CAS SBA and Omega LC), and displacement was measured with a string potentiometer (Measurement Specialties SP2-50). The loading rate was significantly higher than other studies, but strain rates have shown to be negligible on the strength of dry sand (e.g. Whitman and Healy 1962) (Bradshaw et al. 2016). Table 2.4 summarizes the local soil properties and results of each plate anchor pullout test.

The peak friction and dilation angles were estimated using the Bolton (1986) stress-dilatancy relationship in order to handle the stress dependent changes in friction and dilation angles at low stresses. The relationship is expressed as

$$\phi'_p - \phi'_c = A_f \left(I_D \left[Q - \ln\left(p'_f\right) \right] - R \right) \quad (2.1)$$

$$\phi'_p - \phi'_c = \beta \psi_p \quad (2.2)$$

where ϕ'_c = the critical state friction angle, p'_f = the mean effective stress at failure, and Q, R, A_f, and β = Bolton's fitting parameters. Triaxial tests were performed to calibrate Bolton's fitting parameters for the sand used in this study. The triaxial samples were prepared using dry pluviation with a funnel in an attempt to achieve a similar fabric as the sand in the physical 1g model experiments. A range of relative density indices between 0.13 and 0.53 could be achieved by varying the opening size of the funnel. The critical state friction angle was determined from extrapolating the peak friction angle at zero dilation angle (Bolton 1986), and the fitting parameters (Q, R, A_f, β) were determined from the linear regression plots shown in Figures 2.4-2.6 (Bradshaw et al. 2016). A summary of the fitting parameters can be seen in Table 2.2.

Experimental Results

Figure 2.7 depicts the normalized load-displacement behavior obtained from the pullout tests conducted on circular, square, equilateral triangular, and kite plate anchors for an average relative density of 23% (I_D = 0.23). Three tests were performed at a higher relative density of 55% (I_D = 0.55) and can also be found in Table 2.4. It is apparent that the pullout capacity increases with increasing embedment and relative density regardless of the shape. All of the experimental tests show a clear peak capacity followed by a softening behavior due to the reduction in soil overburden and confining pressure as the anchor is pulled out of the soil. For anchor tests starting at H/B = 1 to 3, the peak pullout capacity occurred at

approximately 0.2B of displacement relative to the initial embedment depth. As the normalized embedment increased from 3 to 5, slightly more displacement (approximately 0.5B) was required before reaching the peak pullout capacity.

Figure 2.8a/b presents a comparison between the breakout factors obtained for circular and square plate anchors in this study with those found in literature from Dickin (1988), Murray and Geddes (1987; 1989), Pearce (2000), Illamparuthi et al. (2002), and Giampa et al. (2016). Although comparisons made between experimental results in literature are difficult due to uncertainty in the soil properties, anchor roughness, size, and sample preparation, they can provide a reasonable baseline for validation. The breakout factors for circular plate anchors are consistently larger than those of square plate anchors over a range of embedment depths. This trend is verified through the experimental results obtained in this study and in the literature. Additionally, the experimental capacities for circular and square plate anchors in this study are at minimum, 40% lower than those found in the majority of the literature which may be due primarily to the 4^{o} difference in soil strength. Majority of the literature presented in Figure 2.8 do not reference any scaling considerations to account for the strength or friction angle of the soil at low stresses. Therefore, the soil strength may in fact be greater than the published values, explaining the discrepancies in the pullout capacity values. However, the non-linear increase in breakout factor is comparable with a greater difference in values at shallower depths (H/B = 1 to 2). Overall, the breakout factors for circular and square anchors obtained from the literature, although larger, follow very similar trends and assist in the validity of the experiments performed in this study.

The breakout factors (i.e. peak pullout capacity) for each anchor shape in this study are shown in Figure 2.9 as a function of normalized embedment depth. Experimental studies from the literature indicate that circular plates have breakout factors that are 20% to 30% higher than square plates (i.e. Murray and Geddes 1987; Tagaya et al. 1988; Merifield et al. 2006). In this study the breakout factors for the circular plates were 30% to 50% higher than those for the square plates. The kite and equilateral triangular anchors had a breakout factor that was comparable to the square anchors at an embedment ratio less than 2. For higher embedment ratios, the breakout factors of the kite and equilateral triangular anchors moved closer to the breakout factor of the circular plate. A reason for this change may be linked to the symmetry of the anchors. The axisymmetry and dilation may be causing an increase in the intermediate principle stress in a direction that is tangential to the failure surface, that is subsequently increasing the strength on the failure plane.

Nonassociated Limit Equilibrium Solutions for Pullout Capacity

Analyses to predict the pullout capacity of plate anchors in sand are typically based solely on peak friction angle (Meyerhof and Adams 1968; Vesic 1971; Sarac 1989; Ghaly and Hanna 1994; Illamparuthi et al. 2002; Merifield et al. 2006). These solutions are either based on the principle of associated flow, where $\psi_p = \phi'_p$, or they inherently assume that the friction angle can uniquely capture the influence of dilation angle. Researchers including Davis (1968), Drescher and Detournay (1993), Loukidis et al. (2008), Krabbenhoft et al. (2012), Sloan (2012), and Giampa et al. (2016) have shown that the assumption of associated flow does not reflect drained soil behavior, and overpredicts drained foundation capacity in soils. Therefore, dilation angle should be directly included

in the analysis of pullout capacity of shallow anchors. A nonassociated limit equilibrium solution presented by White et al. (2008) for plane strain conditions and Giampa et al. (2016) for axisymmetric conditions has shown to capture the influence of dilation on the pullout capacity of shallow embedded anchors within 15% of the measured values.

Solutions to predict the pullout capacity of shallow embedded anchors have been primarily developed for plane strain or axisymmetric conditions. The Author is unaware of any available closed-form theoretical solutions to predict the pullout capacity of shallow embedded asymmetric plate anchors. Therefore, a nonassociated limit equilibrium solution is adapted herein from Giampa et al. (2016) to assess the breakout factor, $N\gamma$, for the shapes used in this study. The axisymmetric solution after Giampa et al. (2016) was adapted from White et al. (2008) with an assumed failure wedge shown in Figure 2.10. The failure wedge assumes the inclination angle (θ) of the failure surface is equal to the dilation angle of the soil (i.e. nonassociated flow). This assumption has been further verified experimentally by Cheuk et al. (2007) and Liu et al. (2012). White et al. (2008) states that the pullout resistance is equal to the weight of the lifted soil wedge plus the shear resistance along the two inclined failure surfaces. The weight of the soil wedge is taken as the volume of a two-dimensional trapezoid, while the shear resistance, assuming only frictional energy dissipation is considered on the failure surface, can be expressed as

$$\tau = C_1 \gamma z \left(\tan \phi'_p - \tan \psi_p \right) \tag{2.3}$$

$$C_1 = \frac{(1+K_0)}{2} - \frac{(1-K_0)\cos(2\psi_p)}{2} \tag{2.4}$$

Where τ = peak-mobilized shear resistance; γ = dry unit weight of sand; z = the height from the top to the bottom of the failure wedge; K_0 = lateral earth pressure coefficient at-rest; ψ_p = peak dilation angle; ϕ'_p = peak friction angle; and C_1 = constant for assessing the normal stress on the failure plane. Furthermore, Eqn. (2.4) is derived assuming that the normal stress on the failure surface does not change during uplift loading and is equal to the in situ value inferred from K_0 conditions (White et al. 2008). By integrating Eqn. (2.3) and (2.4) along the two-dimensional slip planes and equating with the vertical forces acting on the sliding block, the peak uplift resistance for plane strain is calculated as

$$Q_u = \gamma HB + \gamma H^2 \tan\psi_p + \gamma H^2 (\tan\phi'_p - \tan\psi_p) \times \left[\frac{1+K_0}{2} - \frac{(1-K_o)\cos 2\psi_p}{2} \right] \tag{2.5}$$

Where H = embedment depth from the ground surface to the deepest point of the anchor; and B = diameter or plate width (typically taken as the smallest dimension). Thus, normalizing Eqn. (2.5) by γAH, where A is the bearing area of the plate anchor, the breakout factor for plane strain conditions can be simplified as

$$N_\gamma = 1 + F_{ps}\left(\frac{H}{B}\right) \tag{2.6}$$

$$F_{ps} = \tan\psi_p + C_1(\tan\phi'_p - \tan\psi_p) \tag{2.7}$$

Where F_{ps} = pullout factor for plane strain conditions. Alternatively, a similar approach was used by Giampa et al. (2016) for axisymmetric conditions. Rather than representing the soil wedge as a two-dimensional trapezoid, Giampa et al. (2016) used a frustum obeying a nonassociated flow rule in which the uplifted weight can be generally expressed as

$$W_w = \frac{\gamma H}{3}\left(A_T + A + \sqrt{A_T A}\right) \tag{2.7}$$

Where A_T = area of the plate projected to the ground surface assuming $\theta = \psi_p$; and A = bearing area of the plate anchor.

Consistent with the assumptions made by White et al. (2008) that only frictional energy dissipation is considered on the failure surface; the peak-mobilized shear resistance becomes synonymous to Eqn. (2.3). Integrating Eqn. (2.3) along the failure surface represented as a frustum or three-dimensional wedge, combining with Eqn. (2.7), and normalizing by γAH, the breakout factor for a circular plate is defined as

$$N_\gamma = 1 + F_1\left(\frac{H}{B}\right) + F_2\left(\frac{H}{B}\right)^2 \tag{2.8}$$

$$F_1 = X_1\left[\tan\psi_p + C_1\left(\tan\phi'_p - \tan\psi_p\right)\right] \tag{2.9}$$

$$F_2 = X_2 \tan\psi_p\left[\tan\psi_p + C_1\left(\tan\phi'_p - \tan\psi_p\right)\right] \tag{2.10}$$

$$C_1 = \cos(\phi'_p - \psi_p) \quad (2.11)$$

Where X_1, X_2 = anchor dependent coefficients = 2 and 4/3, respectively for a circle; and C_1 = constant for assessing the normal stress on the failure plane. Giampa et al. (2016) proposed a first-order approximation of the constant C_1 that differs from White et al. (2008). The approximation was based on analyses of strip anchors in a nonassociated flow Coulomb soil (Rowe and Davis 1982; Vermeer and Sutjiadi 1985; Koutsabeloulis and Griffiths 1989; White et al. 2008; Smith 2012). Giampa et al. (2016) concluded K_0 has a minor influence on pullout capacity and C_1 is approximately $\cos(\phi'_p)$ for $\psi_p = 0$, and C_1 can be unity for $\psi_p = \phi'_p$, thus the constant can be represented by Eqn. (2.11). Additionally, for $\psi_p = \phi'_p$ (associated flow) Eqn. (2.8) becomes an upper bound solution where $F_1 = X_1\tan(\phi'_p)$ and $F_2 = X_2\tan^2(\phi'_p)$ (e.g. Murray and Geddes 1987).

The solution procedure presented by Giampa et al. (2016) was extended to square, equilateral triangular, and kite shaped plate anchors. The calculated soil wedge weights (i.e. Eqn. (2.7)) were verified numerically using SolidWorks for frustums inclined over a range of angles, from 0^o to ϕ'_p, and embedment depths. For shallow embedded square and equilateral triangular plate anchors, the breakout factor can be expressed in a form identical to Eqns. (2.8-2.10). The constants X_1 and X_2 are equal to 2 and 4/3 for square anchors, and $2\sqrt{3}$ and 4 for equilateral triangular anchors. The kite anchor can be simplified to a slightly different form due to the geometry of the shape and is expressed as

$$N\gamma = \frac{2}{3} + \left(\frac{2H\tan\psi_p}{3BL}\right)T_1 + \left(\frac{2}{3BL}\right)T_2 + \left(\frac{a_1H + a_2H}{BL}\right)T_3 + \frac{H^2}{BL}\left(\frac{1}{\cos\alpha_1} + \frac{1}{\cos\alpha_2}\right)T_4 \quad (2.12)$$

Where L = largest dimensions of the anchor; $T_1 = \left(\frac{B}{\cos\alpha_1} + \frac{L}{\cos\alpha_2} + \frac{2H\tan\psi_p}{\cos\alpha_1\cos\alpha_2}\right)$;

$T_2 = \sqrt{\frac{1}{4}B^2L^2 + \frac{1}{2}BLH\tan\psi_p T_1}$; $T_3 = 2C_1\left(\tan\phi'_p - \tan\psi_p\right)$; $T_4 = 4C_1\tan\psi_p\left(\tan\phi'_p - \tan\psi_p\right)$

; and a_1,a_2 = length of the diagonals; and α_1,α_2 = one half of the interior angles. In order to assess the newly derived solutions, the constant C_1 was varied between Eqns. (2.4) and (2.11).

Comparison of Analytical Expressions with Experimental Results

Table 2.5 shows the tabulated results comparing the predicted and measured breakout factors using the solutions presented in Eqn. (2.8) for a circular, square, and equilateral triangular anchor, and Eqn. (2.12) for a kite anchor. The constant C_1 was varied between Eqns. (2.4) and (2.11) to investigate the quality of the solution with respect to shape. A statistical assessment is also shown in Table 2.6. Figure 2.11 shows the $N\gamma$ ratio of predicted to measured, for each shape, using both C_1 constants. The results indicate that the pullout capacity of circular plate anchors (Figure 2.11d) is predicted within approximately 10% to 15% of the measured value with a coefficient of variation (COV) equal to 0.18, when using Eqn. (2.11) to estimate the normal stress along the failure plane. This finding is consistent with Giampa et al. (2016) for helical anchors and further validates the solution for circular plate anchors. Conversely, when using Eqn. (2.4) the results for

circular anchors are predicted within 20% to 40% of the measured values; thus, making the solution much more conservative.

The $N\gamma$ bias for the square, equilateral triangular, and kite plate anchors are shown in Figure 2.11a/b/c, respectively. For normalized embedment's, $H/B \leq 3$, the closed-form solution predicts capacity within approximately 30% for the aforementioned shapes when using Eqn. (2.4) rather than Eqn. (2.11) to assess the normal stress on the failure plane. Eqn. (2.4) assumes K_0 conditions which reduces the value by approximately one-half relative to Eqn. (2.11). This in turn decreases the predicted breakout factor and brings the bias closer to 1 for square, equilateral triangular, and kite plate anchors. The difference is clearly highlighted in Figure 2.11a/b/c represented by the open markers.

The sharp spike found in Figure 2.11 at $H/B \geq 5$ may be explained by the anchor moving into a transition or deep failure mode in which the slip surface becomes more localized around the plate. Therefore, the current solution becomes unsuitable for predicting pullout capacity due to the assumed failure wedge extending from the anchor plate to the ground surface. Although additional study is warranted to assess C_1 for non-circular plate anchors, Eqn. (2.4) is recommended to provide more conservatism when predicting pullout capacity.

Shape Factors

The effect of shape on the pullout resistance may be expressed as a dimensionless shape factor (S.F.) as

$$S.F. = \frac{N\gamma_{square,circle,Eq.Triangle,Kite}}{N\gamma_{strip}} \tag{2.13}$$

$$S.F. = \frac{N\gamma_{square,Eq.Triangle,Kite}}{N\gamma_{circle}} \tag{2.14}$$

Where the values of $N\gamma_{strip}$, $N\gamma_{circle}$ have been obtained from the work of White et al. (2008) and Giampa et al. (2016), respectively. For the purposes of numerical modeling it is convenient to model the pullout resistance under plane strain or axisymmetric conditions. Therefore, the use of shape factors will provide a means to adjust the resistance to a given shape. The breakout factors for a circular, square, equilateral triangular, and kite plate anchors are based on the present solution derivation with the recommended C_1 constant, and are compared to the plane strain solution of White et al. (2008) and the axisymmetric solution of Giampa et al. (2016). The shape factors expressed in Eqn. (2.13) and (2.14) are presented over a range of dilation angles and normalized embedment depths as shown in Figures 2.12 and 2.13, respectively.

For the shape factors shown in Figure 2.12 it is evident that dilation and embedment significantly increase capacity of circular, square, equilateral triangular, and kite plate anchors as compared to strip anchors. However, this trend is not quite similar when compared to the capacity of circular plate anchors. Figure 2.13a indicates that the capacity of circular plate anchors is larger than square plate anchors with increasing dilation and embedment depth. The trend is similar for the remaining shapes shown in Figure 2.13b/c at ψ_p equal to 0^o; however, as dilation angle increases the capacity of an equilateral

triangular and kite plate anchor become larger than circular plate anchors. This trend is in opposition with the experimental results and may be explained by the solutions' overprediction of pullout capacity for the equilateral triangular and kite shaped plate anchors. However, if the solutions predictions resulted in a mean bias closer to 1, the shape factors for $\psi > 0^o$ would mimic the behavior shown in Figure 2.13a for square plate anchors.

For comparison purposes Figure 2.14 presents shape factors based on the nonassociated flow limit equilibrium solution for circular and square anchors, and compares them to those presented by Merifield et al. (2006), Vesic (1971), and Koutsabeloulis and Griffiths (1989). Similar to previous findings, dilation and embedment depth increase capacity of circular and square anchors as compared to strip anchors, however it is noted that shape factors using the associated flow case of the limit equilibrium solution (upper bound) in Eqns. (2.8-2.11) match well with the lower bound published by Merifield et al. (2006). The associated flow case will tend to overpredict shape factors as compared to the nonassociated flow case. Shape factors based on the Vesic (1971) cavity expansion solution are slightly lower to shape factors based on the nonassociated flow limit equilibrium solution for the case when $\psi_p > 10^o$ (e.g. $\phi'_p > 39^o$). While shape factors from the nonassociated flow limit equilibrium and cavity expansion solution compare reasonably well with those of Koutsabeloulis and Griffiths (1989) up to H/B equal to 4 for $\phi'_p > 40^o$, the axisymmetric solution of Koutsabelouslis and Griffiths (1989) does not explicitly account for dilation angle and may significantly overpredict shape factors for 'loose' sands ($\psi_p < 10^o$) and H/B greater than 5.

Conclusions

The objective of this study was to investigate the effect shape has on the pullout capacity of shallow embedded plate anchors in sand. Twenty small-scale 1g physical model experiments were performed on various plate anchors including circular, square, equilateral triangular, and kite shapes to assess the effect on pullout capacity. A general procedure to derive closed-form nonassociated flow limit equilibrium solutions for the aforementioned shapes is also presented. The solutions were compared to the respective shapes in order to test the quality of the model.

The experimental results indicate differences in breakout factor, over a range of embedment ratios with respect to shape. Consistent with literature, the capacity of circular plate anchors is 30% to 50% larger than square anchors. Additionally, as the embedment ratio increases ($H/B > 2$) the breakout factor for a circle, kite and equilateral triangular anchor become comparable, and are all larger than a square anchor. The change may be linked to an increase in the intermediate principle stress (i.e. tangential to the failure surface), that is increasing the strength on the failure plane. The analytical expressions extended to the shapes used in this study agree well with the experimental test results when selecting the appropriate normal stress constant, C_1. Pullout capacity for circular plate anchors were predicted within 10% with a COV of 0.18 when $C_1 = \cos(\phi'_p-\psi_p)$. Conversely, capacity of the square, equilateral triangular, and kite plate anchors were predicted within 30% when $C_1 = (1+K_0)/2-(1-K_0)\cos(2\psi_p)/2$ was used. The lateral earth pressure coefficient at-rest reduced the C_1 value by one half, which in turn lowered the

predicted breakout factor for all shapes, but significantly improved the quality of the solutions for the non-circular or asymmetric plate anchors. It is recommended for design purposes that C_1 shown in Eqn. (2.4) be used for shallow embedded, non-circular plate anchors to conservatively predict pullout capacity.

From the analytical expressions derived in this study, shape factors were developed comparing the capacity of the square, equilateral triangular, and kite shapes to the capacity of a strip (plane strain) and circular (axisymmetric) anchor. The shape factor results indicated that the capacity of square, equilateral triangular, and kite anchors are larger than a strip anchor with increasing dilation and embedment depth. This trend was also evident for the capacity of equilateral triangular and kite shapes when compared to circular anchors for dilation angles greater than 0^o. However, the capacity of a square anchor is smaller than a circular anchor over a range of dilation angles and embedment depths, as well as, equilateral triangular and kite anchors when $\psi_p = 0^o$.

Lastly, comparisons of the nonassociated limit equilibrium model for circular (Giampa et al. 2016) and square (this study) anchors were made with solutions presented by Merifield et al. (2006), Vesic (1971), and Koutsabeloulis and Griffiths (1989). Shape factors agreed well with lower bound shape factors of Merifield et al. (2006) when associated flow was assigned. Similarly, shapes factors based on Vesic (1971) cavity expansion solution were very similar to shape factors based on the nonassociated flow limit equilibrium solution for

circular plate anchors when $\psi_p > 10^o$; both solutions also compared reasonably well with Koutsabeloulis and Griffiths (1989) up to H/B = 4 for $\phi'_p > 40^o$.

Further assessment of the analytical solution procedure may be warranted for additional shapes, sand types, layering configurations, and the normal stress coefficient for non-circular plate anchors. However, the reasonable agreement among the analytical and experimental results gives confidence in the further application of the simple limit equilibrium analytical solution method presented in this study, which can be used for asymmetrical or non-standard shallow embedded plate anchors. Additional experimental testing may be warranted to study the failure mechanisms of axisymmetric plate anchors to further clarify the observed differences in breakout factors.

Acknowledgments

This material is based upon work supported by the National Science Foundation under Grant No. 1300142 and also by the Science Foundation Ireland under the U.S.-Ireland R&D Partnership Program Grant No. SFI/2012/US/E2479. The Author would also like to thank Kevin Broccolo at the University of Rhode Island for all of his fabrication efforts put forth to conduct this research.

References

Andreadis, A., Harvey, R.C., and Burley, E. (1981). "Embedded anchor response to uplift loading." *J. Geotech. Engrg. Div.*, 107(1), 59-78.

Bolton, M. (1986). "The strength and dilatancy of sands." *Geotechnique*, 36(1), 65–78.

Bradshaw, A.S., Giampa, J., Dietrich, F., Gilbert, R.B., and Gerkus, H. (2015). "Pullout Capacity of Plate Anchors in Sand for Floating Offshore Wind Turbines." *Proc., of the 3rd Inter. Symp. on Frontiers in Offshore Geotechnics*, Oslo, Norway: NGI. 833-838.

Bradshaw, A.S., Giampa, J.R., Gerkus, H., Jalilvand, S., Fanning, J., Nanda, S., Gilbert, R., Gavin, K., and Sivakumar, V. (2016). "Scaling Considerations for 1-g Model Horizontal Plate Anchor Tests in Sand." *Geotech. Testing J.*, 39 (6), 1-9.

Bouazza, A. and Finlay, T.W. (1990). "Uplift capacity of plate anchors in a two-layered sand." *Geotechnique*, 40(2), 293-297.

Cheuk, C., White, D., and Bolton, M. (2007). "Uplift mechanisms of pipes buried in sand." *J. Geotech. Geoenviron. Engrg.*, 2(154), 154–163.

Das, B.M. and Seeley, G.R. (1975a). "Breakout resistance of shallow horizontal anchors." *J. Geotech. Engrg. Div.*, 101(GT9), 995-1008.

Das, B.M. and Seeley, G.R. (1975b). "Inclined load resistance of anchors in sand." *J. Geotech. Engrg. Div.*, 101(9), 999-1003.

Davis, E.H. (1968). "Theories of plasticity and the failure of soil masses." *Soil mechanics: selected topics*, I. K. Lee, ed., Butterworths, London, 341–380.

Dickin, E.A. (1988). "Uplift behavior of horizontal anchor plates in sand." *J. Geotech. Engrg. Div.*, 114(11), 1300-1317.

Dickin, E.A. and Laman, M. (2007). "Uplift response of strip anchors in cohesionless soil." *J. Adv. Eng. Softw.*, 1(38), 618-625.

Drescher, A., and Detournay, E. (1993). “Limit load in translational failure mechanisms for associative and non-associative materials.” *Geotechnique*, 43(3), 443–456.

Fargic, L. and Marovic, P. (2003). “Pullout capacity of spatial anchors.” *J. Eng. Comput.*, 21(6), 598-700.

Frydman, S. and Shamam, I. (1989). “Pullout capacity of slab anchors in sand.” *Can. Geotech. J.*, 26(3), 385-400.

Gade, V.K., Dave, T.N., Chauhan, V.B., and Daska, S.M., 2013, “Portable traveling pluviator to reconstitute specimens of cohesionless soils,” *Proc. of Indian Geotech. Conf.*, University in Roorkee, India.

Garnier, J., Gaudin, C., Springman, S.M., Culligan, P.J., Goodings, D., Konig, D., Kutter, B., Phillips, R., Randolph, M. F., and Thorel, L. (2007). “Catalogue of scaling laws and similitude questions in geotechnical centrifuge modeling.” *Int. J. Phys. Modell. Geotech.*, 7(3), 1-23.

Gerkus, H., Giampa, J.R., Senanayake, A.I., Lai, Y., Huang, Y., Flores, J. E.I., Breithaupt, N.B., Sivarajah, S., Bradshaw, A. S., and Gilbert, R.B. (2015). “Preliminary development of a new concept to improve sustainability of offshore foundations.” *Proc. Geo-Congress Conference*, ASCE, IL.

Ghaly, A., and Hanna, A. (1994). “Ultimate pullout resistance of single vertical anchors.” *Can. Geotech. J.*, 31(5), 661–672.

Giampa, J.R., Bradshaw, A.S., and Schneider, J.A. (2016). “Influence of Dilation Angle on Drained Shallow Circular Anchor Uplift Capacity,” Int. J. Geomech., 17(2).

Hanna, T.H. and Carr, R.W. (1971). “The loaing behavior of plate anchors in normally and over consolidated sands.” *Proc., 4th Int. Conf. on Soil Mech. and Fnd. Engrg.*, Budapest, 589-600.

Hanna, T.H., Sparks, R., Yilmaz, M. (1971). “Anchor behavior in sand.” *J. Soil Mech. Fnd. Div.*, 98(11), 1187-1208.

Ilamparuthi, K., Dickin, E.A., and Muthukrisnaiah, K. (2002). “Experimental investigation of the uplift behavior of circular plate anchors embedded in sand.” *Can. Geotech. J.*, 39(3), 648–664.

Koutsabeloulis, N.C., and Griffiths, D.V. (1989). “Numerical modelling of the trap door problem.” *Geotechnique*, 39(1), 77–89.

Krabbenhoft, K., Karim, M.R., Lyamin, A.V., and Sloan, S.W. (2012). “Associated computational plasticity schemes for nonassociated frictional materials.” *Int. J. Numer. Methods Engrg.*, 90(9), 1089–1117.

Liu, J., Liu, M., and Zhu, Z. (2012). “Sand deformation around an uplift plate anchor.” *J. Geotech. Geoenviron. Eng.*, 728–737.

Loukidis, D., Chakraborty, T., and Salgado, R. (2008). “Bearing capacity of strip footings on purely frictional soil under eccentric and inclined loads.” *Can. Geotech. J.*, 45(6), 768–787.

Merifield, R., Lyamin, A., and Sloan, S. (2006). “Three-dimensional lowerbound solutions for the stability of plate anchors in sand.” *Geotechnique*, 56(2), 123–132.

Meyerhof, G. and Adams, J. (1968). “The ultimate uplift capacity of foundations. “*Can. Geotech. J.*, 5(4), 225–244.

Murray, E. and Geddes, J. (1987). “Uplift of anchor plates in sand.” *J.Geotech Engrg.*, 3(202), 202–215.

Murray, E.J. and Geddes, J.D. (1989). “Passive inclined anchorages in sand.” *J. Geotech. Engrg.*, 117(5), 810-814.

Musial, W., Butterfield, S., and Boone, A. (2004). “Feasibility of floating platform systems for wind turbines.” *Proc. 23rd ASME Wind Energy Symp.*, Reno, NV.

Musial, W. and Butterfield, S. (2006). “Energy from offshore wind.” *Offshore Technology Conference*, Houston, TX.

Musial, W. and Ram, B. (2010). “Large-scale offshore wind power in the United States.” `National Renewable Energy Laboratory.

Niroumand, H., Kassum, K.A., and Nazir, R. (2010). “Experimental studies of horizontal square anchor plates in cohesionless soil.” *Electron J. Geotech. Engrg.*, 15, 609-620.

Niroumand, H. and Kassum, K.A. (2014a). “Square plates as symmetrical anchor plates under uplift test in loose sand.” *Geomechanics and Engineering*, 6(6), 593-612.

Niroumand, H. and Kassum, K.A. (2014b). “Uplift response of irregular-shaped anchor in cohesionless soil.” *Arab J. Sci. Engrg.*, 39, 3511-3524.

Ovesen, N.K. (1981). “Centrifuge tests of the uplift capacity of anchors.” *Proc., 10th Int. Conf. on Soil Mech. and Fnd. Engrg.*, Stockholm, 717-722.

Pearce, A. (2000). “Experimental investigation into the pullout capacity of plate anchors in sand.” MSc thesis, University of Newcastle, Australia.

Randolph, M. and Gourvenec, R. (2011). *Offshore geotechnical engineering*, New York, USA: Spon Press.

Rowe, R.K., and Davis, E. (1982). “The behaviour of anchor plates in sand.” *Geotechnique*, 32(1), 25–41.

Saeedy, H.S. (1987). “Stability of circular vertical anchors.” *Can. Geotech. J.*, 24(3), 452-456.

Sakai, T., and Tanaka, T. (1998). “Scale effect of a shallow circular anchor in dense sand.” *Soils Found.*, 38(2), 93–99.

Sarac, D.Z. (1989). “The uplift capacity of shallow buried anchor slabs.” *Proc., 12th Int. Conf. on Soil Mech. and Fnd. Engrg.*, Balkema, Rotterdam, Netherlands, 2, 1213–1218.

Sing, S.P. and Ramaswamy, S.V. (2008). “Effect of shape on holding capacity of plate anchors buried in soft soil.” *Geomechanics and Geoengineering*, 3(2), 157-166.

Sloan, S.W. (2013). “Geotechnical stability analysis.” *Geotechnique*, 63(7), 531-572.

Smith, C. (1998). “Limit loads for an anchor/trapdoor embedded in an associative Coulomb soil.” *Int. J. Numer. Anal. Methods Geomech.*, 22(11), 855–865.

Smith, C.C. (2012). “Limit loads for a shallow anchor/trapdoor embedded in a non-associative Coulomb soil.” *Geotechnique*, 62(7), 563–571.

Tagaya, K., Scott, R. F., and Aboshi, H. (1988). “Pullout resistance of buried anchors in sand.” *Soil. Found.*, 28(3), 114-130.

Vermeer, P.A., and Sutjiadi, W. (1985). “The uplift resistance of shallow embedded anchors.” *Proc., 11th Int. Conf. on Soil Mech. and Fnd. Engrg.*, Balkema, Rotterdam, Netherlands, 3, 1635–1638.

Vesic, A.S. (1971). “Breakout resistance of objects embedded in ocean bottom.” *Soil Mech. Fnd. Engrg. Div.*, 97(9), 1183–1205.

White, D.J., Cheuk, C.Y., and Bolton, M. (2008). “The uplift resistance of pipes and plate anchors buried in sand.” *Geotechnique*, 58(10), 771–779.

Whitman, R. V. and Healy, K. A., 1962, “Shear Strength of Sands During Rapid Loadings,” *J. Soil Mech. Found. Div.*, 88(SM2), 99–131.

Table 2.1. Summary of experimental tests on horizontal anchors in sand found in literature.

Reference	Type of Testing	Anchor Shape	Anchor Size (mm)
Meyerhof and Adams (1968)	Model-Scale	Circ.	25.4 to 102
Hanna and Carr (1971)	1g	Circ.	38
Hanna et al. (1971)	Chamber and Field	Circ.	38, 150
Vesic (1971)	1g	Circ.	
Das and Seeley (1975a/b)	1g	Sqr., Rect.	51
Andreadis et al. (1981)	1g	Circ.	80 , 150
Ovesen (1981)	Centrifuge and Field	Circ., Sqr.	20
Rowe and Davis (1982)	1g	Sqr., Rect.	51
Murray and Geddes (1987)	1g	Circ., Rect.	50.8
Saeedy (1987)	1g	Circ.	37.8-75.6
Dickin (1988)	Centrifuge and Chamber	Sqr., Rect.	25, 50
Tagaya et al. (1988)	Centrifuge	Circ., Rect.	15
Frydman and Shamam (1989)	Chamber and Field	Strip, Rect.	19, 200
Murray and Geddes (1989)	1g	Sqr., Rect.	50.8
Bouazza and Finlay (1990)	1g	Circ.	37.5
Sakai and Tanaka (1998)	1g	Circ.	30, 200
Pearce (2000)	1g	Circ.	50-125
Illamparuthi et al. (2002)	1g	Circ.	100-400
Fargic and Marovic (2003)	1g and Field	Spatial	25, 50, 100

Table 2.1. Continued…

Reference	Type of Testing	Anchor Shape	Anchor Size (mm)
Dickin and Laman (2007)	Centrifuge	Strip	100, 250
Niroumand et al. (2010)	1g	Sqr.	50, 75
Niroumand and Kassim (2014a)	1g	Sqr.	50, 75, 100
Niroumand and Kassim (2014b)	1g	Irregular	159, 297
Bradshaw et al. (2015)	1g	Sqr.	152, 305
Bradshaw et al. (2016)	1g	Sqr.	152, 305
Giampa et al. (2016)	1g	Helical	152, 254

Table 2.2. Properties of test sand.

Property	Value
γ_{max} (kN/m^3)	18.1
γ_{min} (kN/m^3)	14.1
e_{min}	0.44
e_{max}	0.84
D_{50} (mm)	0.30
G_s	2.65
ϕ'_c (deg)	32.3
Q	7.03
R	-0.12
A_f	4.75
β	0.69

Table 2.3. Dimensions of test anchors used in this study.

Dimensions	Square (large)	Square (small)	Circle	Equilateral Triangle (large)	Equilateral Triangle (small)	Kite (large)	Kite (small)
B (mm)	304.8	152.4	165.1	231	127	198	127
L (mm)	304.8	152.4	165.1	231	127	236	127
Diagonal long (mm)	-	-	-	-	-	197	127
Diagonal short (mm)	-	-	-	-	-	127	66
t (mm)	12.7	12.7	12.7	12.7	12.7	12.7	12.7
A (cm^2)	929	232	214	232	70	234	81

Table 2.4. Summary of local soil properties and plate anchor test results.

Test ID	Shape	γ (kN/m3)	ϕ'_p (deg)	ψ_p (deg)	B & L (m)	H (m)	H/B	Q_u (N)	$N\gamma$
1	Square	14.91	40.2	11.4	0.152	0.152	1.0	90	1.7
2	Square	14.91	39.4	10.3	0.152	0.305	2.0	255	2.4
3	Square	14.85	39.7	10.7	0.152	0.152	1.0	96	1.8
4	Square	14.85	38.5	9.0	0.152	0.457	3.0	706	4.5
5	Square	14.85	38.9	9.6	0.305	0.305	1.0	720	1.7
19	Square	14.72	37.1	7.0	0.152	0.762	5.0	1492	5.7
22	Square	16.05	48.9	24.1	0.152	0.152	1.0	125	2.2
15	Eq. Triangle	14.78	38.7	9.3	0.231	0.231	1.0	174	2.2
16	Eq. Triangle	14.78	38.0	8.2	0.231	0.462	2.0	687	4.3
17	Eq. Triangle	14.78	37.6	7.7	0.231	0.693	3.0	1384	5.8
20	Eq. Triangle	14.72	37.3	7.2	0.127	0.635	5.0	494	7.6
23	Eq. Triangle	16.05	46.0	19.9	0.231	0.462	2.0	1222	7.1
12	Kite	14.81	38.9	9.6	0.198 & 0.236	0.236	1.2	173	2.1
13	Kite	14.81	38.2	8.5	0.198 & 0.236	0.472	2.4	613	3.7
14	Kite	14.81	37.9	8.1	0.198 & 0.236	0.638	3.2	1355	6.1
18	Kite	14.72	37.3	7.2	0.127 & 0.127	0.635	5.0	498	6.6
21	Kite	16.05	46.0	19.8	0.198 & 0.236	0.472	2.4	1353	7.6
24	Circle	14.90	40.1	11.2	0.165	0.165	1.0	181	3.4
25	Circle	14.90	39.2	10.1	0.165	0.330	2.0	524	5.0
26	Circle	14.90	38.8	9.4	0.165	0.495	3.0	935	5.9

Table 2.5. Comparison of experimental results to analytical expressions.

Test ID	Shape	Experimental Nγ	Predicted Nγ*	Pred./Meas.	Predicted Nγ**	Pred./Meas.
1	Square	1.7	2.7	1.6	2.2	1.3
2	Square	2.4	4.7	1.9	3.4	1.4
3	Square	1.8	2.7	1.5	2.1	1.2
4	Square	4.5	6.6	1.5	4.7	1.0
5	Square	1.7	2.6	1.5	2.1	1.2
19	Square	5.7	10.4	1.8	6.9	1.2
22	Square	2.2	3.8	1.7	3.2	1.4
15	Eq. Triangle	2.2	4.0	1.8	2.9	1.3
16	Eq. Triangle	4.3	7.4	1.7	5.1	1.2
17	Eq. Triangle	5.8	11.4	2.0	7.6	1.3
20	Eq. Triangle	7.6	21.3	2.8	13.8	1.8
23	Eq. Triangle	7.1	13.3	1.9	10.1	1.4
12	Kite	2.1	4.7	2.2	2.4	1.1
13	Kite	3.7	10.4	2.8	5.2	1.4
14	Kite	6.1	15.4	2.5	8.0	1.3
18	Kite	6.6	32.5	4.9	19.0	2.9
21	Kite	7.6	21.0	2.8	13.2	1.7
24	Circle	3.4	2.7	0.8	2.2	0.6
25	Circle	5.0	4.6	0.9	3.4	0.7
26	Circle	5.9	6.8	1.1	4.8	0.8

Table 2.6. Statistical assessment of analytical expressions based on experimental data.

	Pred./Meas. $C_1=\cos(\phi'_p-\psi_p)$		Pred./Meas. $C_1=(1+K_0)/2 - (1-K_0)\cos(2\psi_p)/2$	
Shape	Median	COV	Median	COV
Square	1.61	0.11	1.21	0.11
Eq. Triangle	1.87	0.22	1.33	0.17
Kite	2.76	0.35	1.39	0.41
Circle	0.93	0.18	0.68	0.13

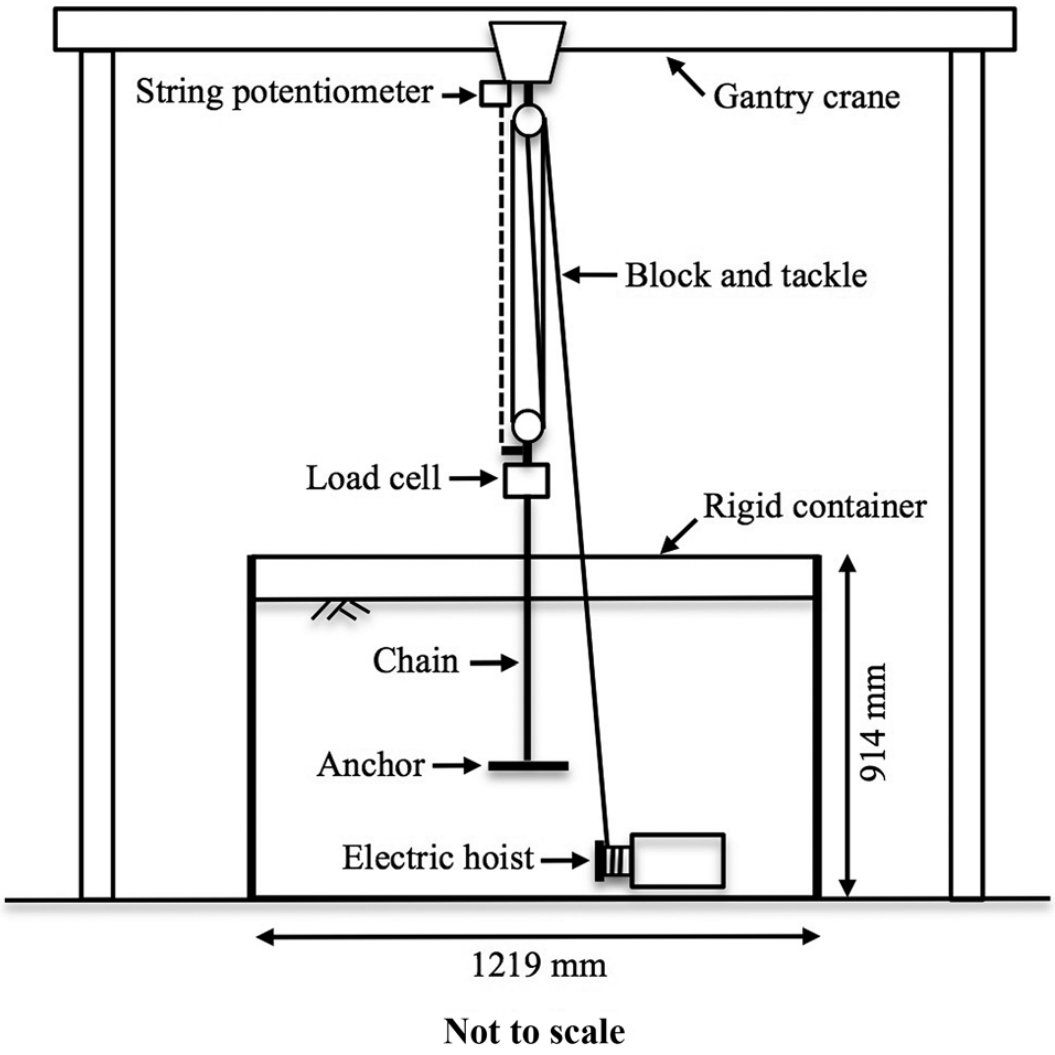

Figure 2.1. Schematic of the anchor test setup used in this study (adapted from Bradshaw et al. 2016).

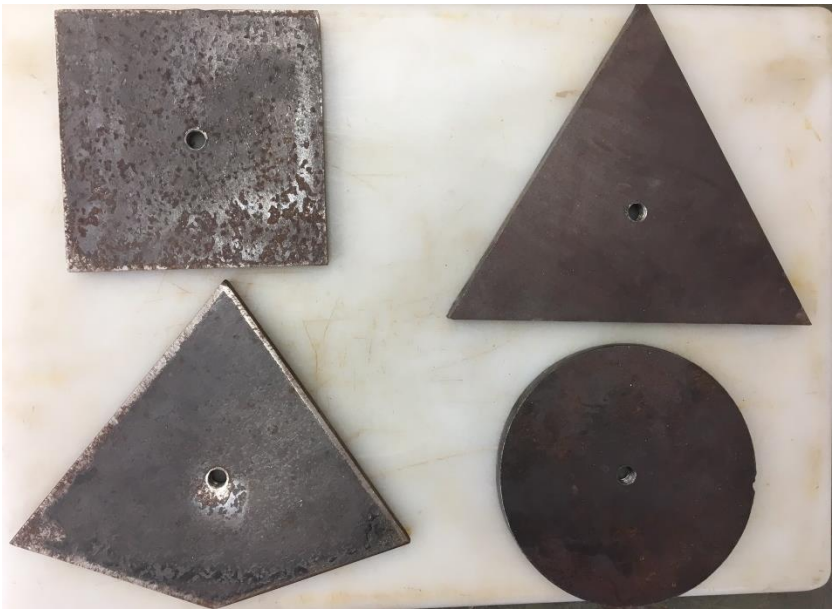

Figure 2.2. Test anchors used in this study with A = 232 cm^2.

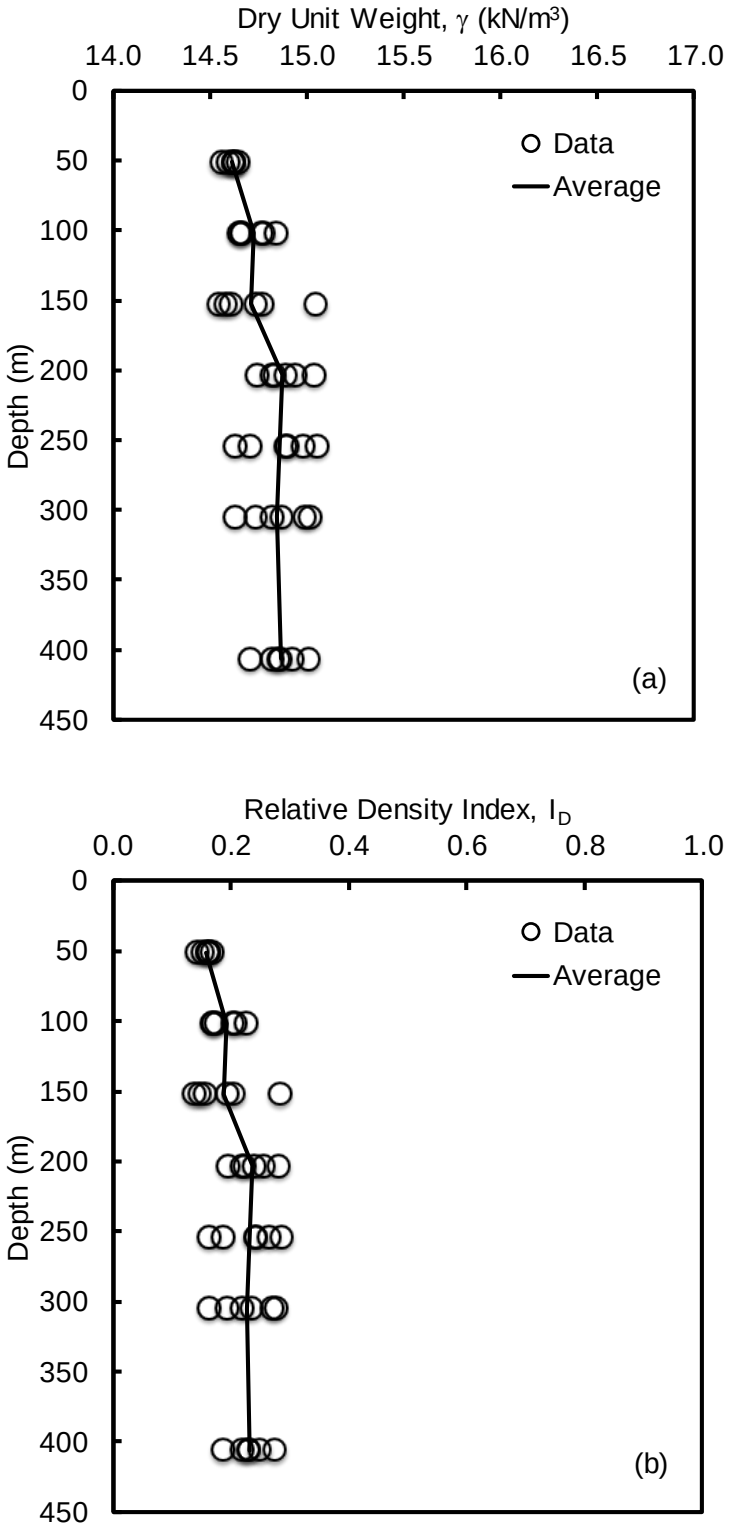

Figure 2.3. Typical profiles of: (a) dry unit weight; and (b) relative density index obtained within the test container.

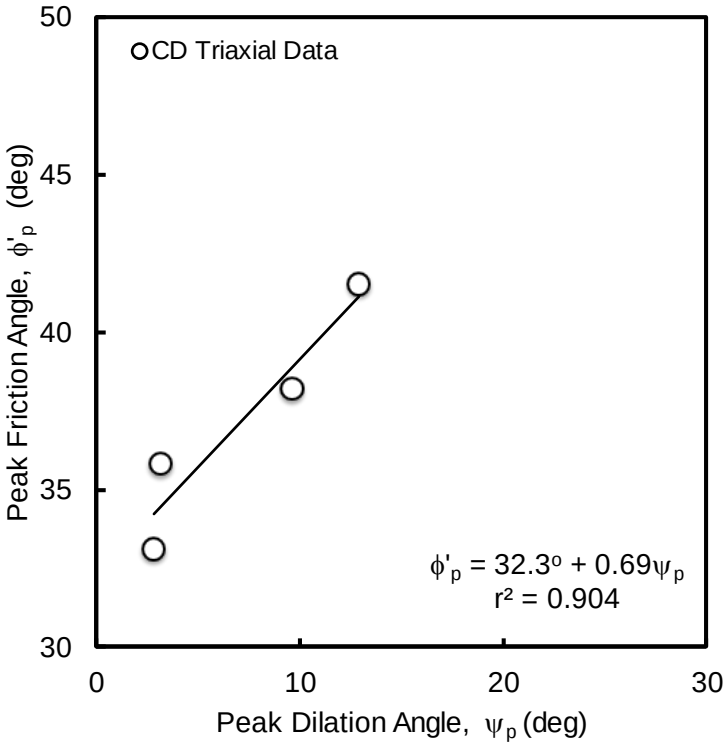

Figure 2.4. Relationship between peak friction and dilation angles for Westerly, RI sand measured in triaxial tests.

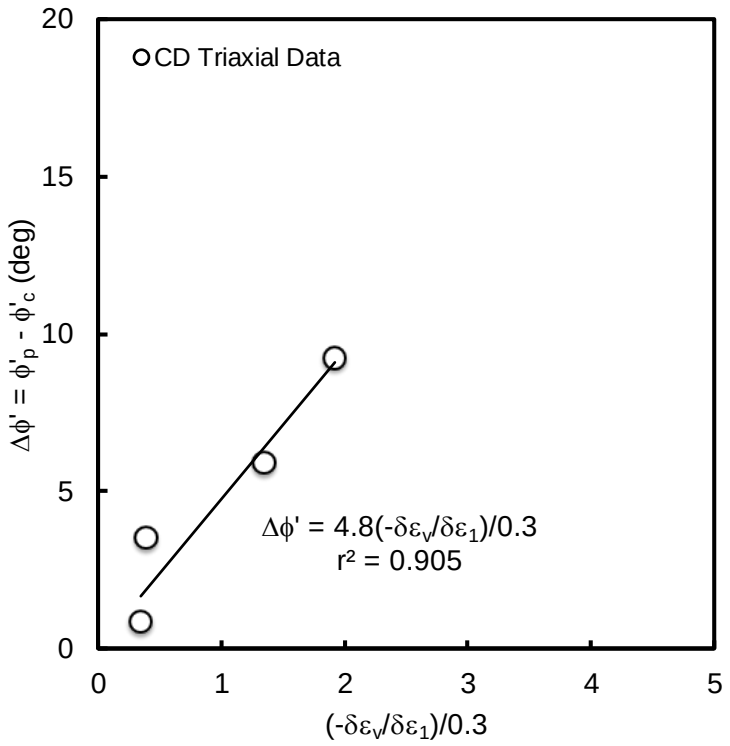

Figure 2.5. Assessment of Bolton (1986) Af parameter from triaxial tests.

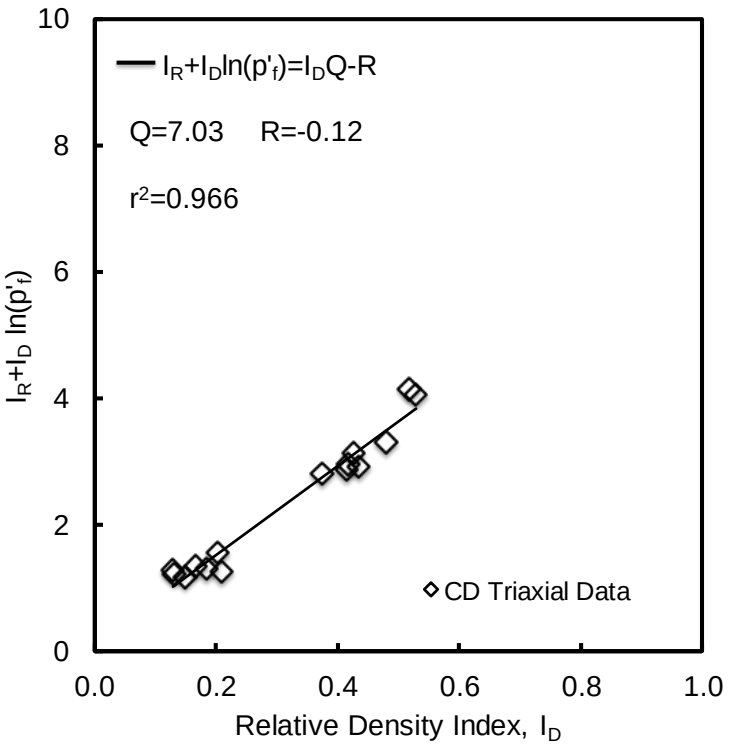

Figure 2.6. Calibration of Bolton (1986) stress-dilatancy Q and R parameters.

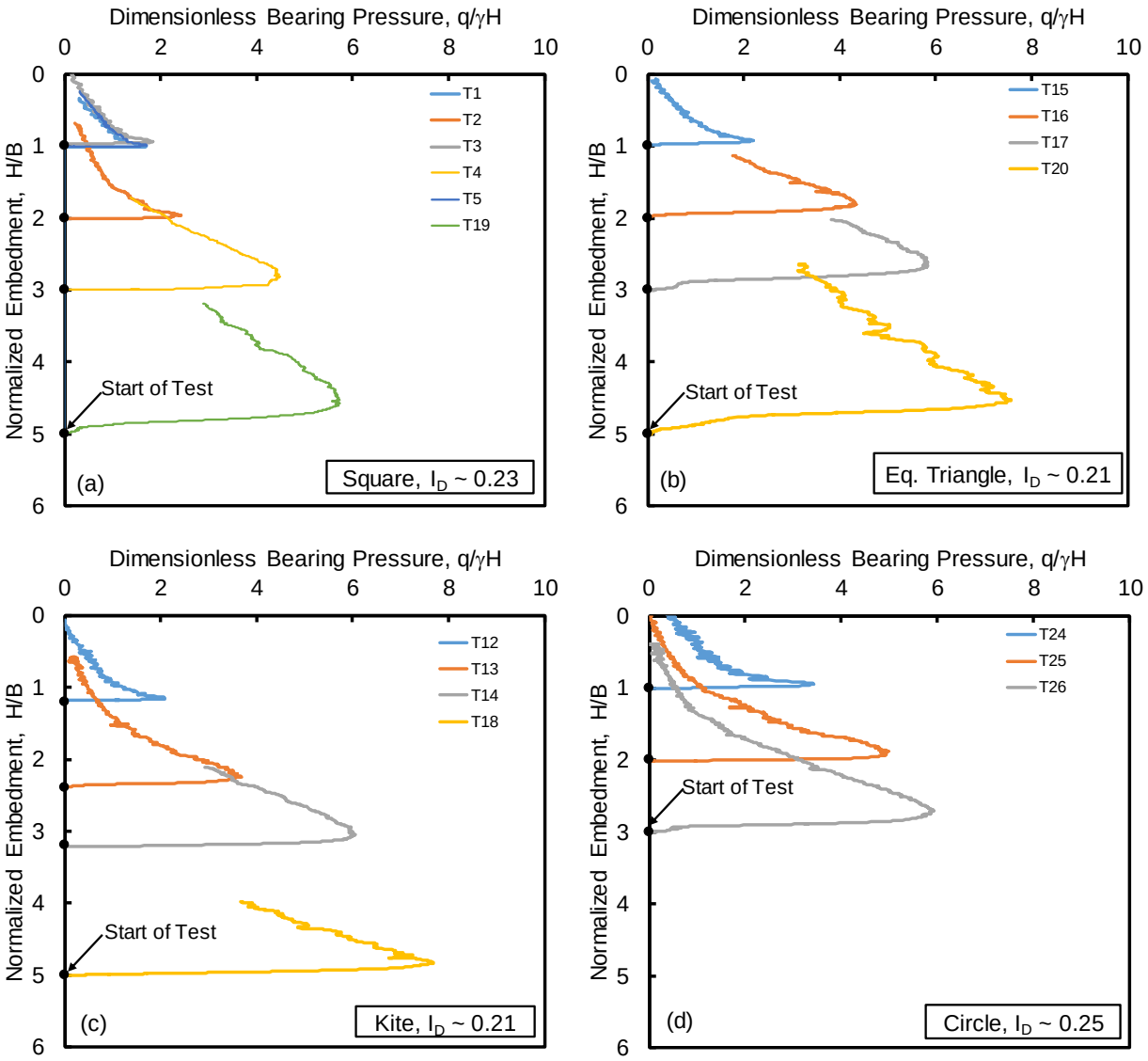

Figure 2.7. Normalized stress-strain behavior for: (a) square anchors; (b) equilateral triangular anchors; (c) kite anchors; and (d) circular anchors.

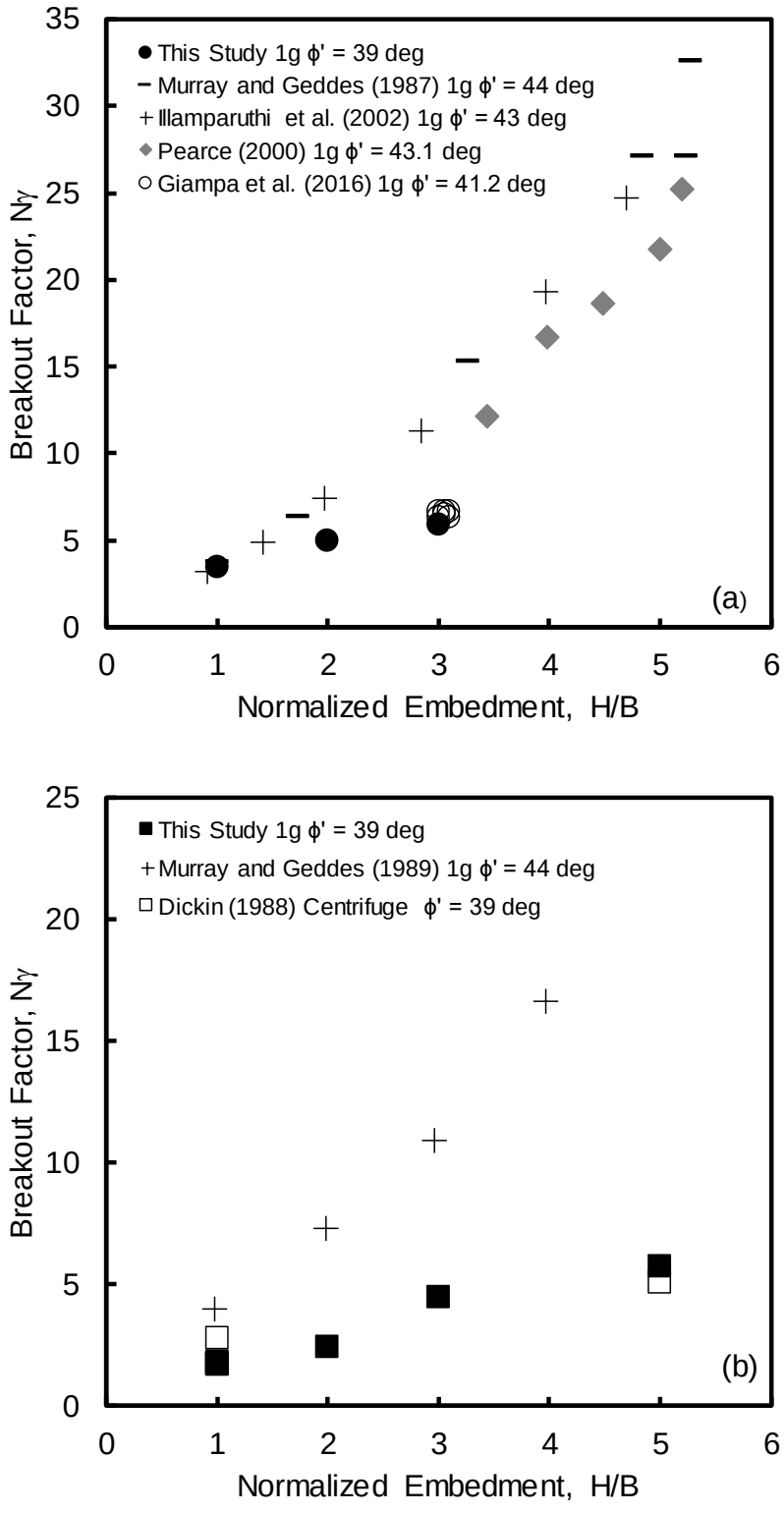

Figure 2.8. Comparison of experimental breakout factors with literature for: (a) circular anchors; and (b) square anchors.

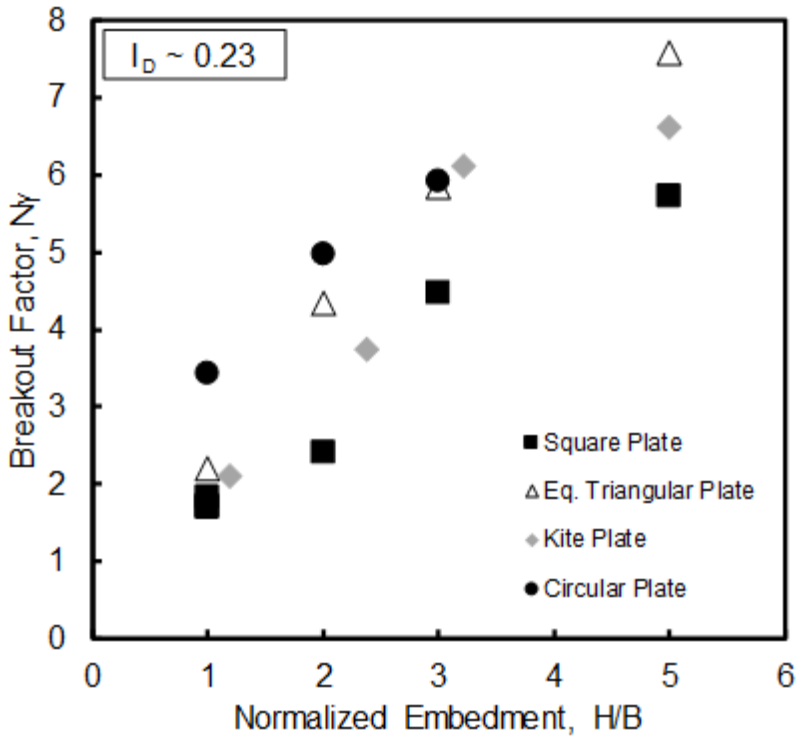

Figure 2.9. Comparison of experimental breakout factor versus normalized embedment.

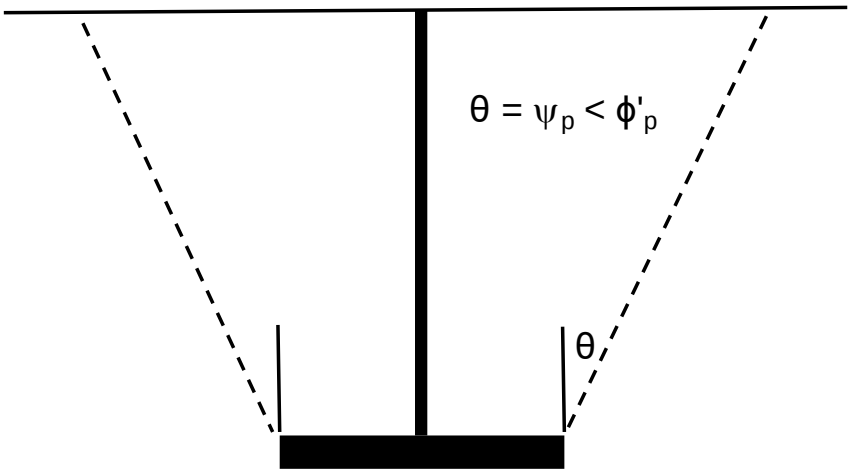

Figure 2.10. Failure mechanism assuming inclination angle corresponds to peak dilation angle.

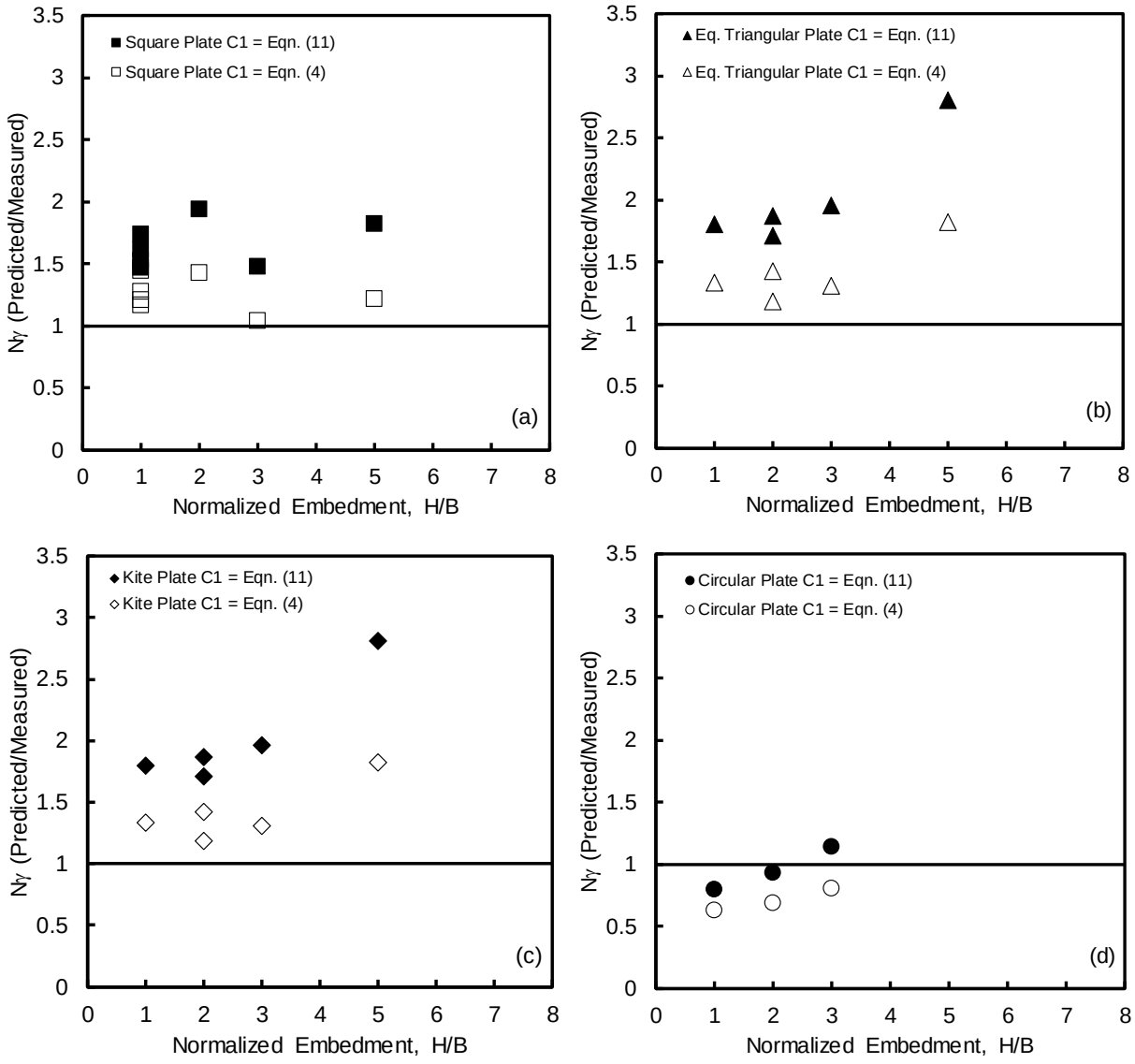

Figure 2.11. Predicted to measured pullout capacity for: (a) square anchors; (b) equilateral triangular anchors; (c) kite anchors; and (d) circular anchors.

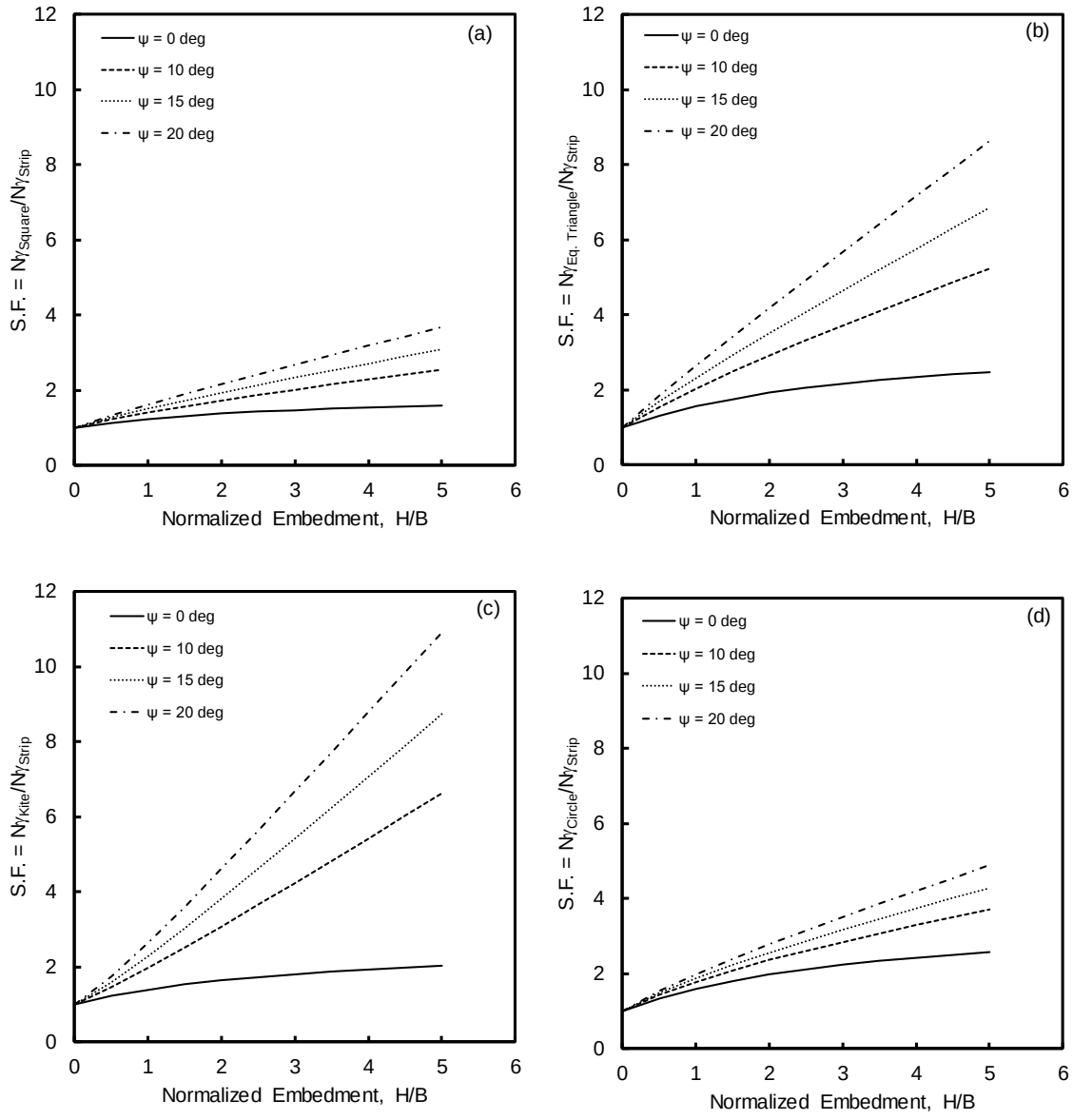

Figure 2.12. Theoretical shape factors with respect to strip anchors for: (a) square anchors; (b) equilateral triangular anchors; (c) kite anchors; and (d) circular anchors.

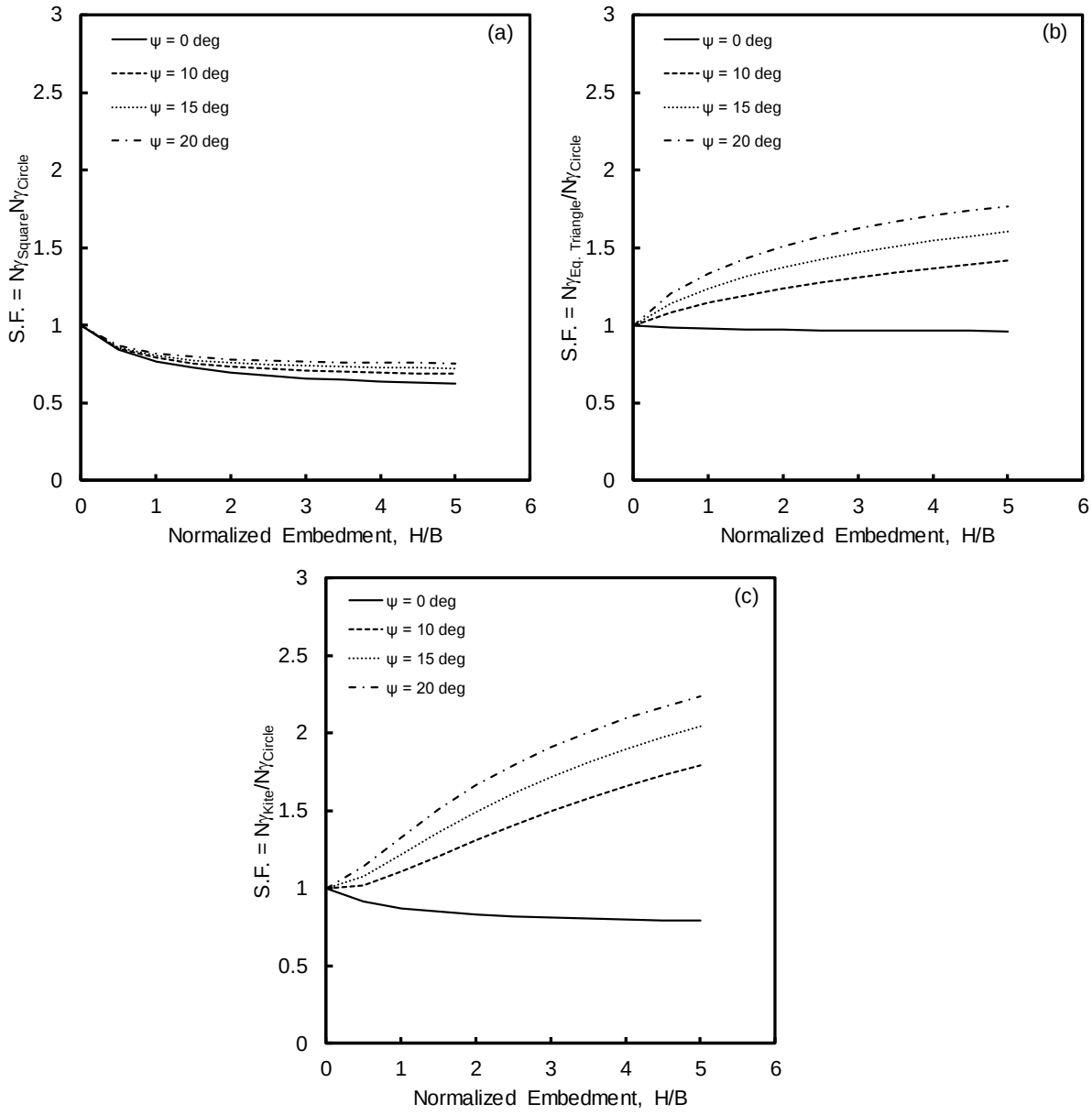

Figure 2.13. Theoretical shape factors with respect to circular anchors for: (a) square anchors; (b) equilateral triangular anchors; and (c) kite anchors.

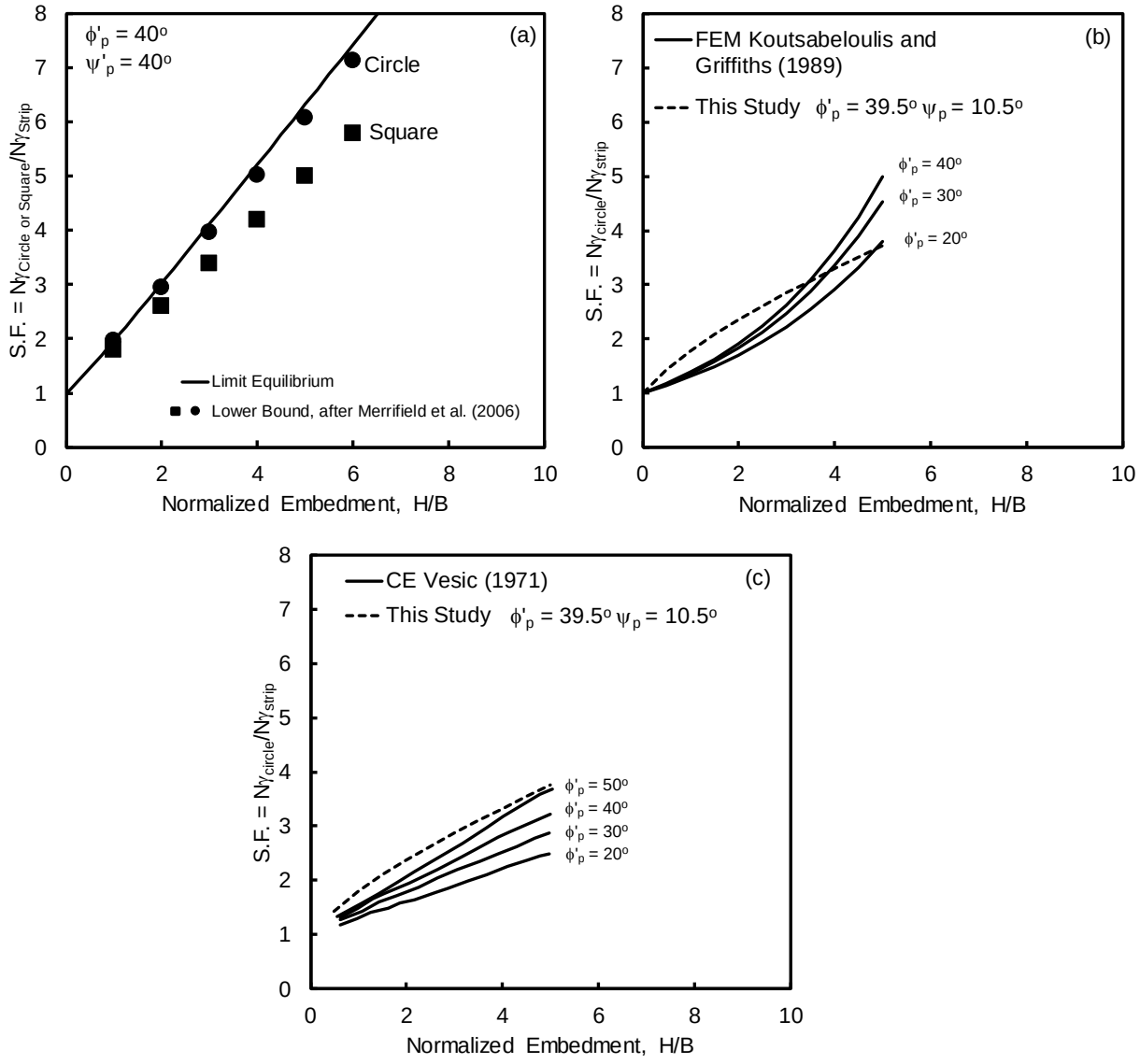

Figure 2.14. Theoretical shape factors comparing strip, circle, and square pullout capacity for shallow embedded anchors in sand using: (a) nonassociated flow limit equilibrium after this study; (b) lower bound limit analysis after Merifield et al. (2006); (c) cavity expansion after Vesic (1971); and (d) FEM after Koutsabeloulis & Griffiths (1989).

3. Experimental Study of the Dive Trajectory Behavior of Fully Embedded Plate Anchors in Sand

Prepared for submission to ASCE Journal of Geotechnical and Geoenvironmental Engineering

-

Abstract

This paper presents an experimental study to investigate the dive trajectory behavior of a fully embedded plate anchor in sand. A series of 1g physical model drag embedment experiments were carried on a simple kite, trapezoid, and double connected trapezoid plate anchor with a free-moving shank mechanism. Experimental results indicate a significant difference in final embedment depth due to drag with respect to geometry. Furthermore, maximum embedment can be achieved when considering the initial embedment depth (i.e. starting point or penetration), fluke orientation, and loading line attachment. The results indicate that the dive performance of a simple kite plate anchor can be optimized when the loading line is attached at or near the anchor centroid at an initial fluke orientation of 10^{o} relative to the horizontal. This configuration has resulted in an additional 1.5 fluke lengths of embedment with no indication of pull out. Although further study is warranted under different soil conditions, anchor geometry, and shank configuration, the results of this study provide valuable insight on the behavior of a fully embedded plate type anchor subject to diving forces, which may further be used for trajectory modeling.

Introduction

Offshore structures are used worldwide for a variety of functions in varying water depth and environmental conditions. Functions include, but are not limited to, oil and gas exploration, production processing, bridges and causeways, loading and offloading facilities, and offshore wind energy production (Offshore Center Danmark [OCD] 2010). In the design and analysis of offshore platforms many factors are taken into account to ensure safety; among the factors are loading conditions generated by the environment (i.e.

wave and wind loads), and transportation and lifting loads. This requires the proper selection and design of the foundation. With increasing interest in offshore technology moving into deeper water there is a greater reliance on anchored floating structures, as opposed to traditional stationary fixed-jacket or gravity-based structures secured to the seafloor through piling (O'Neill et al. 2003).

The Author is currently researching a new anchor concept where a wing-like plate anchor is installed into the seabed using free-fall penetration, similar to a torpedo pile. The anchor will then rotate and move into position that is near normal to the anchor line under the applied mooring load (Gerkus et al. 2016). The shape of the anchor will need to be designed to maintain hydrodynamic stability during free-fall through the water column, and thus will likely take on non-axisymmetric and/or non-planar shapes. To further develop this anchor concept, it is necessary to understand and eventually predict the dive trajectory behavior of the anchor because its capacity in service will depend on its final embedment and orientation.

Much of the literature on anchor trajectory or kinematics has focused on either drag embedment (DEA) or vertically loaded anchors (VLA) which start at the mudline and are dragged into place, or suction embedded plate anchors (SEPLA) that are jetted to a depth and then rotated into position. The behavior of these specific anchors has been investigated in both clay and sand. Theoretical investigations, primarily in clay, have used plastic limit analysis, finite element modeling, and limit equilibrium theories to estimate the dive trajectory and ultimate capacity, initial movement criteria, ultimate embedment depth, and

understanding the failure mechanisms under specific loading conditions (e.g. Murff 1994; Martin 1994; Neubecker and Randolph 1995; Dahlberg 1998; Bransby and O'Neill 1999; O'Neill et al. 2003; Murff et al. 2005; Gilbert et al. 2009; Aubeny and Chi 2010; Liu et al. 2012; Yang et al. 2012; Gaudin et al. 2015; Wu et al. 2016). Other studies have used physical modeling. Focusing on sand, researchers have investigated the dive trajectory and holding capacity of drag embedment anchors simulating a Danforth anchor (LeLievre and Tabatabaee 1981), Navy Standard Stockless anchor with and without stabilizers (Walker and Taylor 1984), Vryhof Stevpris (O'Neill et al. 1999), and Hall type anchors (Shin et al. 2011; Ren et al. 2016), as well as, vertical loaded anchors (e.g. Liu et al. 2010).

The Author is unaware of published studies that have focused on the dive trajectory of an initially embedded drag embedment anchor in sand. Therefore, the objectives of this study are twofold: (1) to identify optimal anchor shapes that have the most effective dive performance, and (2) to investigate the effects of initial embedment depth, loading line location, initial fluke orientation, and loading line angle on the dive trajectory.

Test Sand and Characterization

The sand used in this study primarily consists of a natural deposit of quartz beach sand obtained from Westerly, Rhode Island. The sand has been used extensively in physical 1g model experiments on plate anchors after Bradshaw et al. (2015; 2016) and Gerkus et al. (2016). Characterization of the sand included standard index and consolidated drained triaxial testing. The index properties are summarized in Table 3.1.

The peak friction (ϕ'_p) and dilation angles (ψ_p) were estimated using the Bolton (1986) stress-dilatancy relationship in order to handle the stress dependent changes in the angles at low stresses. The relationship is expressed as

$$\phi'_p - \phi'_c = A_f \left(I_D \left[Q - \ln\left(p'_f\right) \right] - R \right) \tag{3.1}$$

$$\phi'_p - \phi'_c = \beta \psi_p \tag{3.2}$$

Where ϕ'_p = peak friction angle, ϕ'_c = critical state friction angle, ψ_p = peak dilation angle, I_D = relative density index = $(e_{max}-e)/(e_{max}-e_{min})$, e_{max}, e_{min} = maximum and minimum void ratios, respectively, and e = void ratio of the prepared sample, p'_f = the mean effective stress at failure, and Q, R, A_f, and β = Bolton's fitting parameters. Triaxial tests were performed to calibrate Bolton's fitting parameters for the sand used in this study. The triaxial samples were prepared using dry pluviation with a funnel in an attempt to achieve a similar fabric as the sand in the physical 1g model experiments. A range of relative density (D_r) between 13% (I_D = 0.13) and 53% (I_D = 0.53) could be achieved by varying the opening size of the funnel. The critical state friction angle was determined from extrapolating the peak friction angle at zero dilation angle (Bolton 1986), and the fitting parameters (Q, R, A_f, β) were determined from the linear regression plots shown in Figures 3.1-3.3 (Bradshaw et al. 2016). A summary of the fitting parameters can be seen in Table 3.1.

Preliminary Dive Trajectory Study

The objective of the preliminary experiments was to obtain a rough assessment on the effect of anchor shape, loading line attachment point, and initial fluke orientation (θ_f) on the dive performance of a fully embedded drag anchor. The model-anchors consisted of a kite-, trapezoid-, and double connected trapezoid- (i.e. bi-wing) shaped plate shown in Figure 3.4. The models were fabricated from 0.51 cm thick plywood with respective fluke areas (A_{fluke}) of 120 cm^2, 120 cm^2, and 130 cm^2. A very thin steel cable, having a diameter of 1.59 mm, was used during loading to help reduce the soil friction along the loading line. The loading line acts likes a shank that is free to rotate along the long axis of the anchor and connects directly to the simple plate anchors at difference locations along the centerline (Figure 3.4). The 1g model experiments were carried out in a rigid test tank having dimensions of 2.4 m length x 1.2 m width x 0.9 m height.

Various experiments were performed to investigate the trajectory of the different anchor shapes by varying the loading line attachment point (Figure 3.4), initial fluke orientation, and initial embedment (H). These variables are shown on the schematic in Figure 3.5. A measurement rod was attached to the back of the plate anchors to visually observe the change in plate anchor rotation and penetration depth during loading. Each anchor began fully embedded at the beginning of the experiment and the measurement rod extended outside of the soil; sand was not pluviated but rather placed via buckets. A hole was excavated to a desired depth relative to the surface, the anchor was then placed at a predetermined fluke orientation, and then backfilled prior to testing. The loading rate was approximately 50 mm/s controlled by an electric hoist, and a block and tackle system.

Although the rate was significantly higher than other studies (e.g. Liu et al. 2010), strain rates have been shown to have a negligible effect on the strength of dry sand (e.g. Whitman and Healy 1962). After the anchors were placed at their initial locations and orientations, they were pulled horizontally, a distance of approximately 5 fluke lengths (L_f).

Figure 3.6 displays the results of the preliminary dive trajectory experiments. The results of each model anchor are presented in terms of final normalized embedment as a function of initial fluke orientation relative to the horizontal, loading line attachment location, and initial embedment. Trends among the three anchor models indicate that the movement, change in orientation, and embedment depth are highly dependent on the loading line attachment location on the fluke. When the loading line was attached at or below the anchor centroid, rotation was induced and the anchor moved away from the vertical, suggesting the attachment point was initially below the anchor center of pressure (COP). Alternatively, with the attachment located above the centroid and COP, all three anchor shapes rotated toward the vertical and pulled out of the soil. For the kite and trapezoid anchor, an increase in embedment was observed, while the anchor rotated away from the vertical (Figure 3.6a/b). The embedment of the bi-wing anchor increased at early stages of drag, but then decreased as the anchor rotated below the horizontal causing the anchor nose to pitch upward, the loading line to act purely parallel with the fluke, and pull the anchor toward the soil surface resulting in an embedment shallower than the starting point (Figure 3.6c). The large amount of rotation seen by the bi-wing is an indication that the loading line is attached significantly below the COP, such that a large moment is produced causing the anchor to rotate more rapidly to the horizontal and eventually pull out.

The dive performance of the plate anchor models is further influenced by the initial fluke orientation (Figure 3.6a/b). With the exception of the bi-wing anchor, the final embedment depth was greatest when the anchor was initially oriented between 45^o and 60^o. The anchors dove while rotating away from the vertical during loading and eventually ceased when becoming parallel with the horizontal. The results suggest that by beginning the anchor at a steeper initial fluke orientation the final embedment can be maximized because more time is required to rotate the anchor to the horizontal over the same distance. Based on a series of experiments using the kite anchor (Figure 3.6a), initial embedment depth showed to have a minimal influence on the dive performance. The kite anchor was started at an initial embedment of $1L_f$ and $2L_f$ below the soil surface. On average, an additional 0.5 fluke lengths of embedment was achieved at either embedment depth.

Main conclusions from the preliminary dive trajectory experiments are as follows:

- The kite plate anchor resulted in the greatest maximum embedment depth compared to the trapezoid and bi-wing shapes. The kite anchor gained 60% more embedment when starting at an initial fluke orientation (θ_f) of 45^o.
- When the loading line was attached above the plate anchor centroid, the fluke moved toward the vertical position and pulled out of the soil with increasing horizontal displacement. This behavior was exhibited by the bi-wing anchor regardless of line location.
- For the kite and trapezoid shapes, diving was caused when the loading line was attached at the anchor centroid and/or slightly below the anchor center of pressure.

- The anchor dive trajectory changed significantly for different anchor shapes in dry sand, contrary to what was found for experiments performed in clay using similar plate anchor shapes after Gerkus (2016).
- Maximum embedment was achieved by the kite shape anchor when the loading line was attached at the anchor centroid or slightly below the anchor COP starting at an initial embedment depth of $1L_f$.

Detailed Dive Trajectory Study of the Kite Anchor

Building on the preliminary dive trajectory study, a series of experiments were performed on just the kite anchor, which included the measurement of all six-degrees of motion and loading line tension during embedment.

Scaling Considerations

It is important to consider scale effects so that the results can be reliably interpreted. Bradshaw et al. (2016) showed that scale effects can be minimized in 1g plate anchor tests by presenting capacity in a dimensionless form, $q/\gamma H$, where q is the plate bearing pressure, γ is the dry unit weight of the sand, and H is the embedment depth from the soil surface to deepest part of the anchor. and by scaling the constitutive behavior of the soil. Soils will generally have a higher strength in small-scale 1g models due to higher dilation at low confining pressures. Therefore, the scaling of the constitutive behavior involves preparing the soil looser in the model than at full-scale to get a similar dilation response. Consistent with current centrifuge scaling laws presented in Garnier and Gaudin (2007), experiments were also designed such that the width of the anchors were at least 48 times the median

diameter (D_{50}) of the sand to ensure there was a sufficient number of particles over the width of the plate.

Sample Preparation

The sand was rained into the test tank using a portable pluviator based on Gade et al. (2013). The pluviation device consisted of a bucket attached to a flexible hose leading to a pipe containing a plate with holes and a stack of sieves. The unit weight of the soil was determined by pluivating sand into small cups of a known volume (413 cm^3) that were placed on the soil surface at various depths during sand placement. An example of the dry unit weights measured during preparation in the test container is shown in Figure 3.7a along with corresponding calculated relative density index in Figure 3.7b. The relative density indices were fairly consistent throughout the container with a coefficient of variation of less than 0.2. This was equivalent to 35% to 40% (I_D = 0.35 to 0.40) at full-scale to account for scale effects (Bradshaw et al. 2016). Additionally, the corresponding peak friction and dilation angles in each test container, on average, were 39^o and 10^o, respectively.

The plate anchors were placed at a desired depth and fluke orientation during pluviation. Upon completion of the test sample, the anchors were fully embedded (Figure 3.5). The kite anchor was placed at normalized embedment's (H/L_f) of 1 and 2, with fluke orientations of 10^o, 20^o, 30^o, and 45^o. Lastly, the loading line location was placed at the approximate anchor centroid in order to minimize the amount of rotation at the start of drag and potentially maximize embedment. During the drag experiments a six-degree-of-freedom magnetic tracker (magnetometer by Polhemus) was used to measure position (i.e.

x-y-z) and orientation (i.e. yaw [azimuth], pitch [elevation], roll) of the anchor as it moves through the soil in real time. Additional sensors included a 2.2 kN (CAS SBA) load cell and string potentiometer (Measurement Specialties SP2-50). The magnetometer was recessed on the back of the plate anchor before testing, while the load cell and string potentiometer were connected to the far end of the loading line beyond the pulley shown in Figure 3.8.

Tracking Position and Orientation

Anchor position and orientation was measured using a Polhemus magnetic tracking device as shown in Figure 3.9. The system consists of a sensor, source, electronics unit, and software package (Patriot User Manual 2008). The source receives the electromagnetic waves produced from the sensor during testing and is then converted to rotation and displacement measurements via a calibration that is performed by the manufacturer. The system generates its own magnetic field when in operation, and if highly magnetic objects are in close proximity to either the source and/or sensor, the internal calibration will be temporarily altered. This interference becomes noticeable in the system's live display and can be fixed by moving magnetic objects out of range and by locating the source within 127 mm of the sensor.

Translation readings from the magnetometer are measured with respect to the center of the source; the positive x and y directions are marked on the sensor and the right hand rule is used to determine the positive z direction. The rotational angles are presented as Euler angles and are expressed in terms of rotating frames. The yaw (azimuth) is rotation around

the z-axis, pitch (elevation) is rotation around the y-axis, and roll is rotation around the x-axis. The sensor first measures the yaw angle with respect to the external frame of x-y-z, next a new coordinate system is set (x'-y'-z') and the pitch rotation is measure with respect to this new frame, and finally, another coordinate system is set (x"-y"-z") to measure the roll rotation. The amount of rotation the anchor undergoes in each direction during loading is important for anchor dive trajectory tests, but using Euler angles may be misleading when extracting the exact behavior. Consequently, to measure the change in each rotation at a given interval or frame, the rotational angles should be measured with respect to a fixed axis of x-y-z rather than rotating axes, thus requiring a correction to be made to the magnetometer output (Gerkus 2016). This correction to the rotational output can be made by using a direction cosine matrix (R) that can be expressed for this magnetometer as

$$R = \begin{bmatrix} \cos\psi\cos\theta & \cos\psi\sin\theta\sin\varphi - \sin\psi\cos\varphi & \cos\psi\sin\theta\cos\varphi + \sin\psi\sin\varphi \\ \sin\psi\cos\theta & \sin\psi\sin\theta\sin\varphi & \sin\psi\sin\theta\cos\varphi - \cos\psi\sin\varphi \\ -\sin\theta & \cos\theta\sin\varphi & \cos\theta\cos\varphi \end{bmatrix} \quad (3.3)$$

Where ψ = yaw; θ = pitch; and φ = roll. The direction cosine matrix is calculated for each measurement frame and then multiplied by the inverse of the matrix (R^{-1}) of each measurement frame. Next, the sum of the change in angles calculated with respect to this "new" frame gives the change in yaw, pitch, and roll angles with respect to a fixed axis. The rotation results presented in this study show the real time anchor movement in each direction calculated using this method. It is noted that for all drag tests the anchor exhibited minimal roll and yaw rotation movements shown in Figure 3.10.

Effects of Initial Embedment Depth

Knowledge of the initial embedment depth of the wing-anchor concept is particularly important in order to understand its trajectory and drag efficiency following free-fall penetration. To investigate the effect of initial embedment depth, the anchor was started at 1 and 2 fluke lengths below the soil surface at initial fluke orientations of 10^o and 30^o from the horizontal.

Figure 3.11 shows the dive trajectory normalized by fluke length, along with the corresponding fluke orientation and loading line tension applied at the surface during drag. It is evident that for a given fluke orientation, the anchor will achieve more relative embedment when beginning at $1L_f$ below the soil surface. During drag, the anchor gradually rotates from the horizontal to the vertical (Figure 3.11b), with this behavior occurring much faster when the anchor begins at an initial embedment of $2L_f$. As the anchor pitches closer to the vertical the tension in the loading line increases, indicating the anchor is being loaded near normal to the fluke area (Figure 3.11c). Upon reaching a peak load there is a sudden decrease due to the reduction in soil overburden as the anchor moves upward through the soil. A rapid increase in the tension force can be seen in tests T8 and T9 due to the anchor rotating to the vertical at an early stage of drag. A similar trend can be seen in tests T3 and T4, however, the increase occurs around $1L_f$ of drag. The cause of the decrease in embedment at $2L_f$ and $2.5L_f$ may be linked to the free movement of the loading line, attachment point, and limitations of the box length potentially causing the loading to act more normal to the fluke as it is drag. As the anchor dives deeper and rotates closer to the vertical, the line will have a tendency to act more normal to the fluke, rather

than parallel to the fluke, and cause pull out. Additionally, as the anchor becomes steeper the center of pressure moves closer to the anchor nose and below the original loading line attachment, causing the loading line to now act above the center of pressure and uplift the anchor.

The location of the loading line between the anchor centroid and center of pressure is particularly difficult to achieve using small-scale models. A slight offset may cause the line to act above the center of pressure and cause the anchor to rotate toward the vertical at early stages of drag shown in Figure 3.11b.

Effect of Initial Fluke Orientation

To investigate the effect of initial fluke orientation on the dive trajectory, the model was placed $1L_f$ below the soil surface with its fluke orientation ranging from 10^o to 45^o from the horizontal. Figure 3.12 shows the normalized trajectory, fluke orientation, and loading line tension applied at the surface during drag. The results indicate optimum diving and maximum embedment depth is achieved when the anchor is near parallel ($\theta_f = 10^o$) with the horizontal. Test T4 achieved approximately $0.5L_f$ more embedment, with no indication of pull out, compared to the remaining tests (Figure 3.12a). Also, the test results show that the anchor continues to pitch to the vertical while diving deeper due the change in center of pressure with depth and orientation. For tests T2, T3, T5R, and T7 the diving occurred when the anchor rotated between 25^o and 35^o from the horizontal. However, slight plowing followed by pull out occurred when the fluke orientation exceeded 40^o (Figure 3.12b).

Rotation of the fluke toward the vertical is observed for all of the tests shown in Figure 3.12b. By placing the anchor at an initial shallow orientation relative to the horizontal, more time is required to rotate the anchor to the vertical, and allowing the anchor to dive deeper over the same distance. This finding indicates that optimum dive can be achieved when the anchor is started at a shallow fluke orientation around 10^o with a loading line attachment at the approximate anchor centroid.

Effect of Loading Line Attachment

To obtain minimal pitch or fluke rotation during drag it is important to locate the loading line or shank attachment at the anchor centroid or below the center of pressure. The preliminary tests performed showed that if the loading line is attached at or below the anchor centroid, the eccentricity will cause a moment resulting in fluke rotation away from the vertical. This further indicates that the center of pressure is close to the anchor centroid. Conversely, for line attachments above the anchor centroid or center of pressure, a moment is caused rotating the anchor toward the vertical, and eventually out of the soil. To investigate the effects of the loading line attachment a comparison of two drag tests, T3 and T6, under the same conditions were made. The loading line attachment point was located at the approximate anchor centroid in T3 and moved $0.13L_f$ below in T6, closer to the anchor nose.

The results are summarized in Figure 3.13. The dive trajectory (Figure 3.13a) differed significantly between the two drag experiments, showing more relative embedment when the location of the loading line was at the approximate anchor centroid. As can be seen in

Figure 3.13b, when the loading line was attached 0.13Lf below the centroid a large moment was induced causing the anchor to rotate at a faster rate to the horizontal. Diving was ceased at approximately 2 fluke lengths of drag due to the anchor becoming parallel with the horizontal. The behavior is further displayed in terms of the applied loading line tension at the soil surface shown in Figure 3.13c, where the loading line tension essentially plateaus indicating the anchor is plowing at a constant depth. As dragging continues, test T6 began to pitch below the horizontal and pull out of the soil, causing a slight reduction in line tension. Alternatively, diving was exhibited in test T3 until reaching a fluke orientation greater than 40^{o}. This behavior was further observed in tests shown in Figure 3.11 and 3.12.

Relationship Between the Fluke Orientation and Loading Line Angle

To further study the behavior of the dive trajectory of this simple wing-anchor concept it is important to understand the relationship between the fluke orientation and loading line angle at the attachment (θ_a) relative to the horizontal (Figure 3.5). Having knowledge of the attachment angle determines the relative horizontal and vertical force components on the anchor caused by a structure. This information is a critical aspect in the design of this anchor and other drag embedment type anchors, as it will determine the mode of failure and the optimum location of the loading line on the anchor, and the embedment performance (Neubecker and Randolph 1995).

For an embedded section of loading line shown in Figure 3.14, the governing differential equations proposed by Vivatrat et al. (1982) and further presented in Neubecker and Randolph (1995) are expressed as

$$\frac{dT}{ds} = F + w\sin\theta \tag{3.4}$$

$$T\frac{d\theta}{ds} = -Q + w\cos\theta \tag{3.5}$$

Where T = tension in the chain; ds = length of loading line segment; q = angle relative to the horizontal subtended by the loading line; F = resistance per unit length offered by the soil tangential to the loading line; Q = resistance per unit length offered by the soil normal to the loading line; and w = buoyant weight of the chain per unit length. The bearing resistance, Q, of the loading line was estimated after Mortensen (2015) shown as

$$Q = dA_{sand}\left(0.5\gamma dA_{sand}N_{\gamma s} + N_q\sigma'_v\right) \tag{3.6}$$

Where d = diameter of the loading line; A_{sand} = 1 for a wire or cable = empirical factor linking chain thickness to the representative width of a chain link; $N_{\gamma s}$ = bearing capacity factor after Lundgren and Mortensen (1953); N_q = bearing capacity factor for the surcharge-case after Prandtl (1920); and σ'_v = average in situ vertical effective stress. The loading line angle at the attachment location was then determined throughout each drag test by numerically solving the chain equilibrium equations with the loading line bearing

pressure, Q, increasing nonlinearly with depth, and assuming the line angle at the soil surface is equal to zero.

The results of the dive trajectory tests showing the relationship between fluke orientation and loading line angle at the attachment are shown in Figure 3.15. Anchor tests beginning at 1 fluke length of embedment with the loading line attached near the anchor centroid are used. With all tests, except T4, the anchor followed a similar trajectory where the anchor rotated continuously during drag while diving deeper. Between $0L_f$ and $1L_f$ of horizontal displacement, a large line angle was estimated suggesting minimal anchor movement. With increasing horizontal displacement, the line cut through the sand, decreasing to approximately 20^o where it was maintained for the duration of drag. Similar behavior was observed in test T4, however the line angle at the attachment was maintained around 30^o relative to the horizontal. Although diving was observed for all tests shown in Figure 3.15, it was maximized in T4. This finding suggests that the loading line angle at the attachment should be maintained around 30^o for optimal dive performance, which is comparable the line angle used for VLAs in sand after Liu et al. (2010).

Conclusions

The objective of this study was to investigate the dive trajectory behavior of a fully embedded plate anchor in sand. Specifically, (1) to identify the optimal anchor shapes that have the most effective dive performance, and (2) to investigate the effects of initial embedment depth, loading line location, initial fluke orientation, and loading line angle on the dive trajectory. A series of 1g physical model experiments were performed on a kite,

trapezoid, and double connected trapezoid (i.e. bi-wing) shaped plate anchor with a loading line free to move along the long axis of the fluke. These experiments were designed to gather a preliminary understanding of the anchor movement, change in orientation, and final embedment depth with respect to shape, initial orientation, and loading line attachment. The preliminary results indicated that the dive trajectory in dry sand is specific to anchor geometry, loading line attachment, and initial embedment depth. The kite plate anchor achieved approximately 60% more final embedment than the trapezoid and bi-wing anchors. The maximum final embedment of the kite anchor was achieved at an initial embedment depth of $1L_f$ with the loading line attached at the anchor centroid.

Building off of the preliminary dive trajectory study, a series of controlled drag tests were carried out on the kite plate anchor to investigate the effect initial embedment depth, initial fluke orientation, and loading line attachment point has on the trajectory behavior, as well as, the relationship between the fluke orientation and loading line angle during drag. The primary conclusions indicate the following:

- The simple plate anchor configurations showed significant diving in sand, indicating a free-moving shank along the long axis of the fluke (i.e. loading line) is sufficient for penetration.
- For a free-moving loading line, the location is critical in order to maximize embedment during drag.
- The dive performance of a kite shaped anchor is optimized by locating the loading line at the approximate anchor centroid and by placing the anchor at an initial fluke orientation 10^o. Model tests with initial embedment of $1L_f$ show that the anchor will

achieve an additional $1.5L_f$ of embedment with no indication of pull out. However, for the same fluke orientation at $2L_f$ of initial embedment the anchor will only dive an additional $0.5L_f$ before pulling out of the soil.

- Optimum diving was further achieved when the loading line angle at the attachment was between 25^o and 30^o relative to the horizontal.

Although further investigation is warranted under saturated conditions, additional anchor geometry, and shank mechanism, the results of the current experimental study provide valuable insight on the dive trajectory behavior of a fully embedded plate anchor in sand and aid in future trajectory modeling.

Acknowledgments

This material is based upon work supported by the National Science Foundation under Grant No. 1300142 and also by the Science Foundation Ireland under the U.S.-Ireland R&D Partnership Program Grant No. SFI/2012/US/E2479. The Author would also like to thank Kevin Broccolo at the University of Rhode Island for all of his fabrication efforts put forth to conduct this research.

References

Aubeny, C.P. and Chi, C. (2010). "Mechanics of drag embedment anchors in a soft seabed." *J. Geotech. and Geoenviron. Engrg.*, 136(1), 57-68.

Bradshaw, A.S., Giampa, J., Dietrich, F., Gilbert, R.B., and Gerkus, H. (2015). "Pullout Capacity of Plate Anchors in Sand for Floating Offshore Wind Turbines." *Proc., of the 3rd Inter. Symp. on Frontiers in Offshore Geotechnics*, Oslo, Norway: NGI. 833-838.

Bradshaw, A.S., Giampa, J.R., Gerkus, H., Jalilvand, S., Fanning, J., Nanda, S., Gilbert, R., Gavin, K., and Sivakumar, V. (2016). "Scaling Considerations for 1-g Model Horizontal Plate Anchor Tests in Sand." *Geotech. Testing J.*, 39 (6), 1-9.

Bransby, M.F. and O'Neill, M. (1999). "Drag anchor fluke soil interaction in clays." *Proc. Int. Symp. on Numerical Models in Geomechanics*, Rotherdam, Netherlands: Balkema. 489-494.

Bolton, M. (1986). "The strength and dilatancy of sands." *Geotechnique*, 36(1), 65–78.

Dahlberg, R. (1998). "Design procedures for deepwater anchors in clay." *Offshore Tech. Conf.,* Houston, TX.

Gade, V.K., Dave, T.N., Chauhan, V.B., and Daska, S.M., 2013, "Portable traveling pluviator to reconstitute specimens of cohesionless soils," *Proc. of Indian Geotech. Conf.*, University in Roorkee, India.

Garnier, J., Gaudin, C., Springman, S.M., Culligan, P.J., Goodings, D., Konig, D., Kutter, B., Phillips, R., Randolph, M. F., and Thorel, L. (2007). "Catalogue of scaling laws and similitude questions in geotechnical centrifuge modeling." *Int. J. Phys. Modell. Geotech.*, 7(3), 1-23.

Gaudin, C., Tian, Y., Cassidy, M., Randolph, M., Wang, D., and O'loughlin, C. (2015). "Design and performance of suction embedded plate anchors." *Proc. Offshore Frontiers in Geotech. III*, 1, London, U.K., 863-868.

Gerkus, H. (2016). "Model experiments to measure yield thresholds and trajectories for plate anchors and develop a new anchor concept". University of Texas at Austin, Austin TX.

Gerkus, H., Giampa, J.R., Senanayake, A.I., Lai, Y., Huang, Y., Flores, J. E.I., Breithaupt, N.B., Sivarajah, S., Bradshaw, A. S., and Gilbert, R.B. (2016). "Preliminary development of a new concept to improve sustainability of offshore foundations." *Proc. Geo-Congress Conference*, ASCE, IL.

Gilbert, R.B., Lupulescu, C., Lee, C.H., Miller, J., Kroncke, M., Yang, M., Aubeny, C., Murff, J.D. (2009). "Analytical and experimental modeling for out-of-plane loading of plate anchors." *Offshore Tech. Conf.*, Houston, TX.

Giampa, J.R., Bradshaw, A.S., and Schneider, J.A. (2016). "Influence of Dilation Angle on Drained Shallow Circular Anchor Uplift Capacity," Int. J. Geomech., 17(2).

LeLievre, B. and Tabatabaee (1981). "The performance of marine anchors with planar flukes in sand." *Can. Geotech. J.*, 18, 520-534.

Liu, H., Zhang, W., Zhang, X, and Liu, C. (2010). "Experimental investigation on the penetration mechanism and kinematic behavior of drag anchors." *Applied Ocean Research*, 32, 434-442.

Liu, H., Liu, C., Yang, H., Li, Y., Zhang, W., and Xiao, Z. (2012). "A novel kinematic model for drag anchors in seabed soils." *Ocean Engrg.*, 49, 33-42.

Martin, C.M. (1994). "Physical and numerical modelling offshore foundations under combined loads." Ph.D. Dissertation. University of Oxford.

Mortensen, N. (2015). "Chain configuration in sand, theory and large scale field testing." *Proc., of the 3rd Inter. Symp. on Frontiers in Offshore Geotechnics*, Oslo, Norway: NGI. 905-912.

Murff, J.D. (1994). "Limit analysis of multi-footing foundation systems." *Proc., 8th Int. Conf. on Computer Methods and Advances in Geomech.*, Abington, U.K.: Vol. 1, Taylor & Francis. 233-244.

Murff, J.D., Randolph, M.F., Elkhatib, S., Kolk, H.J., Ruinen, R., Strom, P.J., and Thorne, C. (2005). "Vertically loaded plate anchors for deepwater applications." *Proc. Int. Symp. on Frontiers in Offshore Geotech.*, Perth, Australia: Balkema. 31-48.

Neubecker, S.R. and Randolph, M.F. (1995). "Performance of embedded anchor chains and consequences for anchor design." *Offshore Tech. Conf.*, Houston, TX. 191-200.

Offshore Center Danmark (2010). *Offshore Book: An introduction to the offshore industry*.Morten Holmager.

O'Neill, M. P., Bransby, M. F., and Randolph, M.F. (2003). "Drag anchor fluke-soil interaction in clays." *Can. Geotech. J.*, 40, 78-94.

O'Neill, M.P., Randolph, M.F., and House, A.R. (1999). "The behaviour of drag anchors in layered soils." *Int. J. of Offshore and Polar Engrg.*, 9(1), 73-78.

Patriot User Manual. (2008, February). Polhemus

Prandtl, L. (1920). "Uber die Harte plastischer Korper." *Nachr. D. Ges. D. Wiss., math-phys.* KI. Gottingen.

Ren, Y., Lei, Z., Sun, L., and Yan, S. (2016). "Model tests of dragging hall anchors in sand." *J. Marine Science and Tech.*, 24(1), 26-31.

Shin, H., Seo, B., and Lee, J. (2011). "Experimental study of embedding motion and holding power of drag embedment type anchor on hard and soft seafloor." *Int. J. Archit. Ocean Engrg.*, 3, 193-200.

Vivatrat, V., Valent, P.J., and Ponterio, A.A. (1982). "The influence of chain friction on anchor pile design." *Proc. 14th Annu. Offshore Tech. Conf.*, Offshore Technology Conference, Houston, TX, 153-163.

Walker, G.R. and Taylor, R.J. (1984). “Model anchor tests in cohensionless soil.” *J. Waterway, Port, Coastal, and Ocean Engrg.*, 110(4), 463-471.

Whitman, R. V. and Healy, K. A., 1962, “Shear strength of sands during rapid loadings,” *J. Soil Mech. Found. Div.*, 88(SM2), 99–131.

Wu, X., Chow, Y.K., and Leung, C.F. (2016). “Prediction of drag anchor trajectory with both shallow and deep anchor behavior.” *Offshore Tech. Conf. Asia*, Kuala Lumpur, Malaysia.

Yang, M., Aubeny, C.P., and Murff, J.D. (2012). “Behavior of suction embedded plate anchors during keying process.” *J. Geotech. and Geoenviron. Engrg.*, 138(2), 174-183.

Table 3.1. Properties of test sand.

Property	Value
γ_{max} (kN/m^3)	18.1
γ_{min} (kN/m^3)	14.1
e_{min}	0.44
e_{max}	0.84
D_{50} (mm)	0.30
G_s	2.65
ϕ'_c (deg)	32.3
Q	7.03
R	-0.12
A_f	4.75
β	0.69

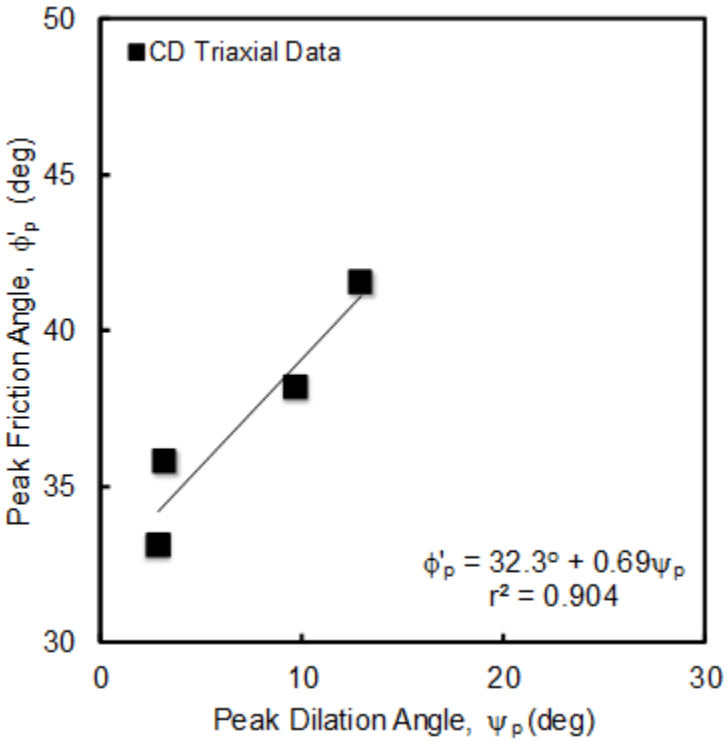

Figure 3.1. Relationship between peak friction and dilation angles for Westerly, RI sand measured in triaxial tests.

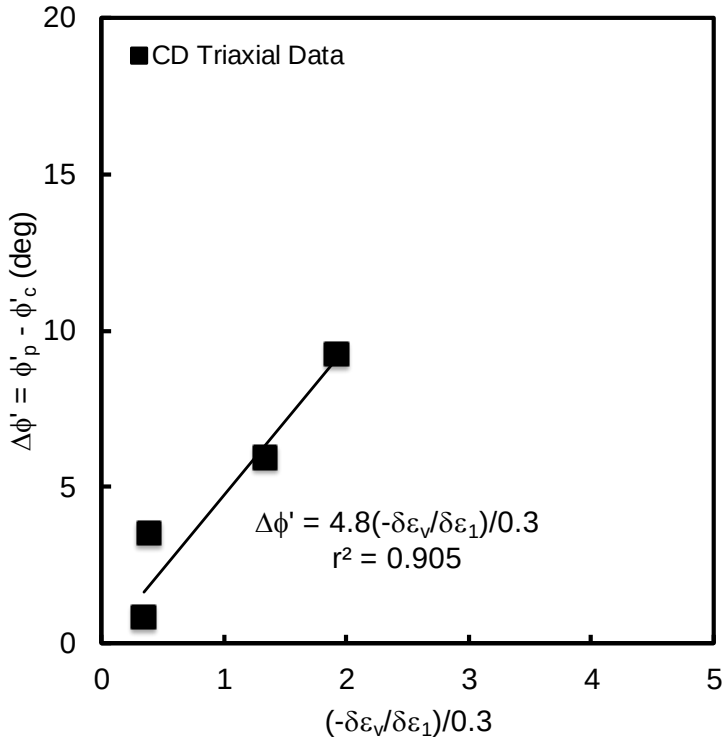

Figure 3.2. Assessment of Bolton (1986) A_f parameter from triaxial tests.

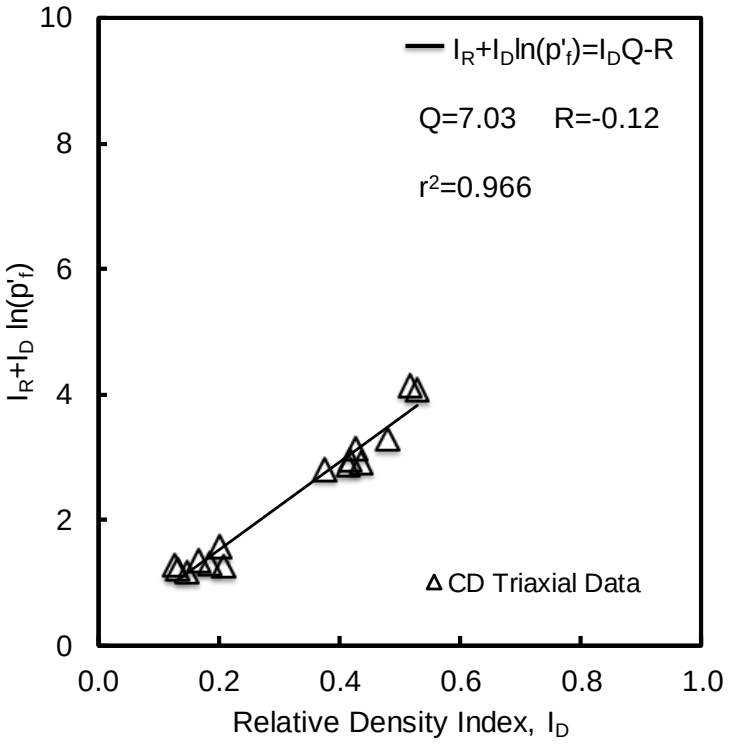

Figure 3.3. Calibration of Bolton (1986) stress-dilatancy Q and R parameters.

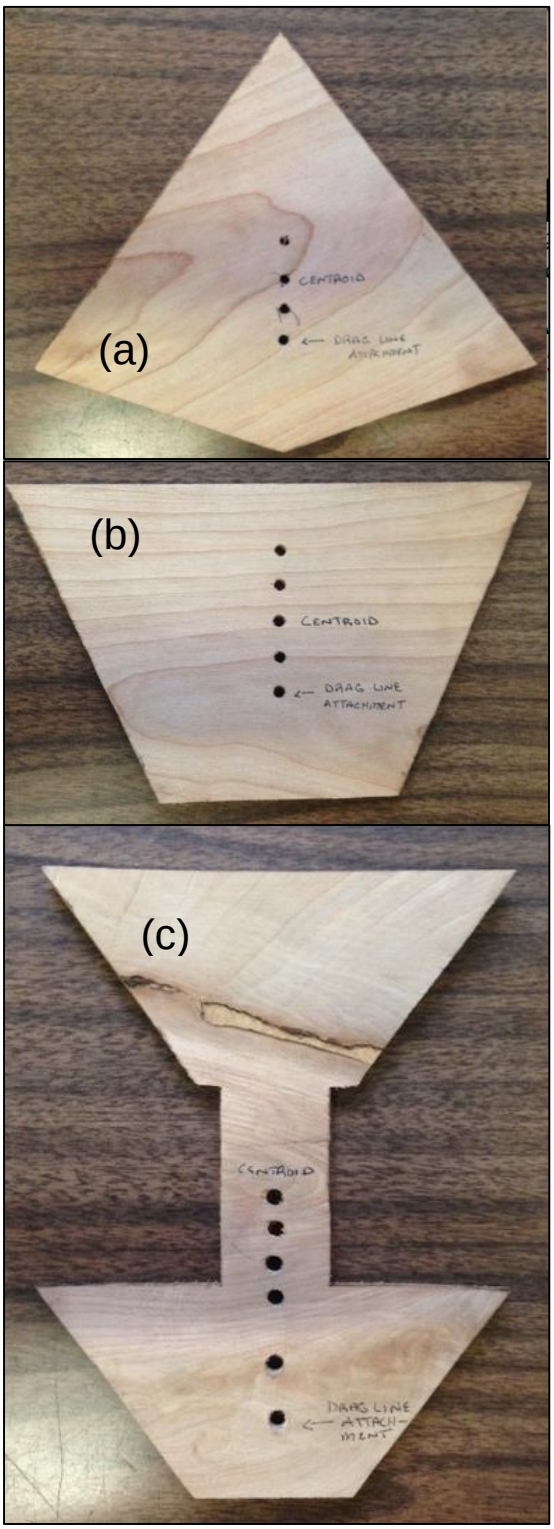

Figure 3.4. Model-scale anchors: (a) kite; (b) trapezoid; and (c) double connected trapezoid or bi-wing.

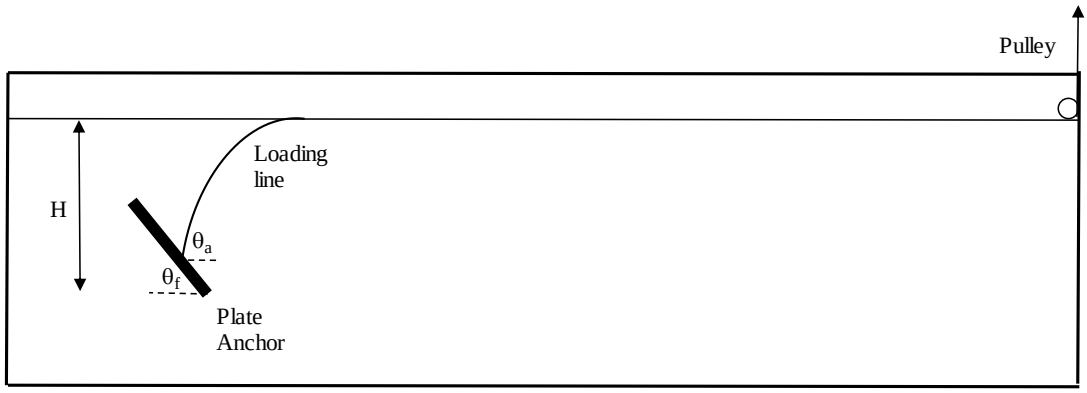

Figure 3.5. Cross-section of drag embedment test setup.

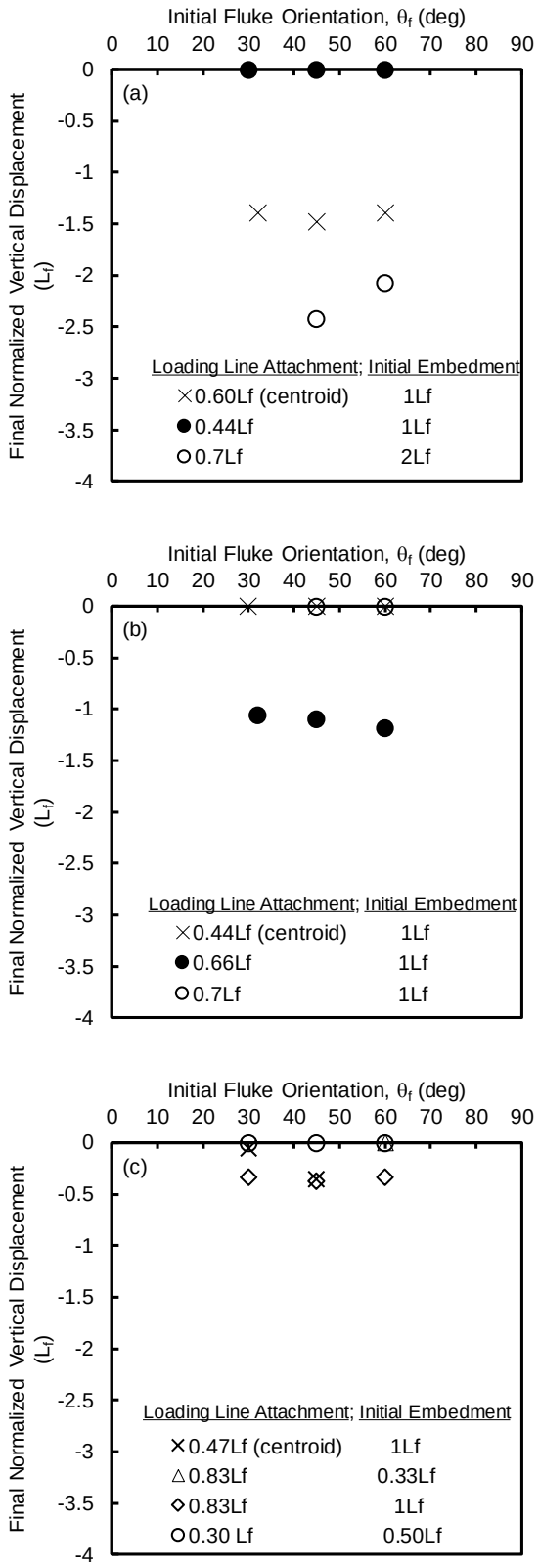

Figure 3.6. Summary of preliminary dive trajectory results for: (a) kite anchor; (b) trapezoid anchor; and (c) bi-wing.

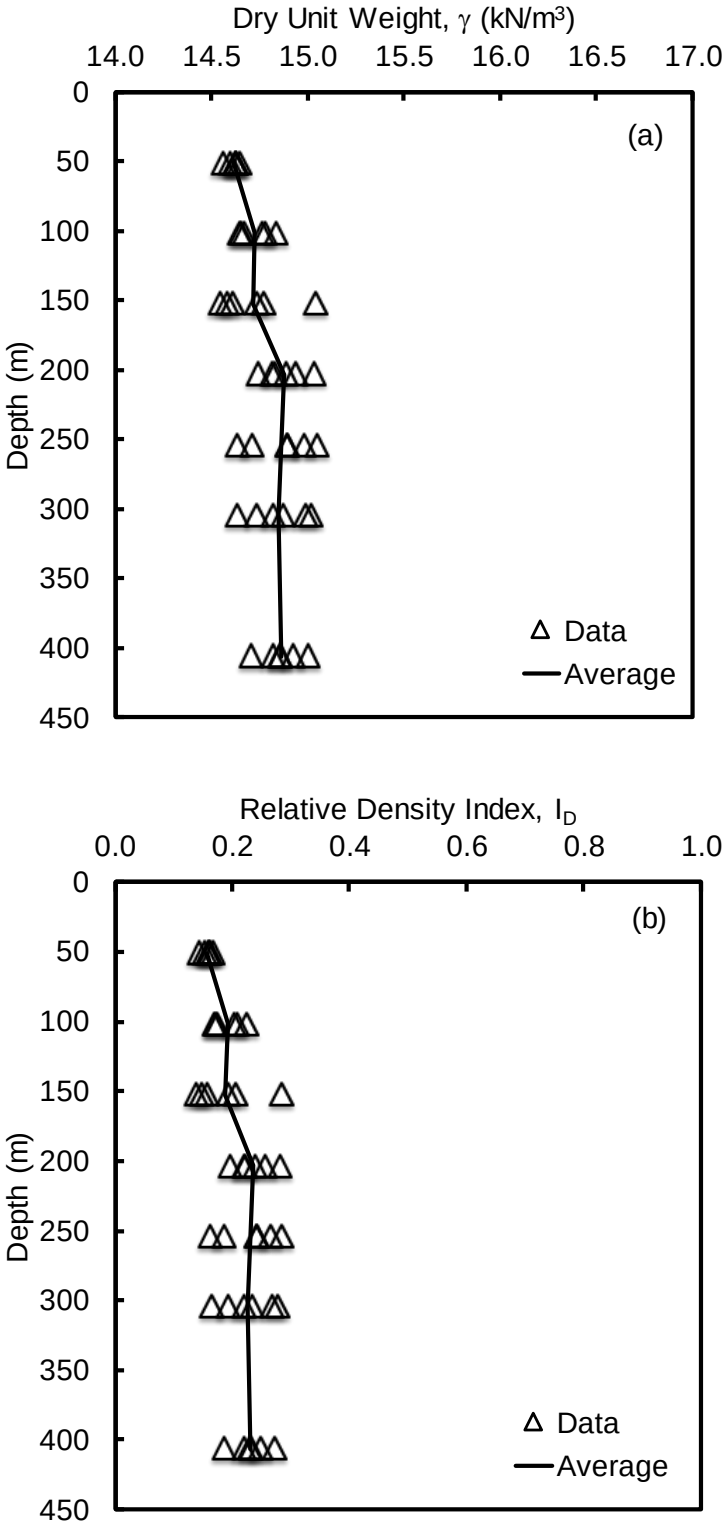

Figure 3.7. Typical profiles of: (a) dry unit weight; and (b) relative density index obtained within the test container.

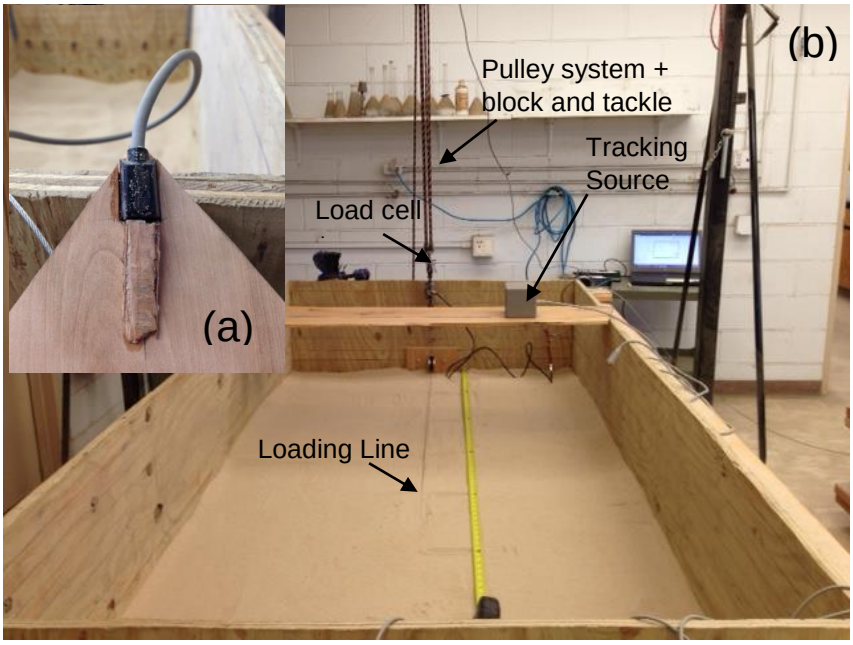

Figure 3.8. (a) Location of Polhemus magnetometer on model anchor; and (b) overview of laboratory test setup.

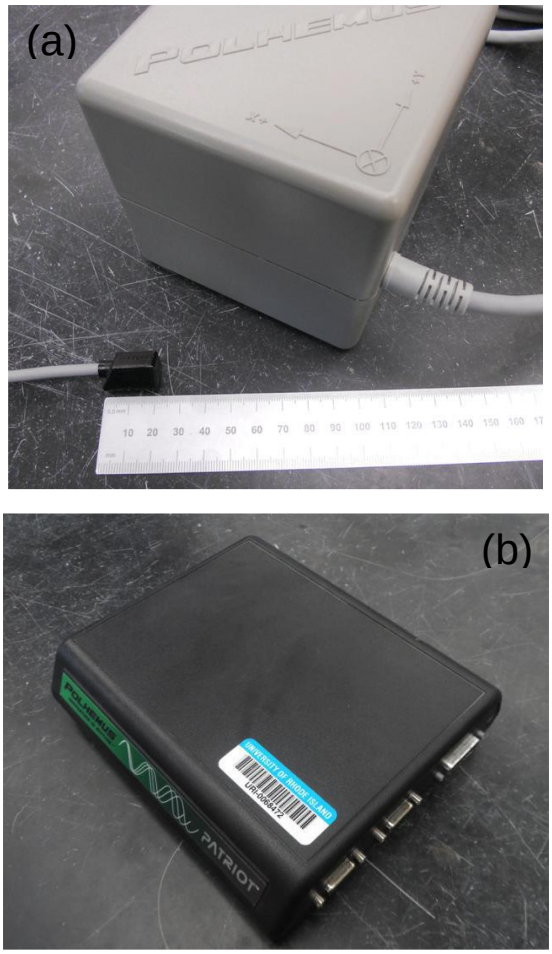

Figure 3.9. (a) Polhemus magnetometer and source; and (b) polhemus electronics unit.

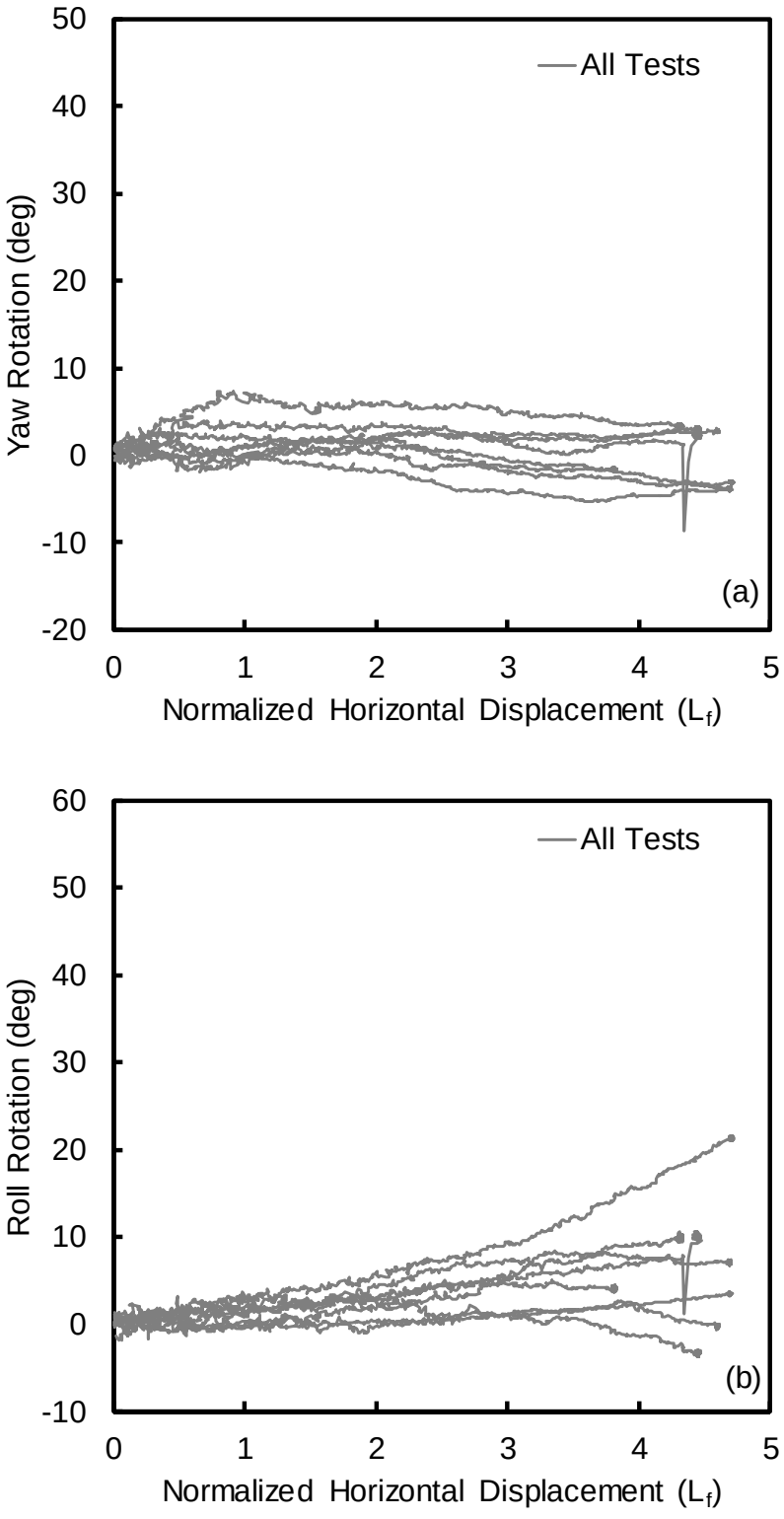

Figure 3.10. Out-of-plane rotation of model anchor during drag: (a) yaw rotation; and (b) roll rotation.

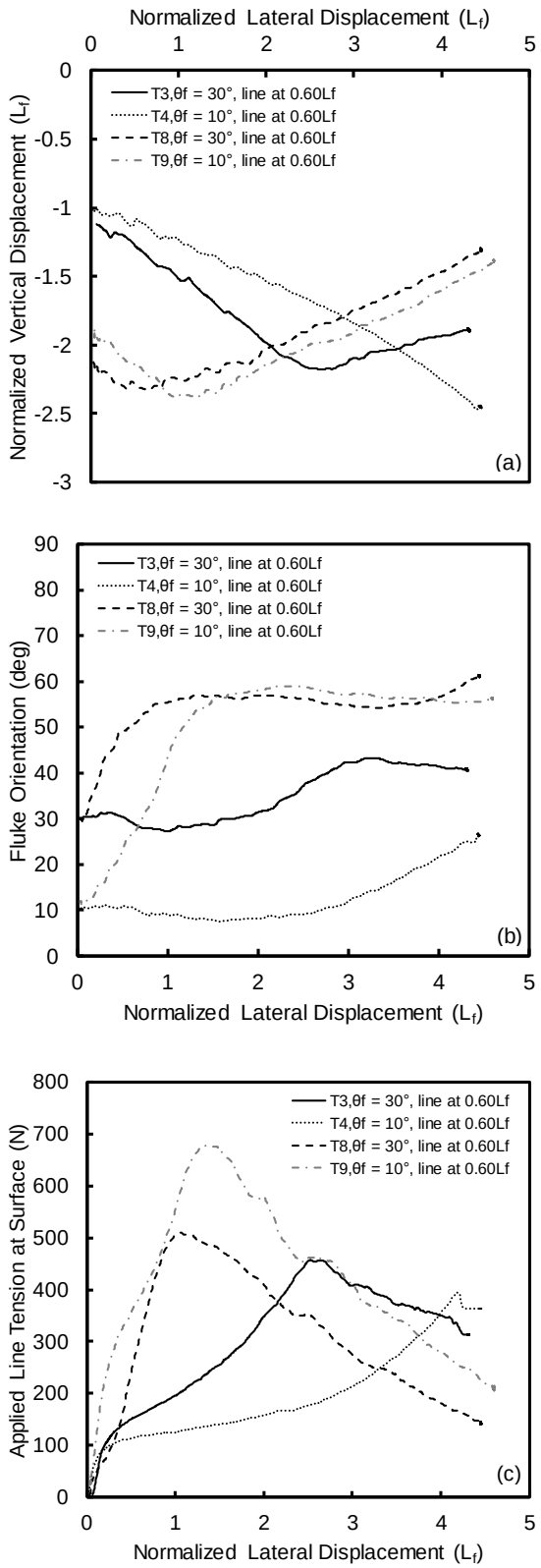

Figure 3.11. Effect of initial embedment depth on: (a) dive trajectory; (b) fluke orientation during drag; and (c) loading line tension applied at the soil surface.

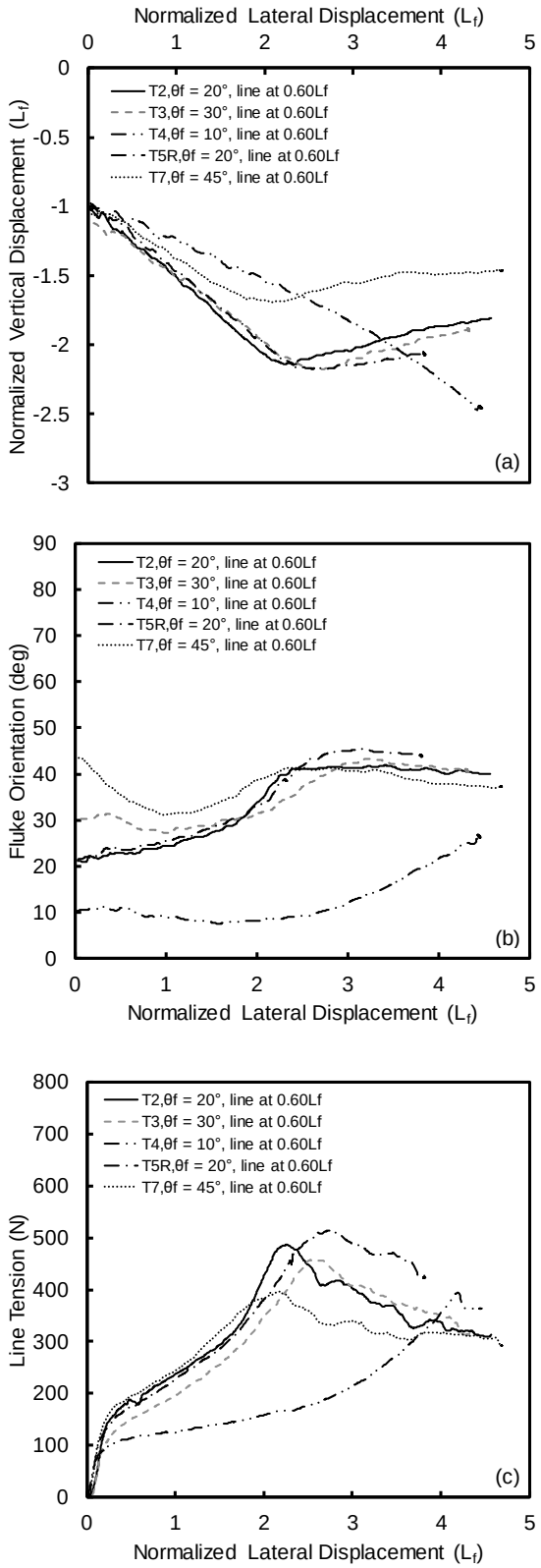

Figure 3.12. Effect of initial fluke orientation on: (a) dive trajectory; (b) fluke orientation during drag; and (c) loading line tension applied at the soil surface.

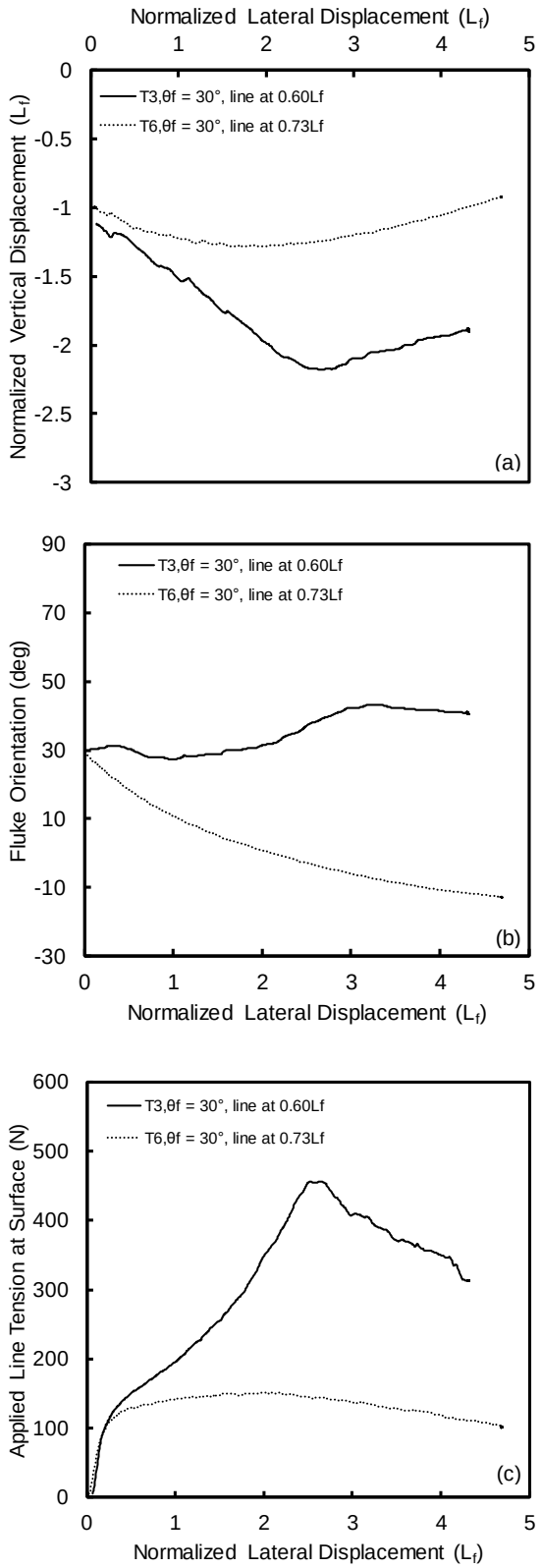

Figure 3.13. Effect of loading line attachment on: (a) dive trajectory; (b) fluke orientation during drag; and (c) loading line tension applied at the soil surface.

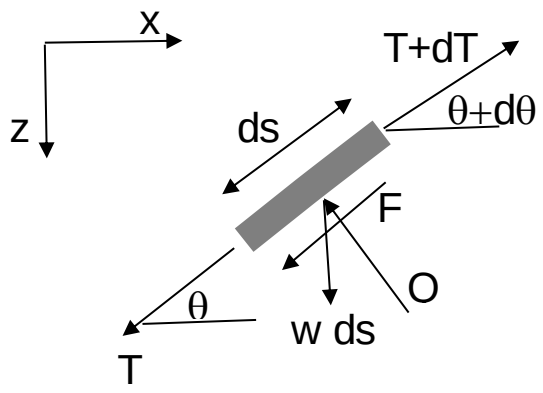

Figure 3.14. System of forces acting on a segment of embedded loading line.

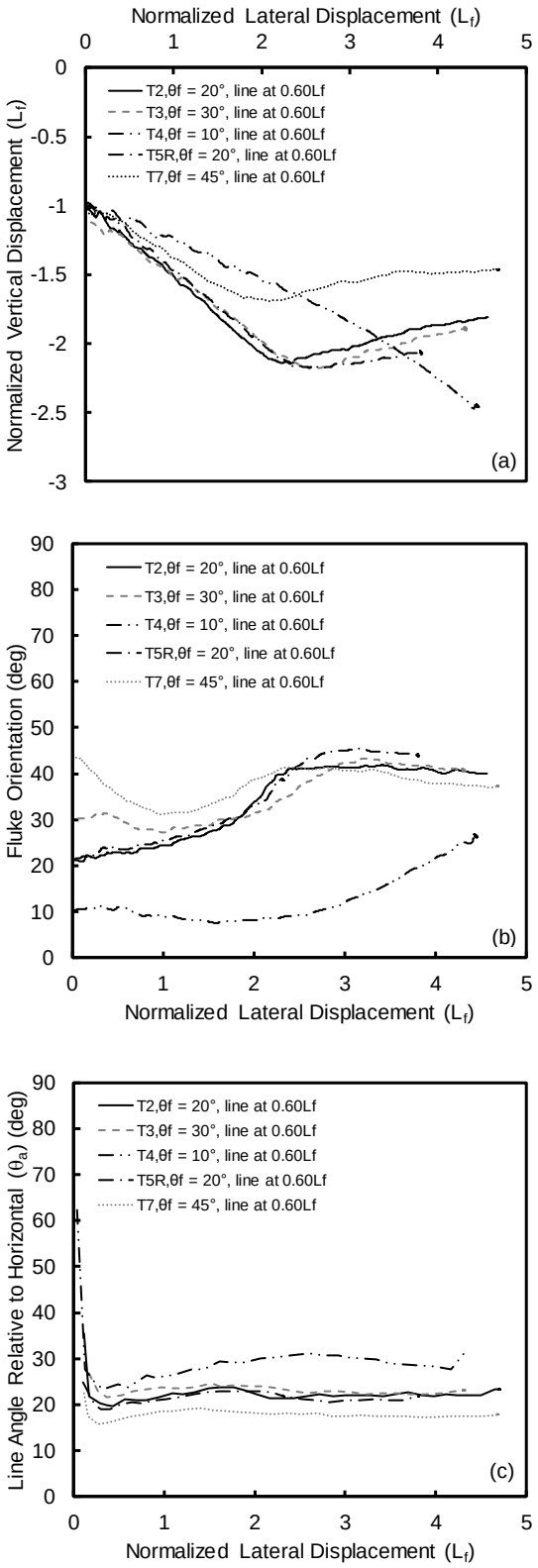

Figure 3.15. Relationship between fluke orientation and loading line angle (a) dive trajectory; (b) fluke orientation during drag; and (c) loading line angle at attachment relative to the horizontal.

4. Experimental Study of Load Interaction on a Novel Drag-Embedded Plate Anchor in Sand

Prepared for submission to ASCE Journal of Geotechnical and Geoenvironmental Engineering

Abstract

This paper presents an experimental study to investigate the normal and shear force interactions that occur during drag embedment of a novel plate anchor in sand that is initially embedded through free-fall penetration. Prediction of the trajectory and final embedment depth of the anchor is critical to determining its ultimate holding capacity. The capacity in the normal and shear (i.e. parallel) direction will control the trajectory and thus it is important to therefore know if the presence of one component of the mooring line force in one direction influences the resistance in the other direction. As a first step toward understanding this interaction, the resistance of a simple kite-shaped plate anchor is measured under pure normal, shear (i.e. parallel), and rotational loading. Force components acting on the fluke were extracted from a series of drag embedment experiments where the anchor movement was tracked in all six-degrees of freedom. The results suggest there is minimal interaction between the normal and shear components acting on a simple fluke during dive trajectory in sand.

Introduction

As offshore wind development moves into deeper water, floating substructures secured to the seafloor through anchoring systems become a viable and economical foundation alternative to traditional fixed-jacket or gravity-based structures (O'Neill et al. 2003; Musial and Butterfield 2006). To properly secure these buoyant structures in position, anchoring systems are often sought after due to their efficiency to resist uplift forces, and ability to achieve very deep embedment. Mooring systems such as catenary, taut or semi-taut, and vertical tendons provide the connections from the structure to the anchors below

the seabed (Randolph and Gorvenec 2011). Some of the anchoring systems that have been used include drag embedment anchors (DEA), drag-in vertically loaded plate anchors (VLA), as well as those installed by suction caissons such as suction embedded plate anchors (SEPLA) (Bradshaw et al. 2015).

The Author is currently researching a new green anchor concept called the "flying wing anchor" as described in Gerkus et al. (2016). The motivation for the concept is to reduce the amount of energy to transport and install the anchor into the seabed. Similar to a torpedo pile, the anchor is dynamically installed vertically into the seabed through free-fall penetration. After initial penetration, the anchor, in concept, will rotate and dive into a position that is near normal to the anchor line in response to the service loads imposed by the structure. For the anchor to be effective it should have a shape that is hydrodynamically stable, and maximizes the drag embedment in the soil.

Knowledge of the final embedment depth and orientation of a drag-type anchor is critical to evaluate the in-service performance including the ultimate holding capacity. To predict the anchor dive trajectory or kinematic behavior, a variety of approaches have been used. These include methods based on limit equilibrium where the trajectory is solved by incrementally advancing the anchor into the soil; it assumes that the anchor will move along the path of least resistance and parallel to the fluke, thus the soil resistances acting on the anchor at its failure condition will dictate the direction of movement (e.g. Stewart 1992; Neubecker and Randolph 1996a; Neubecker and Randolph 1996b; Thorne 1998;

Dahlberg 1998; Ruinen 2004; Liu et al. 2012). Plasticity limit analysis methods have been proposed primarily in soft clays were a yield locus is used to characterize the plastic failure behavior of the anchor during its trajectory; the yield loci are expressed as a combination of normal, shear, and moment forces acting on the anchor, thus incremental anchor displacements are calculated under the given loading combination (e.g. Murff 1994; Martin 1994; Bransby and O'Neill 1999; O'Neill et al. 2003; Kim 2005; Murff et al. 2005; Aubeny et al. 2005; Aubeny et al. 2008; Aubeny and Chi 2010). This approach typically assumes associated flow where the displacement of the anchor occurs normal to the yield loci.

In some types of foundation systems, it is recognized that the capacity in one mode of failure may be reduced by the presence of loads in other directions. For example, in shallow foundations the bearing capacity can be substantially reduced under the presence of a shear load (e.g. Meyerhof 1953; Hansen 1970). This led to the development of inclination factors that adjust the bearing capacity for the load interaction effect. Subsequently, more complex interaction diagrams have been proposed that account for a combination of normal, shear, and moment loads (e.g. Gottardi et al. 1999); Aubeny and Chi 2010). Though the interaction diagram (or yield loci) approach has been applied to drag embedment anchors in clay under undrained loading, the author is unaware of any studies that have considered the force interaction of a plate-type drag embedment anchor in sand under drained conditions. As a first step, the objective of this study is to investigate if there is a similar interaction between the normal and shear force components during drag embedment on a simple plate anchor that is initially embedded in sand. This will be achieved in the

laboratory by performing a suite of 1g physical model experiments involving a kite-shaped plate anchor as described below.

Scaling Considerations

It is important to consider scale effects so that the results can be reliably interpreted. Bradshaw et al. (2016) showed that scale effects can be minimized in 1g plate anchor experiments by presenting capacity in a dimensionless form, $q/\gamma H$, where q is the plate bearing pressure, γ is the dry unit weight of the sand, and H is the embedment depth from the soil surface to deepest part of the anchor, and by scaling the constitutive behavior of the soil. Soils will generally have a higher strength in small-scale 1g models due to higher dilation at low confining pressures. Therefore, the scaling of the constitutive behavior involves preparing the soil looser in the model than at full-scale to get a similar dilation response. Consistent with current centrifuge scaling laws presented in Garnier and Gaudin (2007), experiments were also designed such that the width of the anchor was at least 48 times the median diameter (D_{50}) of the sand to ensure there was a sufficient number of particles over the width of the plate.

Test Sand and Characterization

The sand used in this study primarily consists of a natural deposit of quartz beach sand obtained from Westerly, Rhode Island. The sand has been used extensively in physical 1g model experiments on plate anchors after Bradshaw et al. (2015; 2016) and Gerkus et al. (2016). Characterization of the sand included standard index and consolidated drained (CD) triaxial testing. The index properties are summarized in Table 4.1.

The peak friction (ϕ'_p) and dilation angles (ψ_p) were estimated using the Bolton (1986) stress-dilatancy relationship in order to handle the stress dependent changes in the angles at low stresses. The relationship is expressed as

$$\phi'_p - \phi'_c = A_f \left(I_D \left[Q - \ln\left(p'_f\right) \right] - R \right) \tag{4.1}$$

$$\phi'_p - \phi'_c = \beta \psi_p \tag{4.2}$$

Where ϕ'_p = peak friction angle, ϕ'_c = critical state friction angle, ψ_p = peak dilation angle, I_D = relative density index = $(e_{max}-e)/(e_{max}-e_{min})$, e_{max}, e_{min} = maximum and minimum void ratios, respectively, and e = void ratio of the prepared sample, p'_f = the mean effective stress at failure, and Q, R, A_f, and β = Bolton's fitting parameters.

Triaxial tests were performed to calibrate Bolton's fitting parameters for the sand used in this study. The triaxial samples were prepared using dry pluviation with a funnel in an attempt to achieve a similar fabric as the sand in the physical 1g model experiments. A range of relative density (D_r) between 13% (I_D = 0.13) and 53% (I_D = 0.53) could be achieved by varying the opening size of the funnel. The critical state friction angle was determined from extrapolating the peak friction angle at zero dilation angle (Bolton 1986), and the fitting parameters (Q, R, A_f, β) were determined from the linear regression plots shown in Figures 4.1-4.3 (Bradshaw et al. 2016). A summary of the fitting parameters can be seen in Table 4.1.

Sample Preparation

The sand was rained into a rigid test tank having dimensions of 2.4 m length x 1.2 m width x 0.9 m height using a portable pluviator based on Gade et al. (2013). All experimental testing was performed in a sand with relative density, $D_r \approx 20\%$ ($I_D \approx 0.20$). The pluviation device consisted of a bucket attached to a flexible hose leading to a pipe containing a plate with holes and a stack of sieves. The unit weight of the soil was determined by pluivating sand into small cups of a known volume (413 cm^3) that were placed on the soil surface at various depths during preparation. An example of the dry unit weights measured during pluviation in the test container is shown in Figure 4a along with corresponding calculated relative density index in Figure 4b. The relative density indices were fairly consistent throughout the container with a coefficient of variation of less than 0.2. The relative density in laboratory model was equivalent to 35% to 40% (I_D = 0.35 to 0.40) at full-scale to account for scale effects (Bradshaw et al. 2016). Additionally, the corresponding peak friction and dilation angles in each test container, on average, were 39^o and 10^o, respectively.

Pure Loading Behavior of Kite Anchor

The first step to understanding, predicting, and controlling the behavior of the proposed anchor concept is to establish its resistance to pure bearing, shear, and rotation (Gerkus et al. 2016). For the purpose of this study only the resistances in pure normal and shear (i.e. parallel to fluke) will be of focus, however results under pure rotation will be presented for completeness. The loading modes of the anchor are shown in Figure 4.5, which include a vertical (fluke orientation = $\theta_f = 90^o$) and horizontal anchor ($\theta_f = 0^o$) loaded perpendicular

(i.e. normal) and parallel (i.e. shear) to the fluke, and pitch rotation. Preliminary experiments on the kite-shaped anchor indicated that most of the resistance of the plates was due to the bearing resistance of the surfaces normal to the loading direction (i.e. bearing capacity). For this reason, the following non-dimensional quantities were used to describe the normal and shear resistance components

$$\frac{F_n}{\gamma H A_{fluke}} \tag{4.3}$$

$$\frac{F_s}{\gamma H A_{le}} \tag{4.4}$$

Where F_n, F_s = the forces in the normal and shear directions, respectively; A_{fluke} = fluke area; A_{le} = projected area of the leading edge of the anchor; γ = dry unit weight; and H = embedment depth from the soil surface to deepest point of the anchor.

Resistance of Kite Anchor Loaded Parallel to Fluke

Two model anchors were used to assess the resistance when loaded in the shear direction or parallel to the anchor fluke (Figure 4.5a/b). The model used for the vertical oriented anchor (Figure 4.5a) was fabricated from 12.7 mm thick structural steel with a fluke length (L_f) and width (B) equal to 127 mm and is shown in Figure 4.6. Similarly, the horizontal oriented anchor (Figure 4.5b) was fabricated from the same structural steel with a fluke length and width approximately equal to 197 mm and 236 mm, respectively, shown in Figure 4.7.

The vertical oriented anchor was pushed into the soil using a steel rod with a diameter of 9.5 mm and length of 483 mm attached at the tip (or top) of the anchor to provide a smooth, controlled, and continual penetration. To ensure constant penetration of the anchor, reaction weights totaling 1.4 kN were placed at the top of the steel rod directly above a load cell. The anchor was started at the soil surface and displaced vertically into the soil, a distance of $3.5L_f$. When the anchor was placed horizontally, it was "wished" into place at normalized embedment depths (H/L_f) of 1, 2, and 3. Due to limitations of the test tank the anchor was displaced laterally a distance of $2L_f$. Both testing configurations displaced the model anchors at a constant rate of 50 mm/s using an electric hoist, and a block and tackle system. Loads were measured with a load cell having a capacity of either 0.89, 2.2, or 11.1 kN (CAS SBA and Omega LC), and displacement was measured with a string potentiometer (Measurement Specialists SP2-50). The loading rate was significantly higher than other studies, but strain rates have shown to be negligible on the strength of dry sand (e.g. Whitman and Healy 1962) (Bradshaw et al. 2016).

The results of the vertical and horizontal oriented anchor tests are shown in Figures 4.8 and 4.9, respectively. The non-dimensional shear resistance curves shown in Figure 4.8 suggest that the resistance is essentially constant with depth below a normalized embedment of approximately 1. The large variability in the normalized resistance indicated at very shallow depths ($< 1L_f$) is caused by a small bearing area in combination with very low effective stresses near the soil surface, thus causing Eqn. (4.4) to produce large values near the surface. The resistance, on average, ranged from 75 to 80, and appear to be independent of embedment depth. It is important to note that the anchor was continuously pushed, and

the calculated resistances represent a fully mobilized value, whereas if the anchor had been placed at a specified embedment depth and then loaded, it would require the anchor to deform some amount before reaching a peak. Lastly, analysis of the results has indicated that the resistance is primarily being controlled from end bearing at the nose of the anchor, and considering the bearing area is much smaller than the embedment depth, it is likely the failure mechanism is local or "deep", suggesting that it is being controlled by the shear strength of the soil near the anchor nose. Because the resistance is increasing approximately linearly with depth, the normalization is accounting for the increase in overburden stress leading to constant normalized resistances for $\theta_f = 90^o$.

The results presented in Figure 4.9 for the anchor experiments at $\theta_f = 0^o$ show an early peak with minimal softening. The cause of this is due to the nature of the test and failure mode, such that the anchor can be displaced laterally without any rotational movement or vertical displacement; thus the overburden pressure remains constant on the anchor. Two curves are shown per initial embedment in Figure 4.9 and indicate a repeat test. The curves are nearly identical and were performed to ensure accuracy of the results. The normalized resistance shows to be largest at an initial normalized embedment of $2L_f$, while the resistances at $1L_f$ and $3L_f$ were nearly indistinguishable; the resulting normalized bearing factors ranged from 34 to 45. Therefore, it is evident that with increasing embedment depth, there is only a slight increase in resistance. It is further assumed that the resistance is being controlled primarily by the net passive resistance of the soil with some resistance due to interface friction (negligible). Similar to the previous anchor tests, normalization should account for the linearly increasing friction with increasing depth, thus resulting in an

approximate constant normalized resistance with depth. This effect is similar to what was found in the measured results.

The primary conclusions of the model anchor experiments loaded parallel to the anchor fluke indicate:

- The loading modes were likely controlled by a local or "deep" failure mechanism near the nose of the anchor, due to the bearing area being significantly smaller than the embedment depth.
- The normalized resistance is dependent on fluke orientation, such that the resistance increases between $\theta_f = 0^o$ and $\theta_f = 90^o$. However, the resistance is relatively independent of embedment depth. The resulting non-dimensional shear resistances, on average, are 38 at $\theta_f = 0^o$ and 75 at $\theta_f = 90^o$.

Resistance of Kite Anchor Loaded Normal to Fluke

The model used to assess the resistance of the kite anchor loaded normal to fluke at $\theta_f = 0^o$ and 90^o (Figure 4.5c/d), is identical to the one used in Figure 4.7 and consists of a fluke length and width of 197 mm and 236 mm, respectively. The test setup for both horizontal and vertical oriented anchors consists of the anchor being "wished" into place at specified embedment depths. For the horizontal oriented anchor tests, the anchor was started at initial normalized embedment's of 1, 2, 3, and 5, and displaced vertically until completely out of the soil. Similarly, the vertical oriented anchor tests began at initial H/L_f's of 1 and 2, and

laterally displaced approximately $2L_f$. Displacements and loads were measured and controlled using the same experimental setup as the tests loaded parallel to the anchor fluke.

Figures 4.10 and 4.11, respectively, present the results of the vertical and horizontal oriented anchor tests loaded normal to the fluke. The resistance of the normal vertical anchor tests showed signs of an early peak and softening behavior for H/L_f of 1 and 2. Two causes of the softening behavior are attributed to the dilative nature of the soil at the low confining stresses in the test container, and the slight upward movement of the anchor at large lateral displacements which would reduce the overburden pressure and ultimately the resistance. Repeat tests were performed at a normalized embedment of 1, and showed to be identical resulting in a peak normalized resistance of 8.5. With an increase in embedment, the peak normalized resistance increased to approximately 11.5 at H/L_f of 2 (Figure 4.10). Conceptually, the resistance as the anchor is displaced laterally is due to the net lateral earth pressure. With increasing embedment depth, the failure changes from a shallow to deep mechanism; when the anchor is shallow ($H = 1L_f$) the soil is undergoing a wedge type failure that extends from the bottom of the anchor to the soil surface. Alternatively, as the embedment increases, the failure mechanism becomes more localized around the fluke area resulting in a higher normalized value.

The normalized load-displacement behavior shown in Figure 4.11 for a horizontal anchor loaded normal to the fluke. The results indicate an increase in pullout resistance with increasing embedment. All tests show a clear peak capacity followed by a softening behavior due to the reduction in soil overburden and confining pressure as the anchor is

pulled out of the soil. For anchor test starting at H/L_f = 1 to 3, the peak pullout capacity occurred at approximately $0.2L_f$ of displacement relative to the initial embedment depth. As the normalized embedment increased from 3 to 5, slightly more displacement (approximately $0.5L_f$) was required before reaching the peak pullout capacity. The peak normalized resistance was calculated as 2.1, 3.7, 6.1, and 6.6, for initial embedment's of $1L_f$, $2L_f$, $3L_f$, and $5L_f$, respectively. It is well established that the failure mechanism of a horizontal anchor loaded normal to the fluke changes from a wedge-type failure to a local or "deep" failure at about $H/L_f \geq 5$, thus providing some explanation in the deviation of capacity from H/L_f of 1 to 5.

The primary conclusions of the model anchor experiments loaded normal to the fluke indicate:

- A significant increase in capacity for a vertical oriented anchor between normalized embedment's 1 and 2. This change may be linked to the transition from shallow to deep failure mechanism.
- The capacity of a horizontal oriented anchor increases nonlinearly with increasing embedment depth.
- Results indicate that the non-dimensional normal resistance is dependent on the fluke orientation and embedment depth. The resistance increases with increasing fluke orientation and depth.

Resistance of Kite Anchor Subject to Pitch Rotation

To properly model the dive trajectory of the proposed wing-anchor concept it is crucial to capture the resistance in all failure modes including rotation (Figure 4.5e). As the anchor dives into the soil, it will inevitably undergo some degree of rotation. The focus of the current study is on the interaction behavior between the normal and shear component, therefore the resistance to pure pitch rotation is presented only for completeness.

Figure 4.5e depicts the failure mode of the anchor subject to pure pitch rotation. The model anchor was tested at three normalized embedment depths of 1, 2, and 3, where it was "wished" into place. The anchor was fabricated from 15.9 mm thick aluminum with a fluke length and width of approximately 197 mm and 236 mm, respectively. To rotate the anchor in pure pitch, the anchor was fixed at the centroid to a 15.9 mm diameter aluminum rod with a length of 610 mm to fully intersect the width of the test tank; the rod was designed to accommodate the anticipated applied moments with the experimental setup is shown in Figure 4.12. On either side of the test container two holes were drilled out to accommodate the aluminum moment rod; either hole was fit with a ball-bearing flange to minimize friction during rotation. The torque throughout the test was measured using a 226 N-m torque sensor (Omega Engineering) and the anchor was rotated manually via a level arm at a constant rate. A magnetic tracking device was fixed at the tip of the anchor to measure rotation, as well as, a manual measurement for comparison purposes. Details of the magnetic tracking device will be discussed later.

The results are presented in Figure 4.13 as a normalized moment resistance with respect to fluke orientation. The normalization of the moment is expressed similar to Eqns. (4.3) and (4.4) as

$$\frac{M}{\gamma H L A_{fluke}} \tag{4.5}$$

Where M = the applied moment including shear and bearing components; and L = the length of an equivalent fluke = $\sqrt{A_{fluke}}$. The moment resistance is anticipated to be from the net bearing resistance on the fluke.

The anchor was rotated between approximately 130^o to 180^o relative to the vertical. A clear peak resistance followed by a softening behavior can be seen for all of the experiments. However, at a normalized embedment depth of $1L_f$ the resistance increased following a first peak around 100^o; the cause of this may be explained due to the shallow embedment where the sand surface collapsed during rotation following the first peak, i.e. the mobilized soil wedge increases until the anchor is almost horizontal, and after the 90^o rotation the soil mobilization behavior repeats (Figure 4.13). For the remaining tests embedded at 2Lf and 3Lf it is anticipated that the soil is flowing almost locally around the anchor during rotation, reflecting the strain-softening behavior. Biarez et al. (1965) showed that failure mechanism transitions from a shallow to local failure between a normalized embedment of 0 and 6. Since the shear strength of the soil should increase near linear with depth, the normalization

of stress should be accounting for this behavior causing an approximate normalized resistance with increasing depth.

Dive Trajectory Study of the Kite Anchor

A series of dive trajectory experiments were performed on the kite-shaped anchor with a free moving shank (or loading line) along the long axis of the fluke. The anchor was fabricated from 0.51 cm thick plywood with an approximately fluke area of 120 cm^2. Measurements of all six-degrees of motion and loading line tension during embedment were made. Using the pluviation technique, the plate anchor was placed at a desired depth and fluke orientation during sample preparation within the rigid test container. Upon completion of the test sample, the anchors were fully embedded as shown in Figure 4.14. The kite anchor was placed at normalized embedment's of 1 and 2, with fluke orientations of 10^o, 20^o, 30^o, and 45^o. Lastly, the loading line location was varied to investigate the effects on dive performance. A very thin steel cable, having a diameter of 1.59 mm was used during loading to help reduce the soil friction along the loading line. During the drag experiments a six-degree-of-freedom magnetic tracker (magnetometer by Polhemus) was used to measure position (i.e. x-y-z) and orientation (i.e. yaw [azimuth], pitch [elevation], roll) of the anchor as it moves through the soil in real time. Additional sensors included a 2.2 kN (CAS SBA) load cell and string potentiometer (Measurement Specialties SP2-50). The magnetometer was recessed on the back of the plate anchor before testing, while the load cell and string potentiometer were connected to the far end of the loading line beyond the pulley shown in Figure 4.15.

Tracking Position and Orientation

Anchor position and orientation was measured using a Polhemus magnetic tracking device as shown in Figure 4.16. The system consists of a sensor, source, electronics unit, and software package (Patriot User Manual 2008). The source receives the electromagnetic waves produced from the sensor during testing and is then converted to rotation and displacement measurements via a calibration that is performed by the manufacturer. The system generates its own magnetic field when in operation, and if highly magnetic objects are in close proximity to either the source and/or sensor, the internal calibration will be temporarily altered. This interference becomes noticeable in the system's live display and can be fixed by moving magnetic objects out of range and by locating the source within 127 mm of the sensor.

Translation readings from the magnetometer are measured with respect to the center of the source; the positive x and y directions are marked on the sensor and the right hand rule is used to determine the positive z direction. The rotational angles are presented as Euler angles and are expressed in terms of rotating frames. The yaw (azimuth) is rotation around the z-axis, pitch (elevation) is rotation around the y-axis, and roll is rotation around the x-axis. The sensor first measures the yaw angle with respect to the external frame of x-y-z, next a new coordinate system is set (x'-y'-z') and the pitch rotation is measure with respect to this new frame, and finally, another coordinate system is set (x"-y"-z") to measure the roll rotation. The amount of rotation the anchor undergoes in each direction during loading is important for anchor dive trajectory tests, but using Euler angles may be misleading when extracting the exact behavior. Consequently, to measure the change in each rotation

at a given interval or frame, the rotational angles should be measured with respect to a fixed axis of x-y-z rather than rotating axes, thus requiring a correction to be made to the magnetometer output (Gerkus 2016). This correction to the rotational output can be made by using a direction cosine matrix (R) that can be expressed for this magnetometer as

$$R = \begin{bmatrix} \cos\psi\cos\theta & \cos\psi\sin\theta\sin\varphi - \sin\psi\cos\varphi & \cos\psi\sin\theta\cos\varphi + \sin\psi\sin\varphi \\ \sin\psi\cos\theta & \sin\psi\sin\theta\sin\varphi & \sin\psi\sin\theta\cos\varphi - \cos\psi\sin\varphi \\ -\sin\theta & \cos\theta\sin\varphi & \cos\theta\cos\varphi \end{bmatrix} \quad (4.6)$$

Where ψ = yaw; θ = pitch; and φ = roll. The direction cosine matrix is calculated for each measurement frame and then multiplied by the inverse of the matrix (R^{-1}) of each measurement frame. Next, the sum of the change in angles calculated with respect to this "new" frame gives the change in yaw, pitch, and roll angles with respect to a fixed axis. The rotation results presented in this study show the real time anchor movement in each direction calculated using this method.

Experimental Results

Eight dive trajectory experiments were performed where the initial fluke orientation, initial embedment depth, and loading line location were varied to investigate the effect on dive performance. Figure 4.17 presents typical results obtained from the experiments. The results are presented with respect to normalized lateral displacement and include the trajectory (i.e. vertical penetration), change in fluke orientation (θ_f) during dive, change in the loading line angle (θ_a) relative to the horizontal at the attachment point, and the change in loading line tension (T_a) at the attachment point. The results indicate that the simple

plate anchor configuration showed significant diving in sand with a free-moving loading line along the long axis of the fluke. However, it is important that the location of the free-moving loading line is attached close to the anchor centroid (≈0.60L_f); this will increase the amount of relative final embedment as shown by tests T3 and T6 in Figure 4.17a. Additionally, the tests indicate that diving may be optimized when attaching the loading line at the approximate centroid and by placing the anchor at an initial shallow fluke orientation of 10^o and initial embedment depth of 1L_f as shown by test T4 in Figure 4.17a. Resulting from this configuration was a loading line angle between 25^o and 30^o relative to the horizontal, which is also consistent with the angle that causes diving for a VLA as shown by Liu et al. 2010.

Analysis of Interaction

As a first order approximation the interaction between the normal and shear components was assessed using the pure loading and dive trajectory experiments. It should be noted for the majority of the drag experiments very little rotation was observed as the anchor was diving. This was attributed to the anchor shape, and location of the loading line; the loading line attachment point was located at the anchor centroid and close to center of pressure resulting in a small eccentricity on the anchor and minimizing rotation early on in the experiments. However, the anchor did exhibit significant rotation during the uplift phase of the experiments due to the change in eccentricity. The eccentricity is controlled by the distance from the fixed attachment point to the center of pressure, and with increasing embedment the center of pressure varies causing an increase in the eccentricity. However,

the current experimental configuration was not set up to obtain the change in center of pressure throughout dive trajectory.

The shear and normal force components acting on the fluke during its trajectory were calculated for each drag experiment based on the fluke orientation, loading line angle relative to the attachment, and loading line tension at the attachment expressed as

$$F_n = T_a \sin(\theta_f + \theta_a) \quad (4.7)$$

$$F_s = T_a \cos(\theta_f + \theta_a) \quad (4.8)$$

Where F_n, F_s = the force acting in the normal and shear directions relative to the fluke; and T_a = loading line tension at the attachment point. Next the trajectory results were analyzed to obtain the absolute change in displacement caused by the force in the normal direction (dn) and the force in the shear direction (parallel to the anchor fluke) (ds). Plots of non-dimensional normal resistance and non-dimensional shear resistance can be created along with vectors representing the movement direction.

Figure 4.18 presents the vector plots representing the two types of behavior that were observed in the experiments. Movement purely in the shear direction is indicated when the direction vectors are parallel with x-axis, and movement purely in the normal direction is indicated when the direction vectors are parallel with the y-axis. An increase in displacement in either the shear and/or normal directions is indicated by an increase in

length of the displacement vectors. This is caused by an increase in magnitude of the shear and/or normal forces acting on the fluke. For test T4, constant vertical penetration was observed, thus the displacement vectors become larger with increasing force and primarily point parallel with the shear or x-axis (Figure 4.18a). Alternatively, test T9 showed a slight vertical penetration or movement parallel to the fluke at early stages of drag indicated by the small vectors pointing along the x-axis in Figure 4.18b. As lateral displacement increased in test T9, the anchor began to move out of the soil causing an increase in the force normal to the fluke and a decrease in the force parallel to the fluke. The anchor movement now becomes perpendicular to the fluke and is represented by the vectors changing orientation and pointing near parallel with the normal or y-axis in Figure 4.18b. The decrease in the normal and shear component is caused by the anchor moving toward the soil surface (i.e. reduction in overburden pressure).

The vector plots created from each test are essentially representative of a yield surface. Given a combination of loading, movement in the normal and/or parallel to the fluke will occur, and are represented by the displacement vectors. It is obvious that the anchor movement does not always occur normal or perpendicular to the yield surface, suggesting that for a drag anchor in sand normality does not hold and therefore follows a nonassociated flow rule.

Using the vector plots created from each drag embedment test, force component data are selected at moments when the anchor was primarily diving (i.e. anchor movement parallel

to the fluke) and pulling out (i.e. anchor movement normal to fluke). These resistances were then compared to the normal and shear resistances obtained through pure loading to assess the interaction between either component. Figure 4.19a compares the results of the pure shear resistance to points within serval drag embedment experiments where both a shear and normal component are present on the fluke, and movement is primarily occurring parallel to the fluke. It is evident that the pure loading resistance parallel to the fluke increases with increasing orientation, however, due to an absence of data it is difficult to definitively define a trend. for simplicity it is assumed to be a linearly increasing trend from 0^o to 90^o. Thus, the forces acting in the shear direction during drag, regardless of the magnitude of the normal force, follow the increasing resistance trend offered by the pure loading results. Additionally, the shear values are within a ±20% boundary, indicated by the dashed lines, over a range of fluke orientations. This suggests that the magnitude of the shear component does not seem to be affected by the presence a normal component.

Alternatively, results from the drag embedment tests were taken when the anchor began to pullout indicating movement was primarily occurring normal to the fluke. The results are compared to the pure loading values shown in Figure 4.19b. Similar to Figure 4.19a, it is unknown of the exact trend of the pure loading resistance loaded normal to the anchor fluke, except that the resistance increases with increasing fluke orientation. Therefore, it is assumed to be a linear increase with increasing fluke orientation. The values of resistance normal to the fluke obtained from several drag embedment tests show to plot within a ±20% boundary, and follow the assumed trend regardless of the magnitude of the shear

component acting on the fluke. This indicates that there is minimal interaction between the two present forces acting on the anchor during the dive trajectory.

Conclusions

The objective of this study was to experimentally investigate the interaction between the force components in the normal and shear direction that are simultaneously acting on a fully embedded plate during its trajectory. The plate anchor tested is inspired by a wing-anchor concept currently under development where it will install into the seabed under free-fall and, in concept, rotate and move into position in-service. The first step to understanding, predicting, and controlling the behavior of the proposed anchor concept is to establish its resistance to pure normal, shear, and rotation loading, and experimentally track the behavior during drag. As a first step, a series of 1g physical model experiments were carried out to assess the interaction between the forces acting normal and parallel to the fluke. Each drag embedment experiment was analyzed to extract the forces acting in both the normal and shear directions caused by the loading line tension at the attachment. At various locations during the dive trajectory where movement was primarily parallel with the fluke, the forces in the normal and shear directions were compared to the pure loading results for a horizontal and vertical oriented anchor loaded parallel to the fluke. A similar process was performed where movement was normal to the anchor.

The results suggest that both the force components in the normal and shear directions acting on the fluke during drag do not interact. This finding is inferred due to the magnitude of either force component falling within a similar range and increasing trend displayed by the

pure loading results, regardless the magnitude of the additional component in place. Furthermore, if no interaction is present between the force component in the normal and shear directions, the trajectory may be simply modeled using the pure loading resistances. However, it is warranted that additional pure loading experiments are performed at intermediate fluke orientations to properly define the overall resistance behavior and trend. Additional assessment of the interaction between the moment and normal component, as well as, interaction between the moment and shear component is warranted to fully develop a dive trajectory model.

Acknowledgments

This material is based upon work supported by the National Science Foundation under Grant No. 1300142 and also by the Science Foundation Ireland under the U.S.-Ireland R&D Partnership Program Grant No. SFI/2012/US/E2479. The Author's would also like to thank Kevin Broccolo at the University of Rhode Island for all of his fabrication efforts put forth to conduct this research. Thanks also to Sven Sivarajah for his assistance with the pure loading experiments.

References

Aubeny, C.P., Kim, B.M., and Murff, J.D. (2005). "Proposed upper bound analysis for drag embedment anchors in soft clays." *Proc. Frontiers in Offshore Geotech.*, ISFOG 2005, London, UK.

Aubeny, C.P., Murff, J.D., and Kim, B.M. (2008). "Prediction of anchor trajectory during drag embedment in soft clay." *Int. J. Offshore Polar Engrg.*, 18(4), 314-319.

Aubeny, C.P. and Chi, C. (2010). “Mechanics of drag embedment anchors in a soft seabed.”*J. Geotech. and Geoenviron. Engrg.*, 136(1), 57-68.

Biarez, I., Boucraut, L.M., and Negre, R. (1965). “Limiting equilibrium of vertical barriers subjected to translation and rotation forces.” *Proc. 6th Int. Conf. Soil Mech. Fnd. Engrg.*, 2, Montreal Canada, 368-372.

Bradshaw, A.S., Giampa, J., Dietrich, F., Gilbert, R.B., and Gerkus, H. (2015). “Pullout Capacity of Plate Anchors in Sand for Floating Offshore Wind Turbines.” *Proc., of the 3rd Inter. Symp. on Frontiers in Offshore Geotechnics*, Oslo, Norway: NGI. 833-838.

Bradshaw, A.S., Giampa, J.R., Gerkus, H., Jalilvand, S., Fanning, J., Nanda, S., Gilbert, R., Gavin, K., and Sivakumar, V. (2016). “Scaling Considerations for 1-g Model Horizontal Plate Anchor Tests in Sand.” *Geotech. Testing J.*, 39 (6), 1-9.

Bransby, M.F. and O'Neill, M. (1999). “Drag anchor fluke soil interaction in clays.” *Proc. Int. Symp. on Numerical Models in Geomechanics*, Rotherdam, Netherlands: Balkema. 489-494.

Bolton, M. (1986). “The strength and dilatancy of sands.” *Geotechnique*, 36(1), 65–78.

Dahlberg, R. (1998). “Design procedures for deepwater anchors in clay.” *Offshore Tech. Conf.,* Houston, TX.

Gade, V.K., Dave, T.N., Chauhan, V.B., and Daska, S.M., 2013, “Portable traveling pluviator to reconstitute specimens of cohesionless soils,” *Proc. of Indian Geotech. Conf.,* University in Roorkee, India.

Garnier, J., Gaudin, C., Springman, S.M., Culligan, P.J., Goodings, D., Konig, D., Kutter, B., Phillips, R., Randolph, M. F., and Thorel, L. (2007). “Catalogue of scaling laws and similitude questions in geotechnical centrifuge modeling.” *Int. J. Phys. Modell. Geotech.*, 7(3), 1-23.

Gerkus, H. (2016). “Model experiments to measure yield thresholds and trajectories for plate anchors and develop a new anchor concept”. Ph.D. Dissertation. University of Texas at Austin, Austin TX.

Gerkus, H., Giampa, J.R., Senanayake, A.I., Lai, Y., Huang, Y., Flores, J. E.I., Breithaupt, N.B., Sivarajah, S., Bradshaw, A. S., and Gilbert, R.B. (2016). “Preliminary development of a new concept to improve sustainability of offshore foundations.” *Proc. Geo-Congress Conference*, ASCE, IL.

Gottardi, G., Houlsby, G.T., and Butterfield, R. (1999). “Plastic response of circular footings on sand under general planar loading.” *Geotechnique*, 49(4), 453-469.

Hansen, B. (1970). “A revised and extended bearing capacity formula.” *The Danish Geotech. Institute Bulletin*, 27.

Kim, B.M. (2005). “Upper bound analysis for drag anchors in soft clay.” Ph.D. Dissertation. Texas A&M University, USA.

Liu, H., Zhang, W., Zhang, X, and Liu, C. (2010). “Experimental investigation on the penetration mechanism and kinematic behavior of drag anchors.” *Applied Ocean Research*, 32, 434-442.

Liu, H., Liu, C., Yang, H., Li, Y., Zhang, W., and Xiao, Z. (2012). “A novel kinematic model for drag anchors in seabed soils.” *Ocean Engrg.*, 49, 33-42.

Martin, C.M. (1994). “Physical and numerical modelling offshore foundations under combined loads.” Ph.D. Dissertation. University of Oxford.

Meyerhof, G.G. (1953). “The bearing capacity of foundations under eccentric and inclined loads.” *Proc. 3rd Int. Conf. Soil Mech. and Fnd. Engrg.*, ICSMFE, Zurich, 1, 440-445.

Murff, J.D. (1994). “Limit analysis of multi-footing foundation systems.” *Proc., 8th Int. Conf. on Computer Methods and Advances in Geomech.*. Abington, U.K.: Vol. 1, Taylor & Francis. 233-244.

Murff, J.D., Randolph, M.F., Elkhatib, S., Kolk, H.J., Ruinen, R., Strom, P.J., and Thorne, C. (2005). “Vertically loaded plate anchors for deepwater applications.” *Proc. Int. Symp. on Frontiers in Offshore Geotech.*, Perth, Australia: Balkema. 31-48.

Musial, W. and Butterfield, S. (2006). “Energy from offshore wind.” *Offshore Technology Conference*, Houston, TX.

Neubecker, S.R. and Randolph, M.F. (1996a). “The kinematic behaviour of drag anchors in sand”. *Can. Geotech. J.*, 33, 584-594.

Neubecker, S.R. and Randolph, M.F. (1996b). “The static equilibrium of drag anchors in sand”. *Can. Geotech. J.*, 33, 574-583.

O'Neill, M. P., Bransby, M. F., and Randolph, M.F. (2003). “Drag anchor fluke-soil interaction in clays.” *Can. Geotech. J.*, 40, 78-94.

Patriot User Manual. (2008, February). Polhemus

Randolph, M. and Gourvenec, R. (2011). *Offshore geotechnical engineering*, New York, USA: Spon Press.

Ruinen, R.M. (2004). “Penetration analysis of drag embedment anchors in soft clay.” *Proc. 14th Int. Offshore and Polar. Engrg. Conf.*, Toulon, France.

Stewart, W.P. (1992). “Drag embedment anchor performance prediction in soft clay.” *Proc. 24th Annual Offshore Tech. Conf.*, OTC 6970, Houston, TX.

Thorne, C.P. (1998). “Penetration and load capacity of marine drag anchors in soft clay.” *J. Geotech. Geoenviron. Engrg.*, 124, 945-953.

Whitman, R. V. and Healy, K. A., 1962, “Shear Strength of Sands During Rapid Loadings,” *J. Soil Mech. Found. Div.*, 88(SM2), 99–131.

Table 4.1. Properties of test sand.

Property	Value
γ_{max} (kN/m^3)	18.1
γ_{min} (kN/m^3)	14.1
e_{min}	0.44
e_{max}	0.84
D_{50} (mm)	0.30
G_s	2.65
ϕ'_c (deg)	32.3
Q	7.03
R	-0.12
A_f	4.75
β	0.69

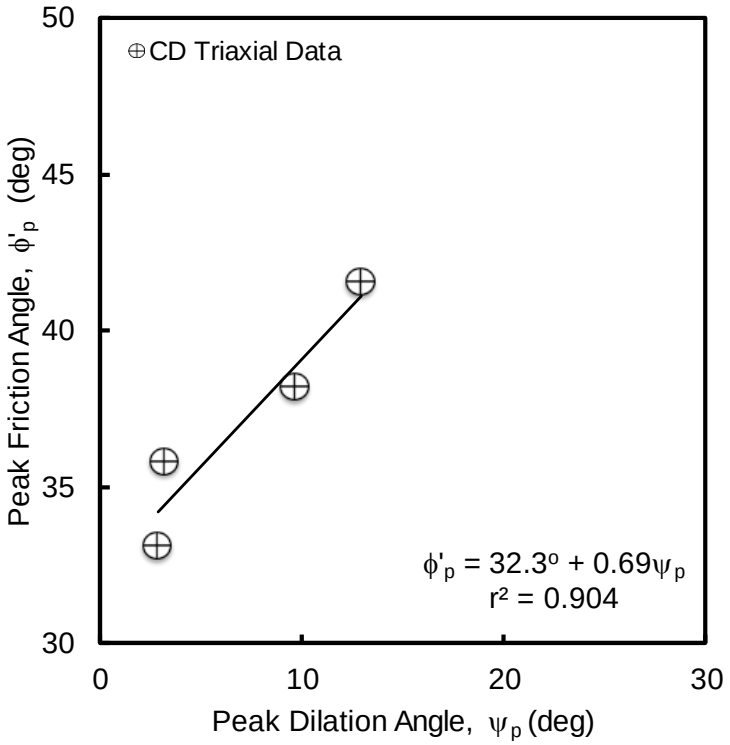

Figure 4.1. Relationship between peak friction and dilation angles for Westerly, RI sand measured in triaxial tests.

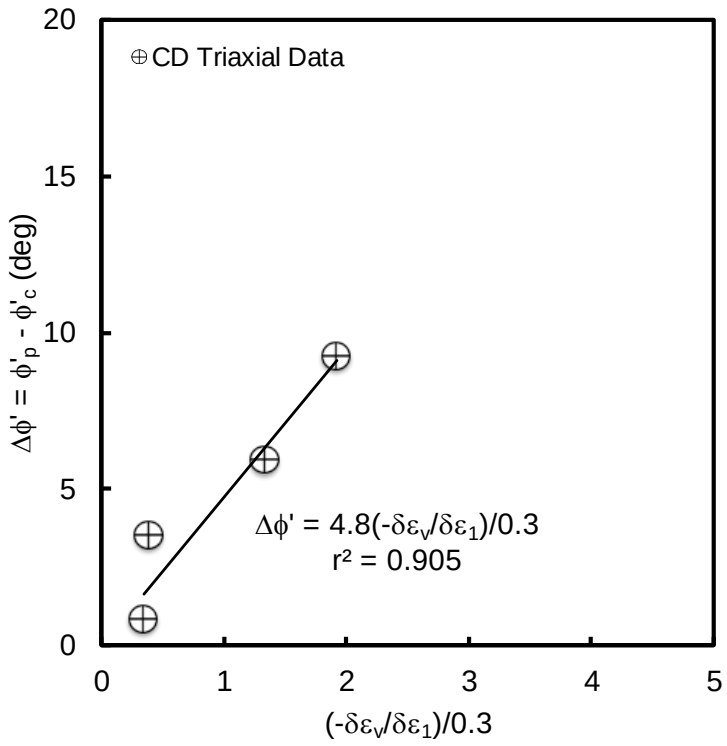

Figure 4.2. Assessment of Bolton (1986) A_f parameter from triaxial tests.

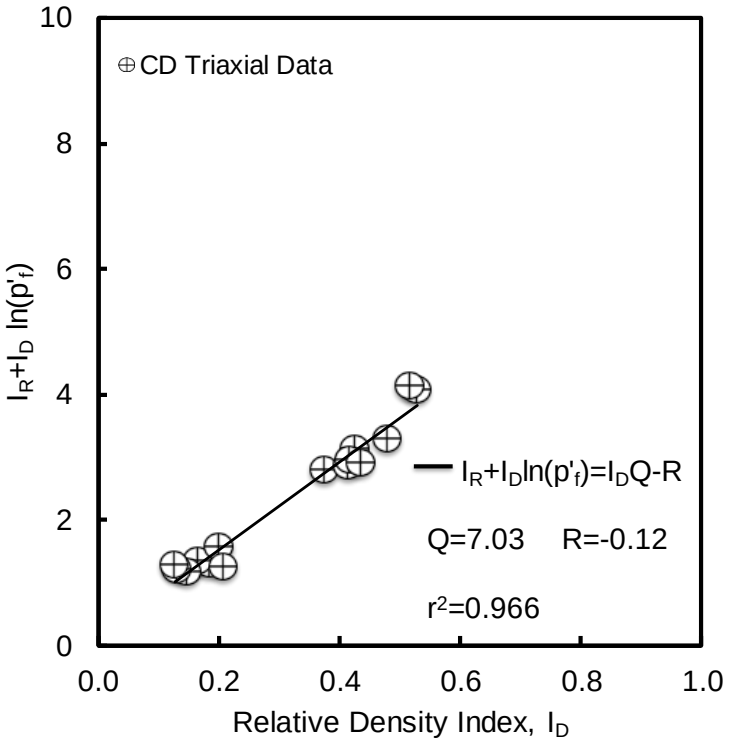

Figure 4.3. Calibration of Bolton (1986) stress-dilatancy Q and R parameters.

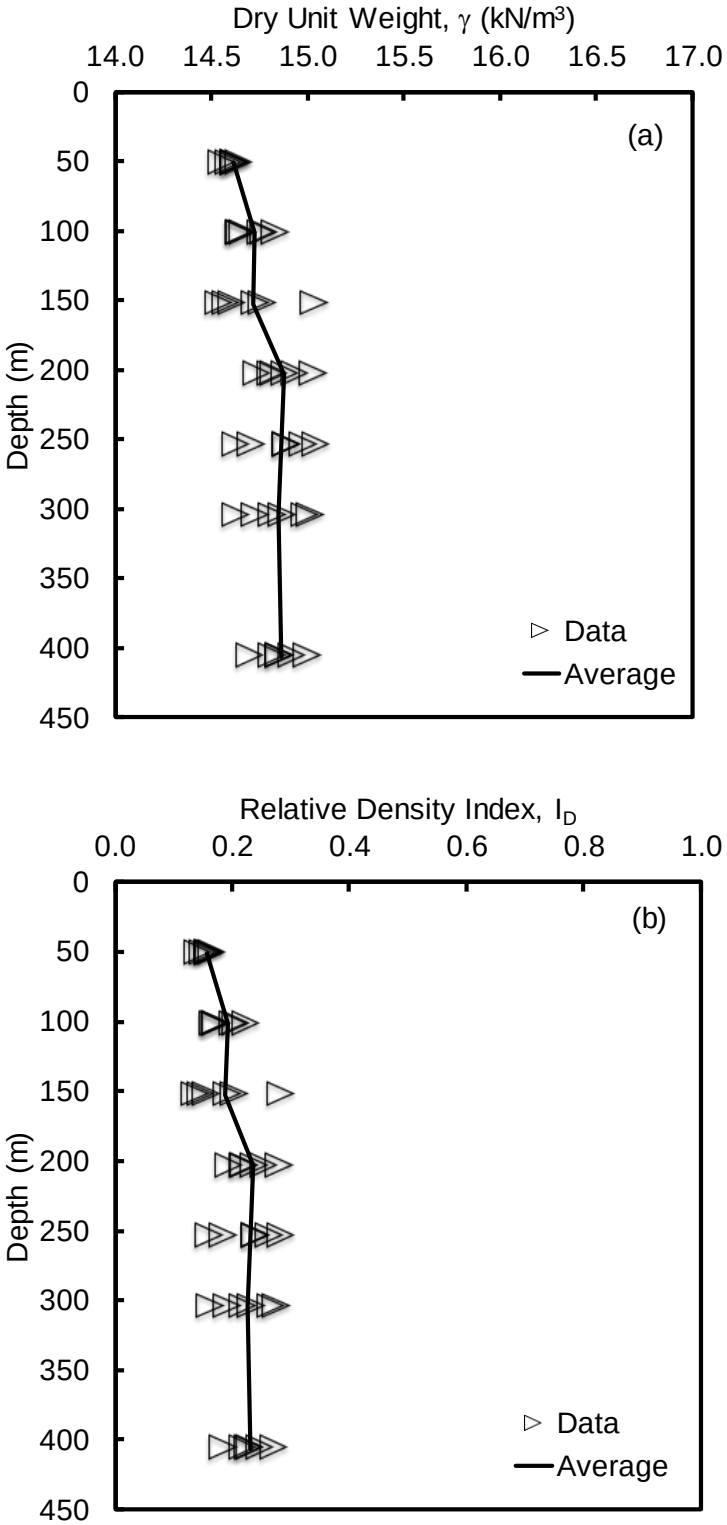

Figure 4.4. Typical profiles of: (a) dry unit weight; and (b) relative density index obtained within the test container.

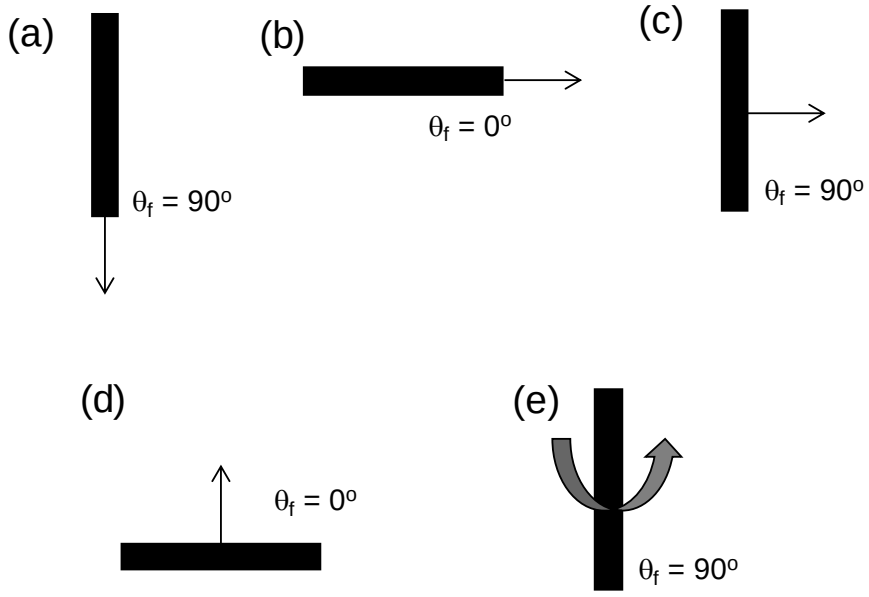

Figure 4.5. Pure loading failure modes for: (a) vertical anchor loaded parallel to fluke area; (b) horizontal anchor loaded parallel to fluke area; (c) vertical anchor loaded normal to fluke area; (d) horizontal anchor loaded normal to fluke area; and (d) vertical anchor subject to pure pitch rotation.

Figure 4.6. Photograph of the anchor model with attached rod used for pure loading of a vertical anchor loaded parallel to the fluke area.

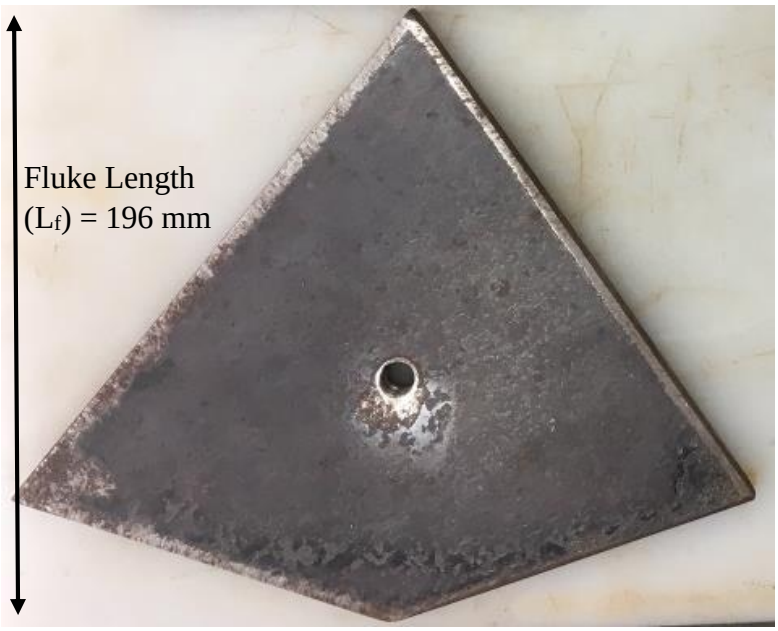

Figure 4.7. Photograph of the anchor model used for pure loading of a vertical and horizontal anchor loaded parallel and normal to the fluke area.

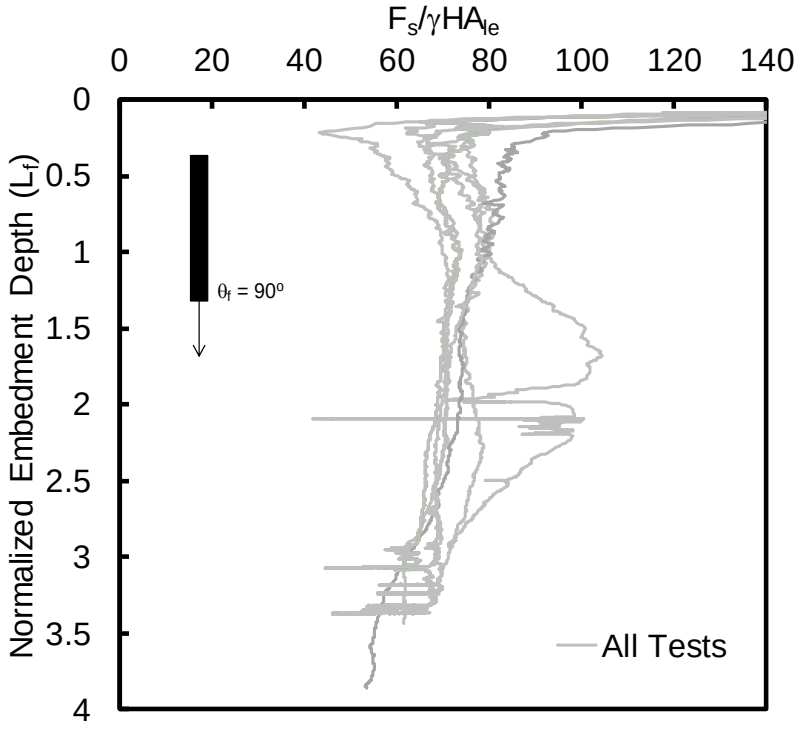

Figure 4.8. Pure loading results for a vertical anchor loaded parallel to the fluke area expressed as a non-dimensional shear resistance.

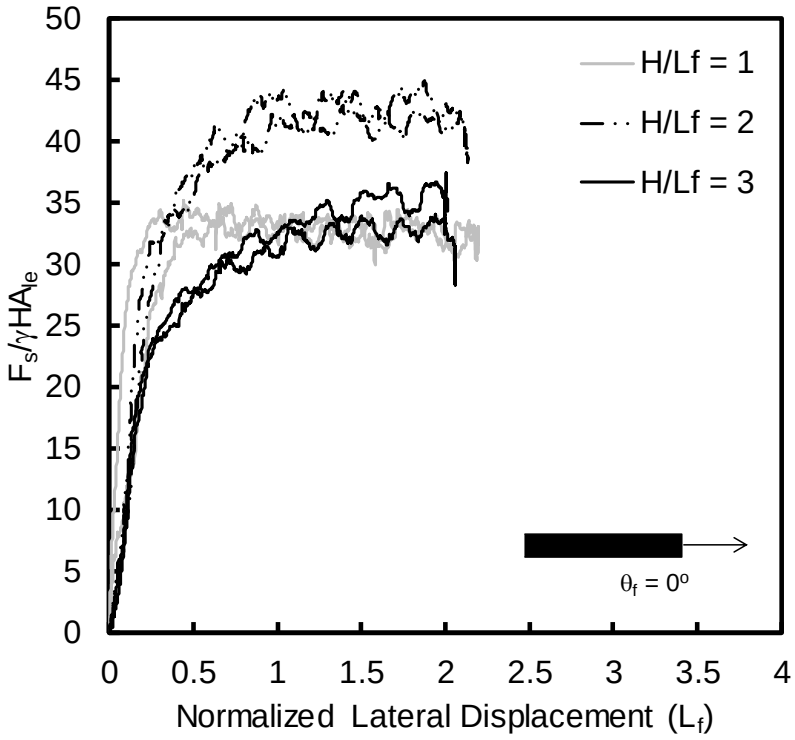

Figure 4.9. Pure loading results for a horizontal anchor loaded parallel to the fluke area expressed non-dimensional shear resistance.

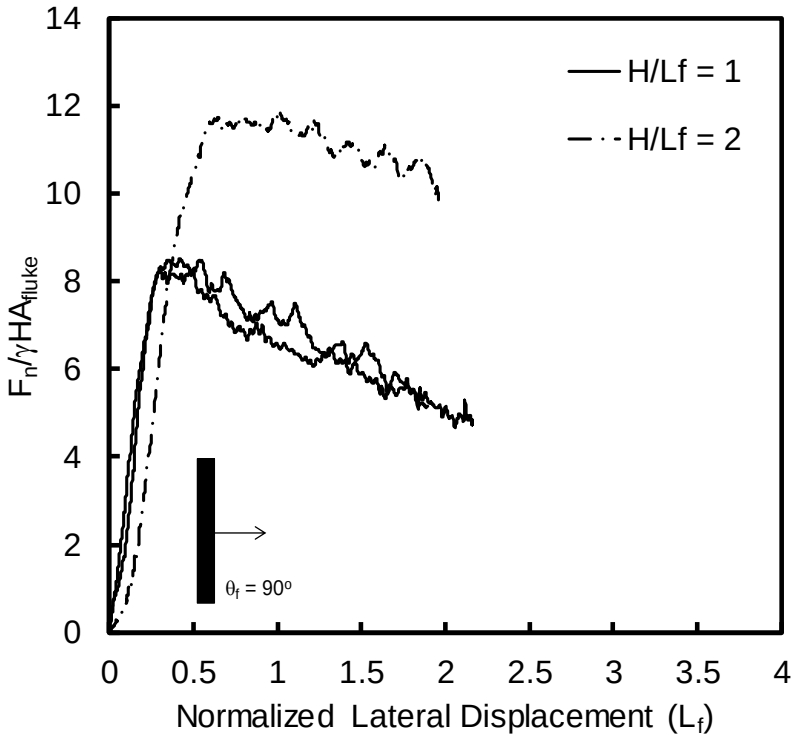

Figure 4.10. Pure loading results for a vertical anchor loaded normal to the fluke area expressed as a non-dimensional normal resistance.

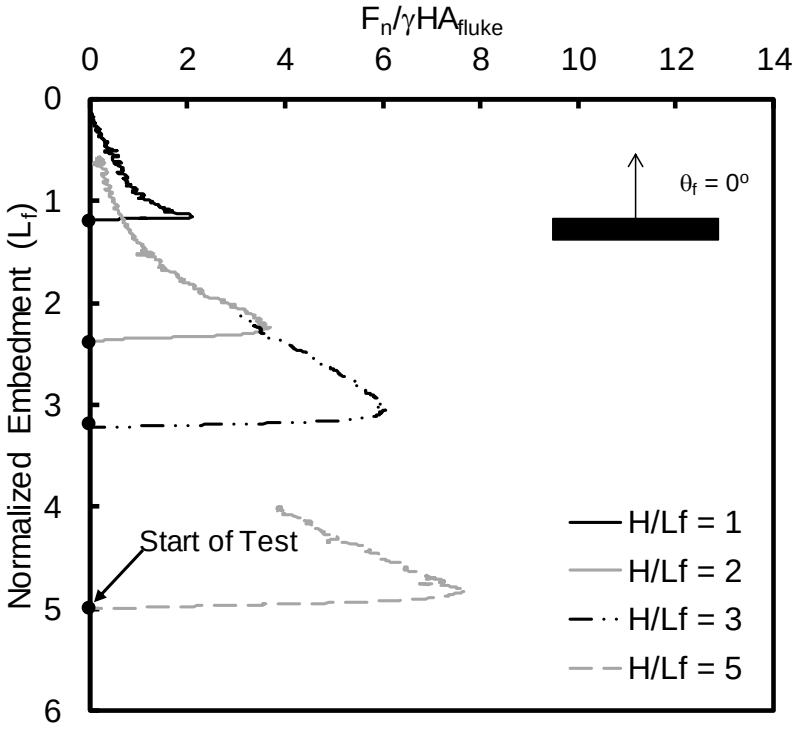

Figure 4.11. Pure loading results for a horizontal anchor loaded normal to the fluke area expressed as a non-dimensional normal resistance.

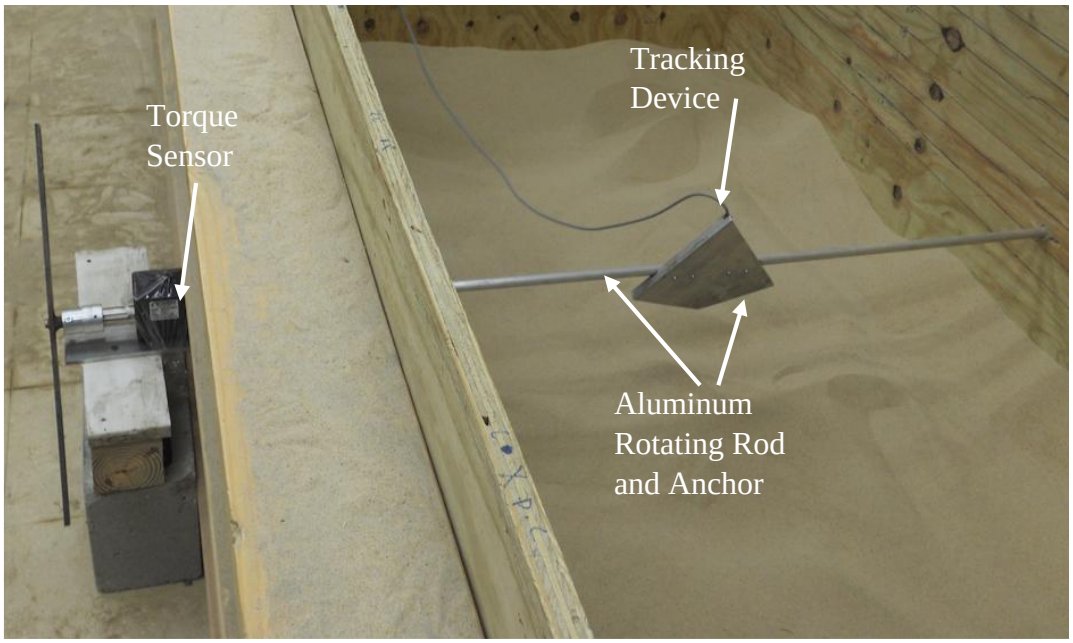

Figure 4.12. Experimental setup for pure pitch rotation loading.

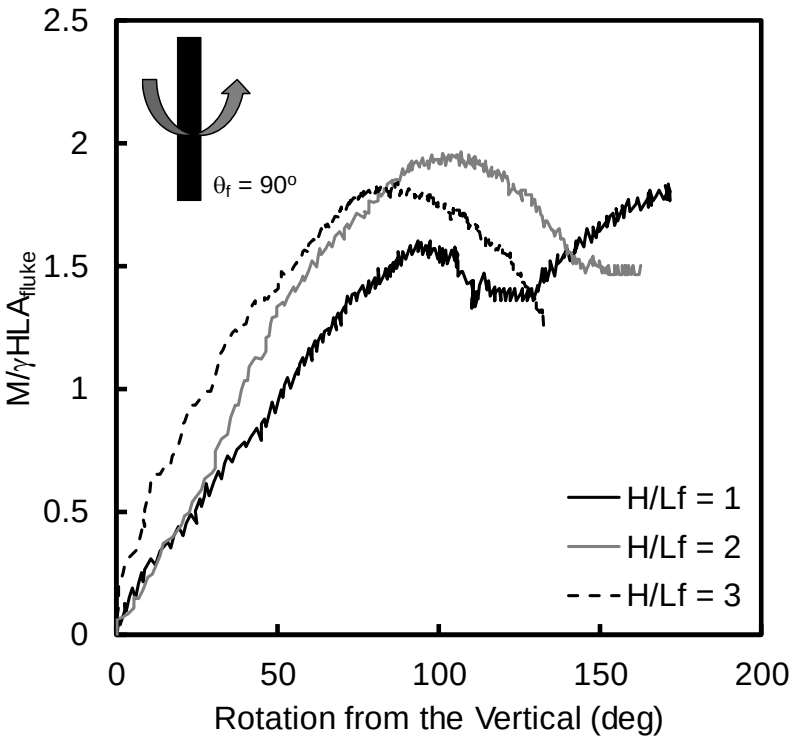

Figure 4.13. Pure loading results for a vertical anchor subject to pitch rotation expressed as a non-dimensional moment resistance.

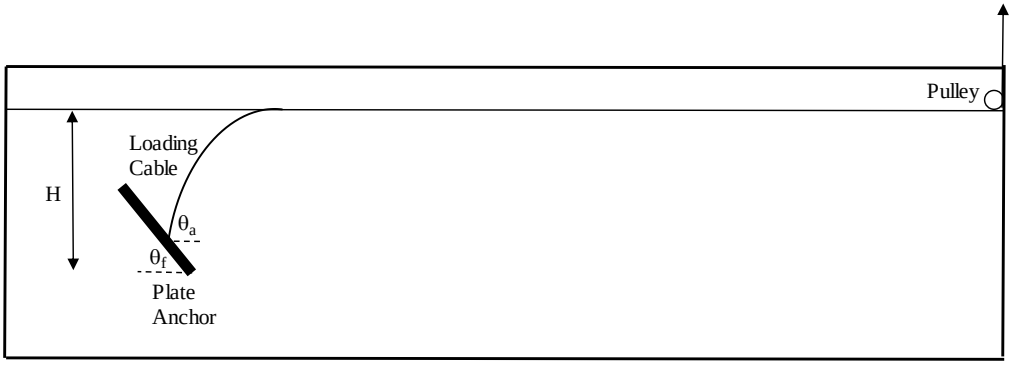

Figure 4.14. Cross-section of drag embedment experimental setup.

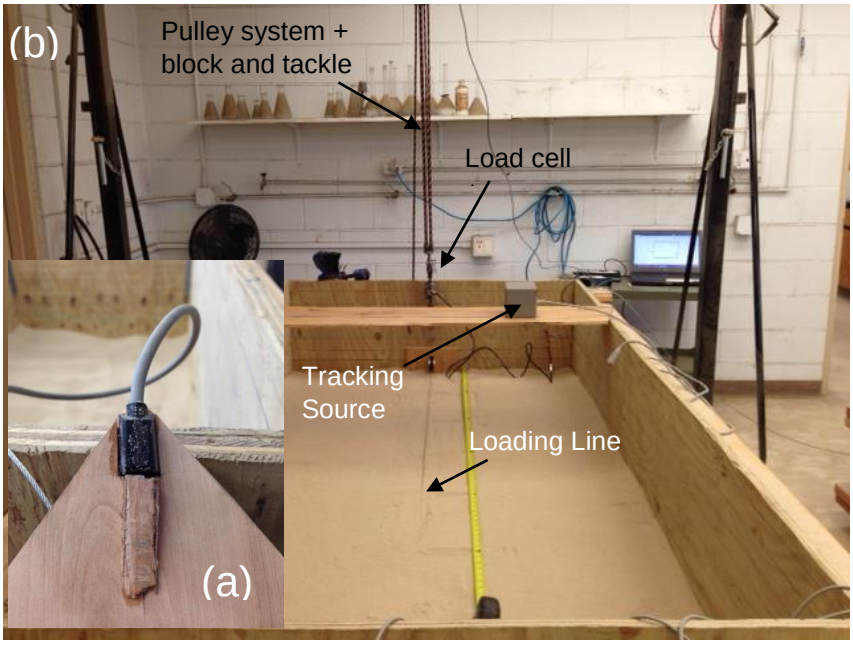

Figure 4.15. (a) Location of Polhemus magnetometer on model anchor; and (b) overview of laboratory test setup.

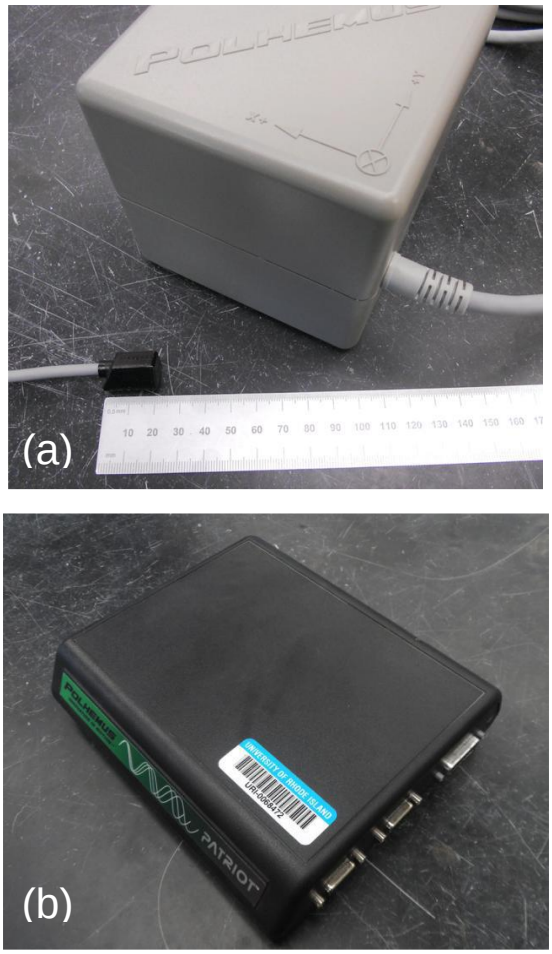

Figure 4.16. (a) Polhemus magnetometer and source; and (b) Polhemus electronics unit.

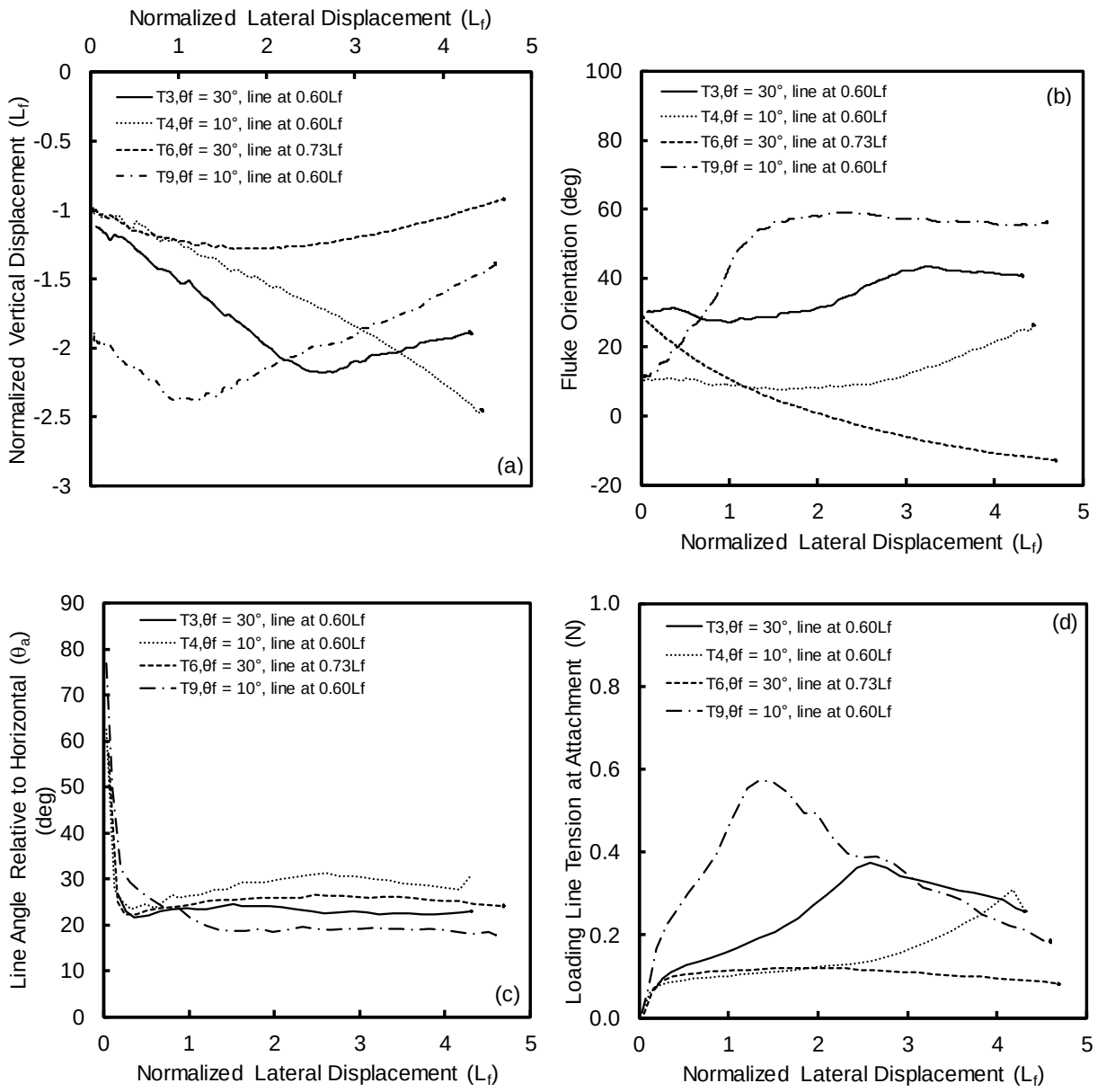

Figure 4.17. Typical results of the dive trajectory experiments with respect to normalized lateral displacements showing: (a) the trajectory or change in vertical penetration; (b) change in fluke orientation throughout dive; (c) change in the loading line angle relative to the horizontal at the attachment location; and (d) total loading line tension at the attachment location.

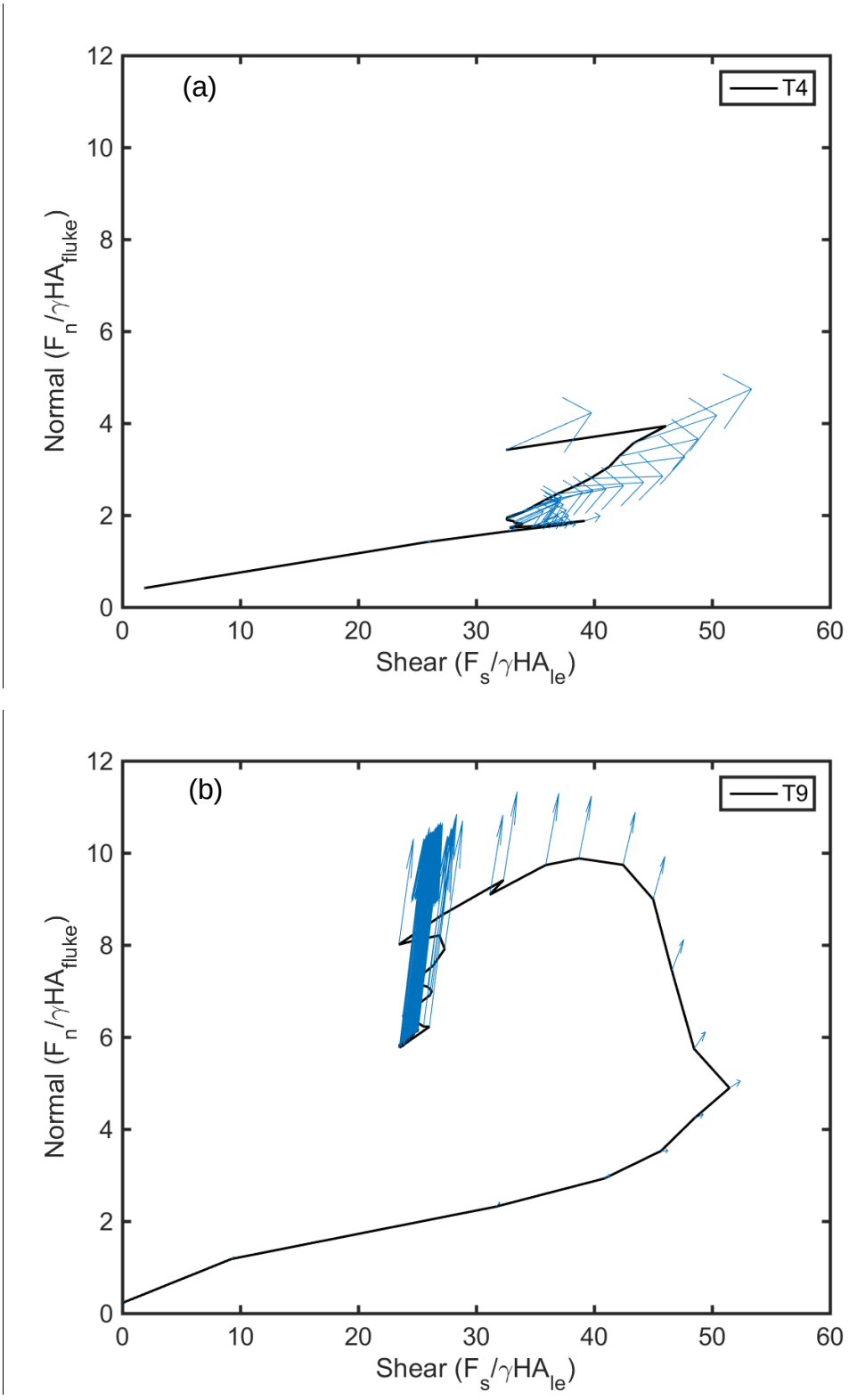

Figure 4.18. Typical normal versus shear plots with displacement vectors for experiments: (a) T4; and (b) T9.

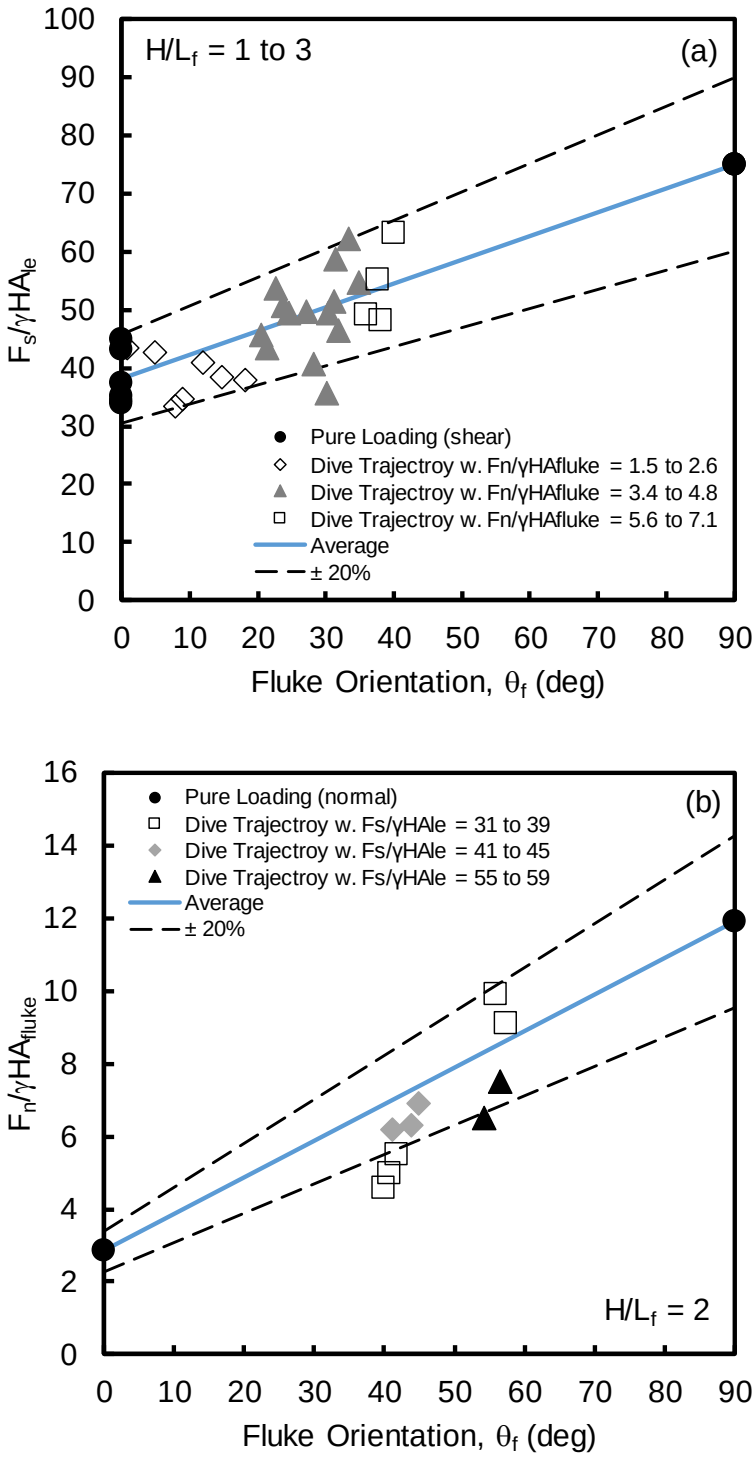

Figure 4.19. Comparison of pure loading results with values obtained from drag embedment experiments for: (a) resistance parallel to the anchor fluke with a presence of a normal force; and (b) resistance normal to the anchor fluke with a presence of a shear component or parallel to the anchor fluke.